CDF/ANAL/TOP/CDFR/10185
Version 1.0
June 14, 2010

Measurement of the Inclusive Forward-Backward Asymmetry and its Rapidity Dependence $\mathbf{A_{fb}(\Delta y)}$ of $\mathbf{t\bar{t}}$ Production in 5.3 fb^{-1} of Tevatron Data

Glenn L Strycker,[1] Dan Amidei,[1] Andrew Eppig,[1]
Dave Mietlicki,[1] Alexei Varganov,[1] Monica Tecchio,[1]
Thomas A Schwarz,[2] Robin Erbacher,[2] Joey Huston[3]

[1] *Physics Department, University of Michigan,*
450 Church Street, Ann Arbor, Michigan 48109-1040

[2] *Department of Physics, University of California-Davis,*
One Shields Ave., Davis, California, 95616

[3] *Department of Physics and Astronomy, Michigan State University,*
4230 Biomedical Physical Sciences Bldg., East Lansing, MI 48824

Abstract

We measure the parton level forward-backward asymmetry of pair produced top quarks using 1260 semi-leptonic b-tagged $t\bar{t}$ events reconstructed with the χ^2 based kinematic fitter. This is an update to the measurements found in References [1–4]. We have increased the dataset from 3.2 fb^{-1} (data through period 19) up to 5.3 fb^{-1} (data through period 27). We study the rapidity, y_{top}, of the top production angle with respect to the incoming parton momentum. In order to measure the production asymmetry in the $t\bar{t}$ frame, we also study the Lorentz-invariant quantity $q\Delta y$. We find the parton-level forward-backward asymmetry to be

$$A_{fb}^{p\bar{p}} = 0.150 \pm 0.050^{\mathrm{stat}} \pm 0.024^{\mathrm{syst}}$$
$$A_{fb}^{tt} = 0.158 \pm 0.072^{\mathrm{stat}} \pm 0.024^{\mathrm{syst}}$$

consistent with the result of CDF-9705 [1] and PRL 101 (202001) [3]. These results should be compared with the small $p\bar{p}$ frame charge asymmetry expected in QCD at NLO, $A_{fb} = 0.050 \pm 0.015$ [6–9]. Additionally, we introduce a measurement of the A_{fb} rapidity dependence $A_{fb}(\Delta y)$. We find this to be

$$\mathrm{A}_{\mathrm{fb}}^{\mathrm{t\bar{t}}}(|\Delta\mathrm{y}| < 1.0) = 0.026 \pm 0.104^{\mathrm{stat}} \pm 0.012^{\mathrm{syst}}$$
$$\mathrm{A}_{\mathrm{fb}}^{\mathrm{t\bar{t}}}(|\Delta\mathrm{y}| > 1.0) = 0.611 \pm 0.210^{\mathrm{stat}} \pm 0.246^{\mathrm{syst}}$$

which we compare with MCFM model predictions 0.039 ± 0.006 and 0.123 ± 0.018 for the inner and outer rapidities, respectively.

Contents

1 Introduction

The $t\bar{t}$ forward-backward production asymmetry (abbreviated as A_{fb}) has gained the interest of the theoretical and experimental communities because of recent measured values higher than the standard model prediction, at CDF [1–4] as well as Dzero [5] (see Section 1.6). Naturally, LO QCD predicts the top quark production angle to be completely symmetric with respect to proton beam direction, which would result in $A_{fb} = 0$. However, at NLO, QCD predicts a small charge asymmetry, $A_{fb} = 0.050 \pm 0.015$ [6–9], due to interference of initial-state radiation diagrams with final-state diagrams (Figure 1b and 1a) and the "box diagram" with Born processes (fig. 1c and 1d).

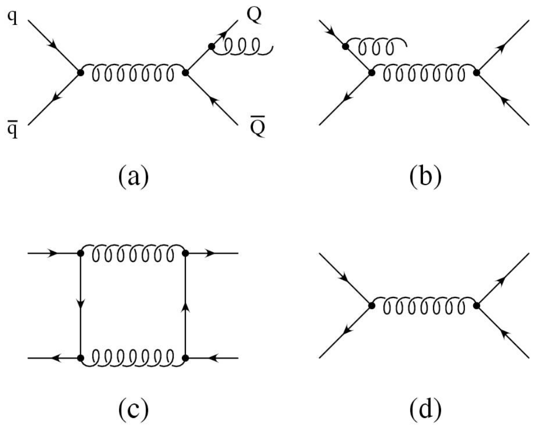

Figure 1: NLO and LO diagrams

Theoretical physics models exist that predict even larger possible A_{fb} values. "Axigluons" are involved in several such models. These hypothetical particles are heavy gluons that could interact with quarks axially as well as vectorially. The Lagrangian used in Reference [10] is

$$\begin{aligned}\frac{d\sigma^{q\bar{q}\to t\bar{t}}}{d\cos(\hat{\theta})} &= \alpha_s^2 \frac{T_F C_F}{N_C}\frac{\pi\beta}{2\hat{s}}\{1 + c^2 + 4m^2 \\ &+ \frac{2\hat{s}(\hat{s}-m_G^2)}{(\hat{s}-m_G^2)^2 + m_G^2\Gamma_G^2}[g_V^q g_V^t (1 + c^2 + 4m^2) + 2 g_A^q g_A^t c] \\ &+ \frac{\hat{s}^2}{(\hat{s}-m_G^2)^2 + m_G^2\Gamma_G^2}[((g_V^q)^2 + (g_A^q)^2) \times ((g_V^t)^2(1 + c^2 + 4m^2) \\ &+ (g_A^t)^2(1 + c^2 - 4m^2)) + 8 g_V^q g_A^q g_V^t g_A^t c]\} \qquad (1)\end{aligned}$$

Because there has been no observede $M_{t\bar{t}}$ discrepancy from the standard model, this constrains the pole term in Equation 1, as explained in Reference [10]. Choosing different values for the coupling parameters g_V^q, g_V^t, g_A^q, and g_A^t possibly can result in A_{fb} values larger than 0, as shown in Figure 2 (reproduced from Reference [10]). Thus

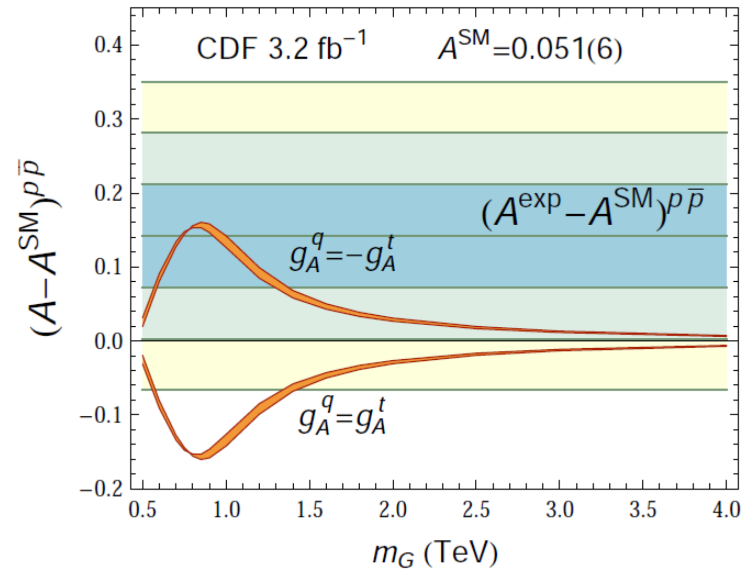

Figure 2: Contributions of Axigluons to A_{fb} as a function of the axigluon mass (reproduced from Reference [10])

we see that measuring A_{fb} in data can both verify the standard model as well as put constraints on physics beyond the standard model.

In this note, we present an update to our measurements of $t\bar{t}$ production asymmetries. Our method follows that of previous analyses CDF-9705 [1] and CDF-9078 [2]. We have increased the dataset from 3.2 fb^{-1} (data through period 19) up to 5.3 fb^{-1} (data through period 27). We study the rapidity, y_t, related to the angle that the momentum of the produced top quark makes with respect to the incoming parton momentum. Additionally, we measure the Lorentz-invariant quantity $q\Delta y$ – equivalent to $(y_t - y_{\bar{t}})$ – in order to measure the asymmetry in the $t\bar{t}$ rest frame. We subtract backgrounds according to the updated "Method II For You" (M24U) results and perform a model-independent correction for acceptance and reconstruction dilutions in order to find the asymmetry at the parton level. Finally, we introduce a new measurement of the A_{fb} rapidity dependence $A_{\text{fb}}(\Delta y)$ and compare with MCFM model predictions.

1.1 Asymmetry Overview

An integral *charge asymmetry* compares the number of top and anti-top quarks produced with momentum in a given direction. Comparing the number of tops and anti-tops produced in the proton direction, using the rapidity $\mathrm{y_t}$ or $\mathrm{y_{\bar{t}}}$, gives

$$\mathrm{A_C} = \frac{\mathrm{N_t(y > 0) - N_{\bar{t}}(y > 0)}}{\mathrm{N_t(y > 0) + N_{\bar{t}}(y > 0)}} \tag{2}$$

where $N_i(j)$ is the number of particle i observed along the direction j ($y > 0$ in this case). A non-zero value A_C implies a net top current in the proton direction.

In contrast, an integral *forward-backward asymmetry* compares the number of top quarks moving along or opposite a given direction. A convenient choice for opposite directions are the proton and anti-proton directions, thus

$$\mathrm{A_{fb}} = \frac{\mathrm{N_t(y_t > 0) - N_t(y_t < 0)}}{\mathrm{N_t(y_t > 0) + N_t(y_t < 0)}} \tag{3}$$

where $N_i(j)$ is as described above. If CP invariance is good, $\mathrm{N_{\bar{t}}(y > 0) = N_t(y_t < 0)}$ and $\mathrm{A_C = A_{fb}}$. Since the Tevatron system is CP-invariant, our analysis is built for $\mathrm{A_{fb}}$.

However, our definition of $\mathrm{A_{fb}}$ is not complete until the frame of reference is specified. Collinear ISR makes the fundamental $\mathrm{q\bar{q}}$ frame inaccessible in both experiment and simulation, leaving the $\mathrm{t\bar{t}}$ rest frame and $\mathrm{p\bar{p}}$ lab frame open to measurement. With χ^2 reconstruction, measurement of angles in the lab frame is straightforward. For angles in the $\mathrm{t\bar{t}}$ frame, however, things become more complicated. Since boosting to the lab frame may the top quark direction, we expect that any true asymmetry is larger (less diluted) in the $\mathrm{t\bar{t}}$ frame. We could measure this reliably if we can accurately boost back from the lab frame reconstruction, but such a correction introduces additional uncertainties. Because of these problems, our previous note did not include a measurement of the $\mathrm{A_{fb}}$ in the $\mathrm{t\bar{t}}$ frame. However, in this current analysis we re-introduce the Lorentz-invariant distribution $\mathrm{q\Delta y}$ to measure this value. We explain our techniques and the use of this variable $\mathrm{q\Delta y}$ below in Section 1.3.

CDF's most recent blessed measurement, CDF-9705 [1], used 3.2 $\mathrm{fb^{-1}}$ of data (period 19) to measure $\mathrm{A_{fb}}$ in the lab frame. An earlier publication, Reference [3], used 1.9 $\mathrm{fb^{-1}}$ of data (through period 12) to measure $\mathrm{A_{fb}}$ in the $\mathrm{t\bar{t}}$ rest frame. We briefly explain these methods and the results here, leaving a more in-depth discussion of our method for Sections 8 and 9.

1.2 $\mathrm{p\bar{p}}$ Frame

In the lab frame, we look at the angle between the top quark and the proton direction and measure the pseudorapidity $\mathrm{y_t}$. However, because we are using semi-leptonic events for our data sample, top quarks decay leptonically in half of our events and hadronically in the other half. This makes it problematic to use the $\mathrm{y_t}$ distribution, since acceptances are different for $\mathrm{y_{had}}$ and $\mathrm{y_{lep}}$. To control against this, for the $\mathrm{p\bar{p}}$ frame measurement we will just measure the rapidity of hadronically-decaying quark $\mathrm{y_{had}}$, whether or not it was a top or anti-top. We know which quark (top or antitop) decayed hadronically by the charge of the lepton in the event, as shown in Table 1. This means that $\mathrm{y_{had}}$ is either $\mathrm{y_t}$ or $-\mathrm{y_{\bar{t}}}$. Assuming CP-invariance allows us to multiply $\mathrm{y_{had}}$ by $-1{\cdot}\mathrm{q_{lepton}}$, resulting in $-\mathrm{q}{\cdot}\mathrm{y_{had}} = \mathrm{y_t}$. This gives us an *equivalent top rapidity.* We use $-\mathrm{q_{lepton}}$ so that a net top current in the proton direction will produce a positive asymmetry. We see that Equation 3 now becomes

$$\mathrm{A_{fb}^{p\bar{p}}} = \frac{\mathrm{N}(-\mathrm{q}{\cdot}\mathrm{y_{had}} > 0) - \mathrm{N}(-\mathrm{q}{\cdot}\mathrm{y_{had}} < 0)}{\mathrm{N}(-\mathrm{q}{\cdot}\mathrm{y_{had}} > 0) + \mathrm{N}(-\mathrm{q}{\cdot}\mathrm{y_{had}} < 0)} \tag{4}$$

This is the definition for $\mathrm{A_{fb}}$ used in our previous note [1].

$\mathrm{q_l}$	$\mathrm{t_{lep}}$	$\mathrm{t_{had}}$
$+$	t	$\mathrm{\bar{t}}$
$-$	$\mathrm{\bar{t}}$	t

Table 1: The leptonic and hadronic systems in events with positive and negative leptons

1.3 $\mathrm{t\bar{t}}$ Frame

To make a measurement of $\mathrm{A_{fb}}$ in the $\mathrm{t\bar{t}}$ frame, consider the following algebra:

$$-1{\cdot}\mathrm{q_{lepton}}(\mathrm{y_{had}} - \mathrm{y_{lep}}) = \mathrm{q_{lepton}}(\mathrm{y_{lep}} - \mathrm{y_{had}}) \equiv \mathrm{q}\Delta\mathrm{y} \tag{5}$$

$$\begin{aligned}
\mathrm{y_{top}^{rest}} &= \mathrm{y_{top}^{lab}} - \mathrm{y}^{\mathrm{t\bar{t}\ system}} \\
&= \mathrm{y_t} - \frac{1}{2}(\mathrm{y_t} + \mathrm{y_{\bar{t}}}) \\
&= \frac{1}{2}(\mathrm{y_t} - \mathrm{y_{\bar{t}}})
\end{aligned}$$

$$
\begin{aligned}
&= \frac{1}{2}\Delta \mathrm{y}_{\mathrm{top}} \\
&= \frac{1}{2}\mathrm{q}_{\mathrm{lepton}}(\mathrm{y}_{\mathrm{lep}} - \mathrm{y}_{\mathrm{had}}) \qquad (6) \\
&\equiv \frac{1}{2}\mathrm{q}\Delta \mathrm{y} \qquad (7)
\end{aligned}
$$

These equations show that top rapidity measured in the $\mathrm{t\bar{t}}$ rest frame is proportional to the quantity $\Delta \mathrm{y}_{\mathrm{top}}$ (and equivalently, $\mathrm{q}\Delta \mathrm{y}$). Because $\Delta \mathrm{y}_{\mathrm{top}}$ is the difference of two rapidities, it is Lorentz-invariant. We see from the definition of $\Delta \mathrm{y}_{\mathrm{top}}$ (Equation 3 in reference [4]) that $\Delta \mathrm{y}_{\mathrm{top}}$ is related to the angle of the top quark production with respect to the incoming parton:

$$y_t - y_{\bar{t}} = 2\cdot \tanh^{-1}\left(\frac{\cos(\theta^*)}{\sqrt{1+\frac{4m_t^2}{\hat{s}-4m_t^2}}}\right) \tag{8}$$

where $\hat{s}$ is center of mass energy, m_t is the top quark mass, and $\cos(\theta^*)$ is the angle of the top quark production with respect to the incoming parton. Note that while there is not an exact 1:1 correspondence of $\Delta \mathrm{y}$ with $\cos(\theta^*)$ due to $\hat{s}$, the forward-backward nature remains the same. That is, if $\theta < 0$ ($\mathrm{y}_{\mathrm{had}} < 0$), then $\tanh^{-1}(\cos(\theta^*)) < 0$, so $\Delta \mathrm{y} < 0$. Therefore asymmetries in $\Delta \mathrm{y}$ will be identical to those in $\cos(\theta^*)$ and $\mathrm{y}_{\mathrm{had}}$, allowing an effective measurement in the $\mathrm{t\bar{t}}$ rest frame. In practice, the difference of top and anti-top rapidities is related to the difference of the hadronic and leptonic top rapidities. Again, because of CP invariance, we are able to multiply the distribution $(\mathrm{y}_{\mathrm{had}} - \mathrm{y}_{\mathrm{lep}})$ by -1 times the sign of the lepton $\mathrm{q}_{\mathrm{lepton}}$, resulting in $\mathrm{q}\Delta \mathrm{y}_{lep,had}$ being equivalent to $(\mathrm{y_t} - \mathrm{y_{\bar{t}}})$. In this paper, we refer to the quantity $-1\cdot \mathrm{q}_{\mathrm{lepton}}(\mathrm{y}_{\mathrm{had}} - \mathrm{y}_{\mathrm{lep}}) = \mathrm{q}_{\mathrm{lepton}}(\mathrm{y}_{\mathrm{lep}} - \mathrm{y}_{\mathrm{had}})$ with the notation $\mathrm{q}\Delta \mathrm{y}$.

Using our new notation and the frame-invariance of $\mathrm{q}\Delta \mathrm{y}$, we are able to write

$$\mathrm{A}_{\mathrm{fb}}^{\mathrm{t\bar{t}}} = \frac{\mathrm{N}(\mathrm{q}\Delta \mathrm{y} > 0) - \mathrm{N}(\mathrm{q}\Delta \mathrm{y} < 0)}{\mathrm{N}(\mathrm{q}\Delta \mathrm{y} > 0) + \mathrm{N}(\mathrm{q}\Delta \mathrm{y} < 0)} \tag{9}$$

In principle, this equation recovers the larger undiluted asymmetry than $\mathrm{A}_{\mathrm{fb}}^{\mathrm{p\bar{p}}}$, but possibly with a larger uncertainty, as the neutrino uncertainty still enters through the involvement of $\mathrm{y}_{\mathrm{lep}}$ in the calculation of $\Delta \mathrm{y}$. However, since that means that the $\mathrm{A}_{\mathrm{fb}}^{\mathrm{t\bar{t}}}$ measurement includes information “thrown-away” from the $\mathrm{A}_{\mathrm{fb}}^{\mathrm{p\bar{p}}}$ measurement, we see that it is best to make *both* measurements to compare with other experiments and theoretical predictions.

1.4 Correction to the Parton Level

The raw $\mathrm{A_{fb}}$ values calculated directly from data using Equations 3 and 9 need to be corrected back to the parton level by accounting for the presence of backgrounds and shape distortions. First, we note that non-signal events that pass our selection criteria cuts (see Sections 2 and 4), particularly those from electroweak processes, may have asymmetries that affect the final $\mathrm{A_{fb}}$ calculation. These backgrounds are estimated and subtracted, using the method we repeat and explain in Section 8. Event selection cuts (see Section 2) remove some signal events and modify the distribution shape of our production angle data, so we will need to correct for possible acceptance bias (explained in Section 9). Finally, the t and $\bar{\mathrm{t}}$ four vectors must be reconstructed from limited information (4 jets, 1-2 btags, MET, as explained in Sections 2 and 5), and it is known that uncertainty in reconstruction causes smearing of the $\mathrm{y_{had}}$ and $\Delta\mathrm{y}$ distributions. The acceptance and smearing effects are corrected using a matrix unfold method that we explain briefly here and explain completely in Section 9.

1.5 Measuring $\mathrm{A_{fb}}(\Delta\mathrm{y})$

As we discussed in the introduction, $\mathrm{A_{fb}}$ measurements are a way to test the standard model and search for physics beyond the standard model. However, finding a non-zero $\mathrm{A_{fb}}$ is not enough – to distinguish between possible models it is advantageous to investigate the dependence of $\mathrm{A_{fb}}$ as a function of other variables. Now that our dataset has more than 1000 $\mathrm{t\bar{t}}$ events, we are gaining enough statistical precision to do this.

The discussion in Reference [9] indicates that the cross-section terms responsible for the asymmetry are proportional to the β of the top/antitop quarks in the center-of-mass; thus, the asymmetry is expected to increase with the rapidity separation of the two quarks. We have shown in Section 1.3 that the rapidity separation is very closely related to the production angle $\cos(\theta^{*})$, so we are not surprised that Reference [9] predicts that the asymmetry grows almost linearly with the production angle, as seen in Figure 3. (Reference [9] also uses resummation techniques to examine the stability of the asymmetry at higher orders and finds only modest corrections, as shown.)

In order to reproduce these calculations for ourselves, we use the program MCFM [11], which is a fully NLO calculation with NLO PDFs, for predicting particle physics at the parton level. In Figure 4, we see that the predicted NLO QCD $\mathrm{A_{fb}}(\Delta\mathrm{y})$ behavior is linear, as we expect from the close relationship between $\Delta\mathrm{y}$ and $cos(\theta^{*})$.

To compare with MCFM predictions, we measure the asymmetry as a function of y or $\Delta\mathrm{y}$, which we then write as $\mathrm{A_{fb}}(\Delta\mathrm{y})$. Because dividing our sample into smaller parts reduces the available statistics, we use the binning scheme described in Section 9.1 (4 bins) and make no finer division of events. The rapidity dependence is then measured by examining the inner and outer bin pairs, using the forward and backward bin event counts in our usual formula.

Using this method allows us to measure the raw rapidity dependence $A_{fb}(\Delta y)$, but we can additionally correct our measurement to the parton level. The same "unfolded" bin event counts from the inclusive A_{fb} correction method can be used to calculate pair-wise corrected A_{fb} values. Statistical errors are propagated using the methods described in Sections 9.3 and 10. Thus we obtain $A_{fb}(\Delta y)$ for background-corrected data as well as fully-corrected data.

We verify that this new measurement method works by examining MC samples with known asymmetries and compare our measured values with the true A_{fb} and $A_{fb}(\Delta y)$ values. By using pseudo-experiments, we can additionally verify the error propagation techniques and test our method for possible biases. We find that our method is reasonable and reconstructs the truth-level A_{fb} and $A_{fb}(\Delta y)$ values quite well.

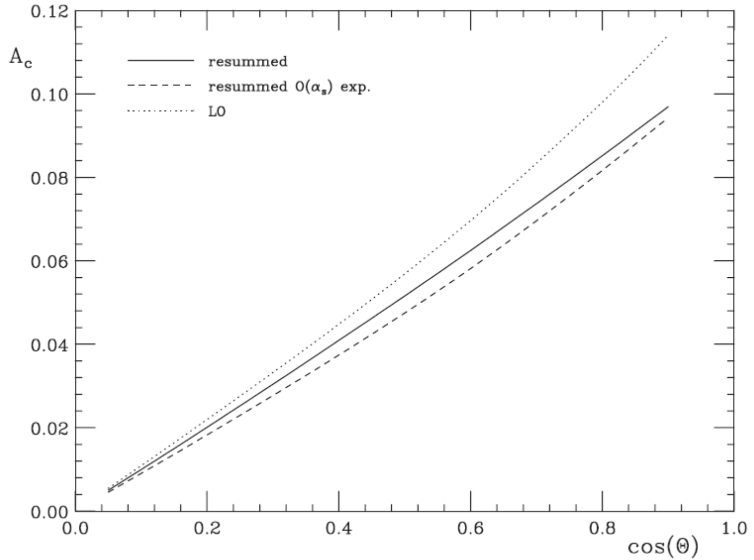

Figure 3: A_C as a function of $\cos(\theta)$
(Reproduced from Reference [9])

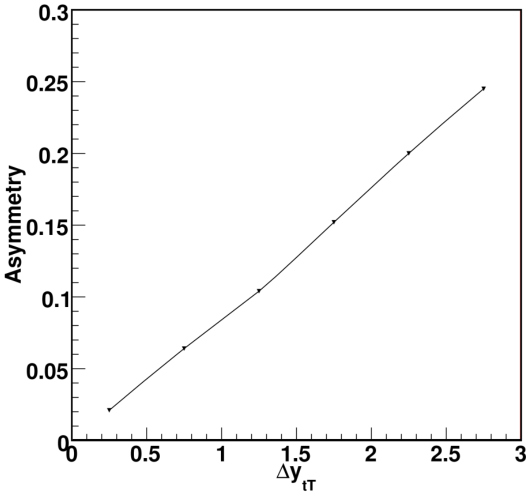

Figure 4: MCFM Prediction for $\mathrm{A_{fb}}(\Delta\mathrm{y})$

1.6 Previously Published Results

CDF-9705 [1], using 3.2 $\mathrm{fb^{-1}}$ of data (through period 19), observed

$$\mathrm{A_{fb}}(-\mathrm{q}\cdot\mathrm{y_{had}}) = \mathrm{A_{fb}^{p\bar{p}}} = 0.193 \pm 0.065^{\mathrm{stat}} \pm 0.024^{\mathrm{syst}} \tag{10}$$

The $\mathrm{p\bar{p}}$ frame value is large, but consistent with the NLO prediction of $\mathrm{A_{fb}} = 0.050 \pm 0.015$ within large uncertainty. CDF-9705 did not measure $\mathrm{A_{fb}^{t\bar{t}}}$, but in [3], using 1.9 $\mathrm{fb^{-1}}$ of data (through period 12), $\mathrm{t\bar{t}}$ frame $\mathrm{A_{fb}}$ was measured as

$$\mathrm{A_{fb}}(\mathrm{q}\Delta\mathrm{y}) = \mathrm{A_{fb}^{t\bar{t}}} = 0.24 \pm 0.14^{\mathrm{stat}} \tag{11}$$

These results in the two frames are roughly consistent with the theoretically expected expected dilution of 30% in passing from $\mathrm{t\bar{t}}$ to $\mathrm{p\bar{p}}$ frames [6].

Dzero has also measured $\mathrm{A_{fb}}$ [5]. They did not correct their value to the parton frame, and chose simply to state the "raw" measured value. Using 0.9 $\mathrm{fb^{-1}}$ of data and the Δy variable, they find

$$\mathrm{A_{fb}^{D0}}(|\Delta\mathrm{y}|) = 0.12 \pm 0.08^{\mathrm{stat}} \pm 0.01^{\mathrm{syst}} \tag{12}$$

1.7 The Plan for this CDF Note

Now that we have introduced our variables and motivated our measurement by explaining some of the theory behind a possible non-zero $\mathrm{A_{fb}}$, the rest of this note is organized as follows: Section 2 will explain the event selection cuts used for semi-leptonic $\mathrm{t\bar{t}}$ events. We discuss the resulting 5.3 $\mathrm{fb^{-1}}$ dataset in Section 3. Backgrounds that pass our event selection cuts will be explained in Section 4, along with a description of the MC samples used in the M24U background estimation procedure. Section 5 describes the CDF Top Group method for reconstructing $\mathrm{t\bar{t}}$ events from CDF data. In Section 6 we will explain our validation of the data set, showing that event reconstruction in Section 5 was good. Once we have established that our dataset is well reconstructed, we turn in Section 7 to an in-depth description of our main distributions $-\mathrm{q{\cdot}y_{had}}$ and $\mathrm{q\Delta y}$. We then explain our techniques for correcting these distributions back to the parton level in Sections 8 and 9. In Section 10 we introduce our new measurement of $\mathrm{A_{fb}(\Delta y)}$, the rapidity dependence of $\mathrm{A_{fb}}$. We then make our measurement in Section 11, look at cross-checks of our method in Section 12, and discuss systematic uncertainties in Section 13. We conclude our note with our final measurement values in Section 14.

2 Event Selection Summary

A summary of the selection criteria for semi-leptonic $t\bar{t}$ events is shown below. Please see the appendix, beginning with Section 15, for the full details of our selection criteria and event reconstruction techniques. As shown in Section 4, this set of selection requirements produces roughly a 977/283 = 3.5:1 signal to background ratio.

- One tight high-P_t lepton, as described in the appendix, Sections 16 and 17
  First criteria for selection, which occurs at both trigger level and offline.
- Dilepton veto:
  Separates lepton plus jets from dilepton events.
- Z veto:
  Reduces the amount of background with Z-bosons.
- Primary vertex check:
  Ensures the lepton and jets originate from the same process.
- $\not{E}_T \geq 20$ GeV:
  Selection based upon the presence of a neutrino in lepton plus jets events.
- ≥ 4 Tight Jets:
  Reduces background by requiring the same number of jets as partons in a $t\bar{t}$ lepton plus jets event.
- ≥ 1 SecVtx "Tagged" jet:
  Rejects background processes without heavy flavor quarks present.

2.1 TopMods Code Tags

In order to correct our jet energies, mistag matrices, and apply other corrections to our events before making cuts, the TopMods code package is used. We implement the following "tags" for CVS checkout for use in our analysis code:

```
my $topModsTag = "top_614_p23_v1";
my %packages =
  (
   # Package              Version
   JetUser             => "jetCorr18",
   BTagObjects         => "btag_4100invpb_v4",
   RootFileCollection => "rfc080609",
   JointPhysics        => "jp091120",
  );
```

Additionally, we have edited the TopMods code to include the file `BTagObjects/jetMistagJun2009.hh` instead of `BTagObjects/jetMistagApr2008.hh`. This is seen in files such as `TopMods/TopAnaTools/TopAnaTools/HeavyFlavorUtils.hh`.

3 Dataset Summary

Table 2 shows the run ranges for the data set used in this note, periods 0-27, corresponding to a silicon-good-run integrated luminosity of 5.3 fb^{-1}. Because our previous measurement was through p19, we compare data from p20 through p27 to check if the number of additional $t\bar{t}$ events corresponds with what we would expect from the increase in integrated luminosity (2.1 fb^{-1}). Based on p19, with 2504 pretag and 776 tagged events in 3.2 fb^{-1}, we expect the additional 2.1 fb^{-1} to yield 1643 ± 41 pretag and 509 ± 23 tagged events. We actually observe 1775 new pretags and 484 new tagged events. This downward fluctuation in the number of tagged events is larger than expected, (but tracks the downward movement of the blessed cross-sections over this data span ????).

Dataset ID	Trigger	Run Range
bhel0d bhmu0d	CEM CMUP, CMX	138425-186598
bhel0h bhmu0h	CEM CMUP, CMX	190697-203799
bhel0i bhmu0i	CEM CMUP, CMX	203819-228596
bhel0j bhmu0j	CEM CMUP, CMX	228664-246231
bhel0k bhmu0k	CEM CMUP, CMX	252836-261005
bhel0m bhmu0m	CEM CMUP, CMX	261119-287261

Table 2: Data sets

	p0-p19 = 3.2 fb^{-1}	p20-p27 = 2.1 fb^{-1}	Expected p20-p27
Inclusive	777	483	509 ± 23
CEM	438	297	287 ± 17
CMUP	219	113	144 ± 12
CMX	120	73	79 ± 9
nJet==4	579	360	380 ± 19
nJet≥5	198	123	130 ± 11
Single Tagged	603	376	396 ± 20
Double Tagged	174	107	114 ± 11

Table 3: Breakdown of Added Data

4 Backgrounds, MC Samples

Our background models and their normalizations are based on the "Method II For You" (M24U) procedure [14] applied to data through p27. The samples used for generating our background shapes are listed in Table 4. The calculated contribution of each background component in our sample is given in Table 5. The total number of background events in the sample is 283.3 ± 49.9 ????. The sample contains 1260 top-pair events, and the ratio of number of signal events to background is roughly 977/283 = 3.5:1.

We note here a somewhat unfortunate fact: we do not have a signal model for $\mathrm{t\bar{t}}$ that has a non-zero $\mathrm{A_{fb}}$ value! That is, the CDF Top Group does not have a working MC@NLO sample, although work is in progress. Instead, we use the $\mathrm{t\bar{t}}$ Pythia MC sample ttop25 ($\mathrm{M_t} = 172.5\mathrm{GeV/c^2}$). This sample has been verified by the CDF Top Group to closely match our data in most reconstructed variables, as we show in our data validation plots and discuss in Section 6. Pythia is a LO Monte Carlo and has no intrinsic asymetry. We can use it as a null-signal control sample, and it is useful in that regard to establish that we are free from bias. However, we do look forward to using MC@NLO to establish our sensitivity for the expected small asymmetry from QCD.

However, while we do not have a non-zero-$\mathrm{A_{fb}}$ $\mathrm{t\bar{t}}$ sample, we have made an MC model using madgraph that has a non-zero $\mathrm{A_{fb}}$ value for a new physics model. The ctopo3 MC was made using the Axigluon Lagrangian shown in Equation 1, with parameters M = 1.8 TeV, $g_V = 0$, $g_A^q = -\frac{3}{2}$, $-g_A^t = +\frac{3}{2}$, picked so that both the $\mathrm{M_{t\bar{t}}}$ distribution and measured $\mathrm{A_{fb}}$ value of the MC closely match that of our data. See Figures 5 and 6 below, where we compare the ctopo3+background shape (green histogram) with data (black) using M24U background predictions (blue). We see that ctopo3/madgraph does reproduce the raw $\mathrm{A_{fb}}$ seen in the data (in fact, it is actually a bit high) while keeping the $\mathrm{M_{t\bar{t}}}$ distribution in relative compliance with the data. We are encouraged that there is a physics model that can do this, but more importantly, it means that we can test a correction procedure on a sample that has a large asymmetry and no other spectrum distortions (as would be the case of $\mathrm{Z'} \rightarrow \mathrm{t\bar{t}}$, for example).

We use this MC in Sections 9, 10, and elsewhere – whenever we need a sample with non-zero $\mathrm{A_{fb}}$ for verification of a procedure. For example, in Section 9.4 we use ctopo3 to verify that we can correct the reconstructed $-\mathrm{q{\cdot}y_{had}}$ and $\mathrm{q\Delta y}$ distributions back to the parton level and measure the correct $\mathrm{A_{fb}}$ value.

Note that we are not claiming this sample as signal hypothesis! We are merely using ctopo3 as a control sample having a non-zero $\mathrm{A_{fb}}$.

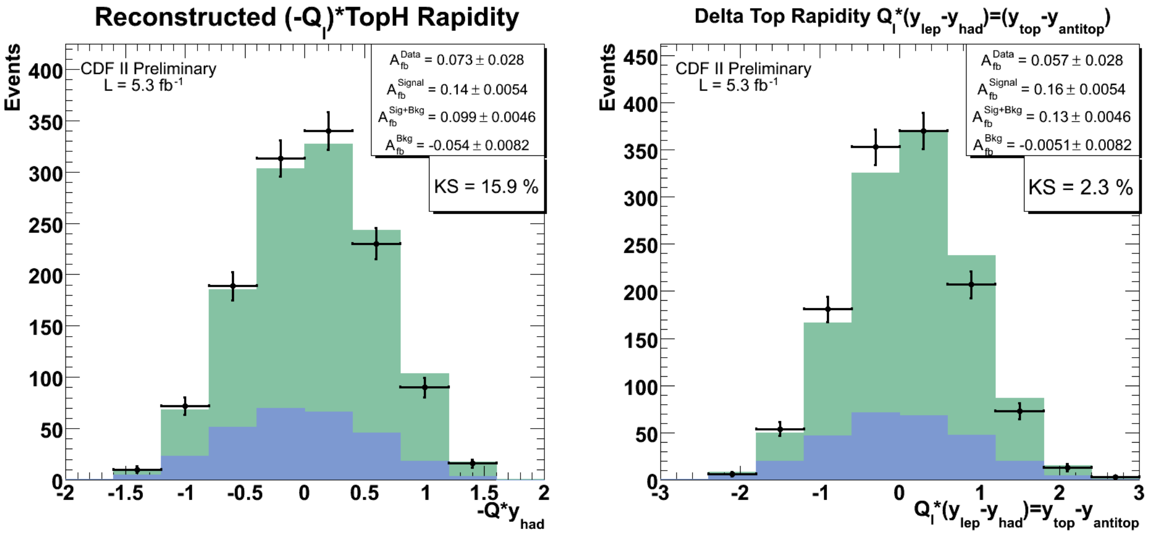

Figure 5: $-q{\cdot}y_{\mathrm{had}}$ and $q\Delta y$ of data (black) compared with ctopo3+background (green)

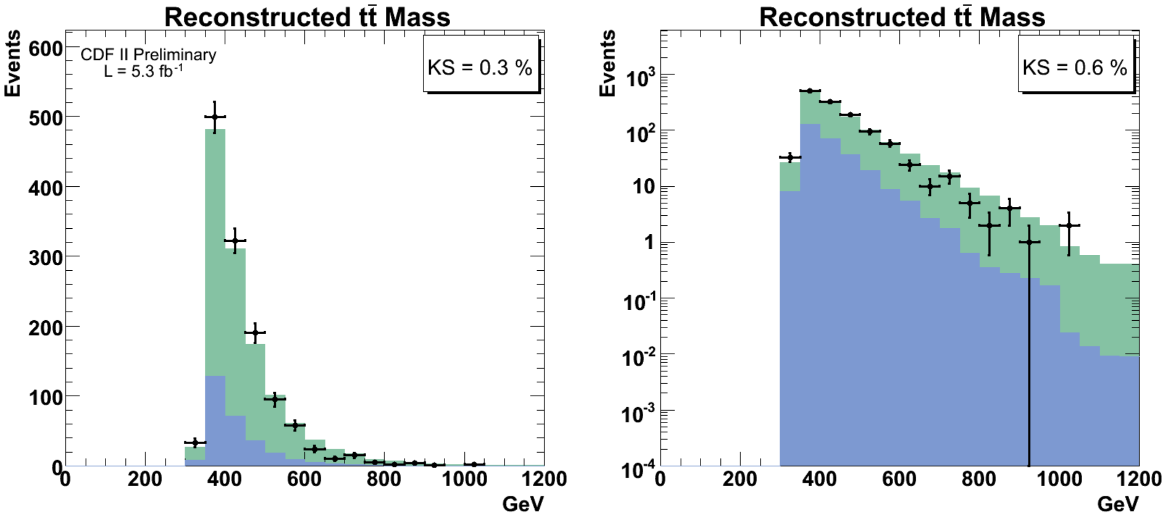

Figure 6: $M_{t\bar{t}}$ of data (black) compared with ctopo3+background (green)

Process	Dataset ID	Type
$t\bar{t}$	ttop25	Pythia
QCD	gjt1X	Jet Electrons
Wbb	btopXw, dtopXw	Alpgen
Wcc	btopXX, ctopXw, etopwX	Alpgen
Wc	stopwX, otopwX	Alpgen
Wlf	ptopXw, ptopwX, utopX, utopXw	Alpgen
WW/WZ/ZZ	itopww, htopww, itopwz, htopwz, itopzz, htopzz	Pythia
Single Top - S	stop26, stop23	MadEvt/Pythia
Single Top - T	stop27_28, stop3m	MadEvt/Pythia
Z+Jets	btopzX, ztopbX, ztopcX, ztoppX, ztopXp	Alpgen

Table 4: Background And Signal Models

Process	==4 Jets	$\geq$ 5 Jets
W + HF Jets	109 ± 34.1	26.5 ± 8.6
Mistags (W+LF)	36.8 ± 9.3	8.4 ± 3.1
Non-W (QCD)	50.1 ± 25.3	17.4 ± 9.2
Single Top S	5.6 ± 0.6	1.2 ± 0.1
Single Top T	7.5 ± 0.6	1.3 ± 0.1
WW	6.2 ± 0.8	1.7 ± 0.2
WZ	1.6 ± 0.2	0.5 ± 0.1
ZZ	0.6 ± 0.1	0.1 ± 0.01
Z+Jets	7.1 ± 0.9	1.7 ± 0.2
Total Prediction	224.5 ± 47.8	58.8 ± 14.2

Table 5: Summary of M24U numbers used –
see Table 7 for the raw A_{fb} values of each background sample.

5 Event Reconstruction

The $t\bar{t}$ semi-leptonic decay results in an up-quark jet, down-quark jet, b and $\bar{b}$ jets, a lepton, and neutrino. The kinematic fitter finds best estimates for the four-vectors of these objects according to the constraint prescription described in the subsections below, CDF-6845 [21], and the kinematic fitter web page [20]. We constrain the top and antitop quark masses to be $M_t = 172.5 \mathrm{GeV/c}^2$. In Section 25 (in the Appendix), we compare the reconstructed parton kinematics in the data to the MC model for the $t\bar{t}$ signal and background. These plots show the raw data as black points (with Poisson error bars), M24U background as the blue histogram, and the solid light-green histogram is the $t\bar{t}$ Pythia MC sample ttop25, normalized such that the signal+background event counts are the same as the number of data events (1260). Note that the χ^2 distribution in Figure 36 shows the data agreeing with the model even out to the overflow bin at $\chi^2 \geq 90$.

5.1 Tagging in the Monte Carlo Model Samples

The Monte Carlo slightly over estimates the tagging and mis-tagging rate found in data. To correct for this, the tagging scale factor and the mistag matrix must be applied to Monte Carlo heavy flavor and light flavor jets respectively. The event tagging probability is the sum of all possible tagging combinations. For example, in a four tight jet event, the tagging probability for tagging just the first jet is:

$$P_{1Tag}^{Jet1} = P_1 \cdot (1 - P_2) \cdot (1 - P_3) \cdot (1 - P_4)$$

where P_1 is the tagging SF or the mistag probability depending on whether the jet originates from light flavor or heavy flavor in the Monte Carlo. The event tagging probability is then:

$$P_{1Tag}^{Event} = P_{=1Tag}^{Jet1} + P_{=1Tag}^{Jet2} + P_{=1Tag}^{Jet3} + P_{=1Tag}^{Jet4}$$

Every event in the Monte Carlo simulations is weighted by it's total tagging probability as prescribed above. The above prescription is of course different for the various combinations of jet and tagging multiplicities, but the same principles apply.

5.2 Handling Btagging with the Kinematic Fitter

As described in above sections, the Monte Carlo does not correctly describe tagging and mis-tagging efficiency found in data. To correct for this, we apply tagging scale factors and mis-tag rates to the Monte Carlo. The solution to the kinematic fitter depends on which jets are tagged, requiring tagged jets to be assigned as bottom quarks. Therefore, *each* tagging combination has a unique lowest χ^2 solution associated with it. Each solution from the kinematic fitter associated with a tagging combination must then contribute to any shape or calculation of a value. We weight each solution from the fitter by its associated tagging probability. For example, in the four tight jet, 1 tag event above in Section 5.1 there are four solutions from the kinematic fitter that will each contribute to every histogram.

6 Data Validation

In order to trust our measurement, we must first check that the detector does not have an inherent asymmetry or that the kinematic fitter biases our reconstructed quantities. The plots for the following sections (moved to the appendix, Sections 24 and 25) demonstrate that this is not the case. We see that the data agree with the model, as can be seen by the reasonable KS-test values for each plot (values greater than 10^{-3} that are roughly uniformly distributed between 0 and 1 are indicative of good agreement between histograms).

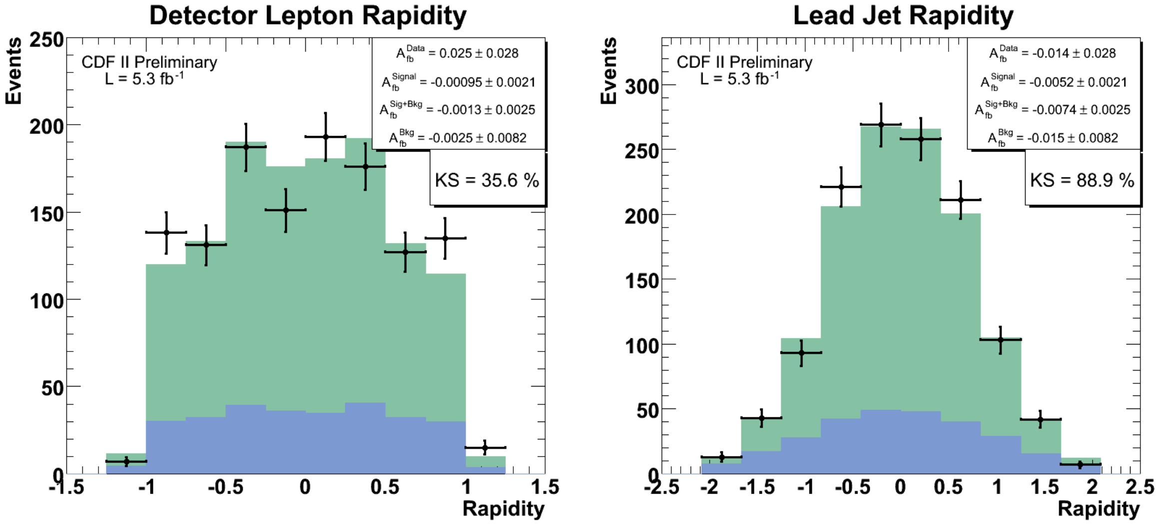

Figure 7: Sample validation distributions – see the Appendix for the full set of plots

6.1 Detector Variables and Observables

Before checking reconstructed $t\bar{t}$ event variables, we will first verify that our signal and background shapes correctly model the CDF detector. To verify this, we have examined many event variables, such as jet energy and rapidities, lepton Pt and rapidity, and various angles between the jets, lepton, and MET.

Our validation plots tabulated in the appendix, Section 24, use the data sets explained above. See Figure 7 above for an example of our validation plots. The black points represent data with Poisson errors, the blue region is the background MC normalized to M24U values, and the green region is signal ($\mathrm{t\bar{t}}$ ttop25 Pythia MC) normalized so that background+signal is equal to the number of data events.

6.2 Kinematic Fitter and Reconstructed Variables

In the appendix, Section 25, we present plots comparing data and MC for variables reconstructed using the kinematic fitter. The $\mathrm{t\bar{t}}$ semi-leptonic decay results in an up-quark jet, down-quark jet, b and $\mathrm{\bar{b}}$ jets, a lepton, and neutrino. The kinematic fitter assigns the jets, lepton, and MET to these particles as explained above in Section 5. We examine these plots to check the goodness of the kinematic fitter. We note from the χ^2 distribution in Figure 36 that our fitter does equally well reconstructing $\mathrm{t\bar{t}}$ events from data as from MC, as the χ^2 distribution of the fitted events closely matches the shape of the background even out to the overflow bin at $\chi^2 \geq 90$.

7 The Rapidity of the Top Quark

Having validated our detector data and reconstructed variables from the kinematic fitter, we are now ready to investigate our $-\mathrm{q}\cdot\mathrm{y}_{\mathrm{had}}$ and $\mathrm{q}\Delta\mathrm{y}$ distributions and measure our uncorrected A_{fb} values in the lab and $\mathrm{t\bar{t}}$ frames.

First, let us briefly examine the reconstructed $\mathrm{y}_{\mathrm{had}}$ distributions, separated by the lepton charge, as shown in Figure 8. Table 6 shows the raw A_{fb} of these distributions. The data shapes are roughly reflections about $y = 0$ and their A_{fb} values are significantly non-zero, similar to each other in magnitude, but opposite in sign. This is indicative that the y_{t} distribution is indeed asymmetric, but in a *CP-invariant way*, with the top and anti-top asymmetries equal in magnitude but different in sign. We see similar charge-dependent values for the $\mathrm{q}\Delta\mathrm{y}$ variable in Figure 9. We combine the charge-separate plots into the primary distributions used in the remainder of our analysis, shown in Figure 10. Note that the KS-test values for these combined distributions are quite low (0% for $-\mathrm{q}\cdot\mathrm{y}_{\mathrm{had}}$ and 2% for $\mathrm{q}\Delta\mathrm{y}$), which is expected for data exhibiting an asymmetry greater than the background and signal predictions. We want to relate these asymmetries measured in these raw distributions to their true asymmetry values at the parton level, so we need to correct for the background component and account for smearing and acceptance effects. We turn now to techniques for these corrections and return to our measurement in Section 11.

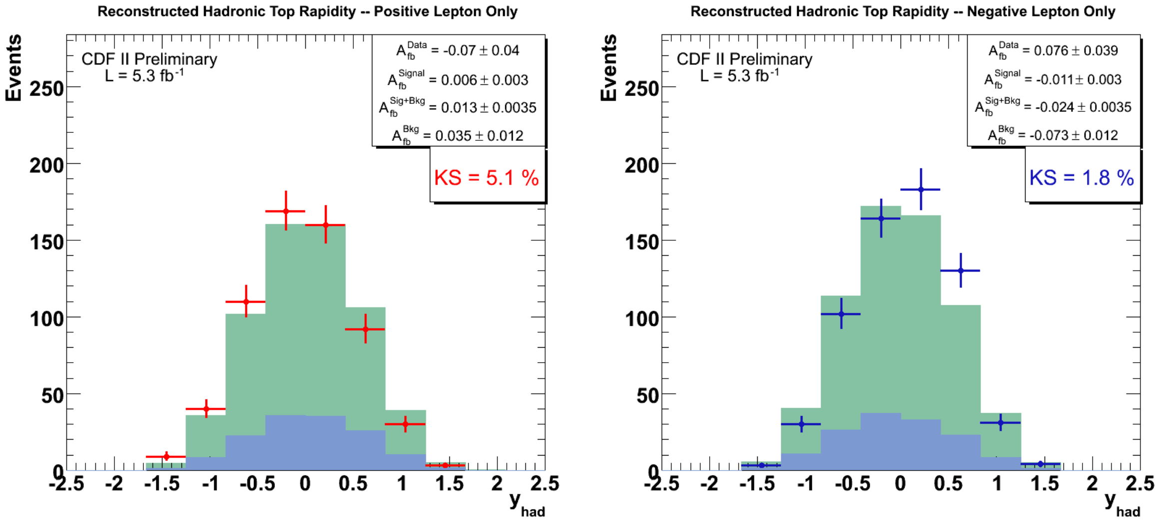

Reconstructed Hadronic Top Rapidity -- Positive Lepton Only

Reconstructed Hadronic Top Rapidity -- Negative Lepton Only

Figure 8: y_{had} distributions by lepton charge
Note that the A_{fb} values for these plots differ in sign, and that the top signal area has been renormalized for each lepton shape so bkg+sig has same area as data.

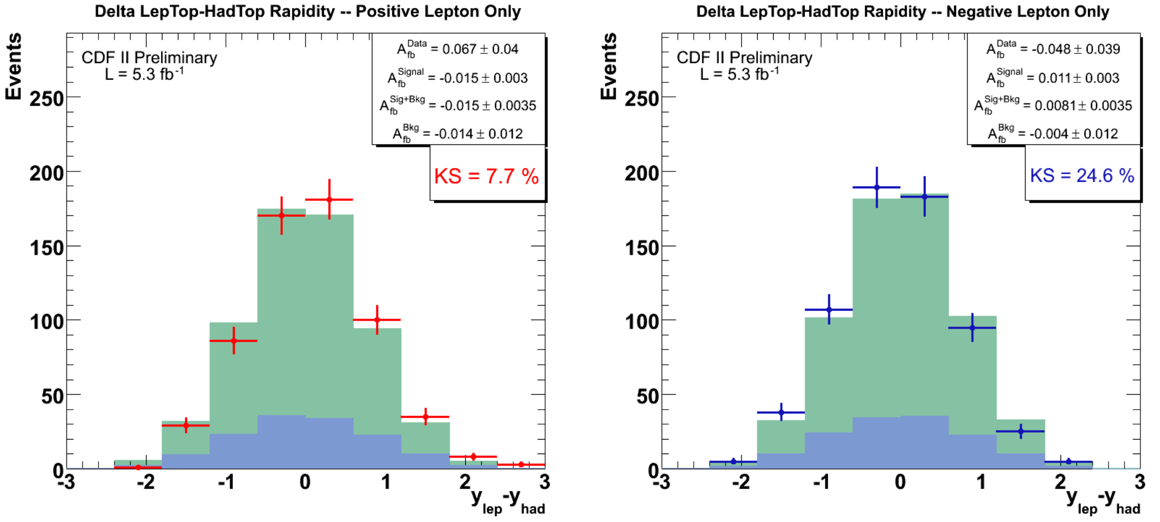

Delta LepTop-HadTop Rapidity -- Positive Lepton Only

Delta LepTop-HadTop Rapidity -- Negative Lepton Only

Figure 9: Δy distributions by lepton charge
Note again that the A_{fb} values for these plots differ in sign.

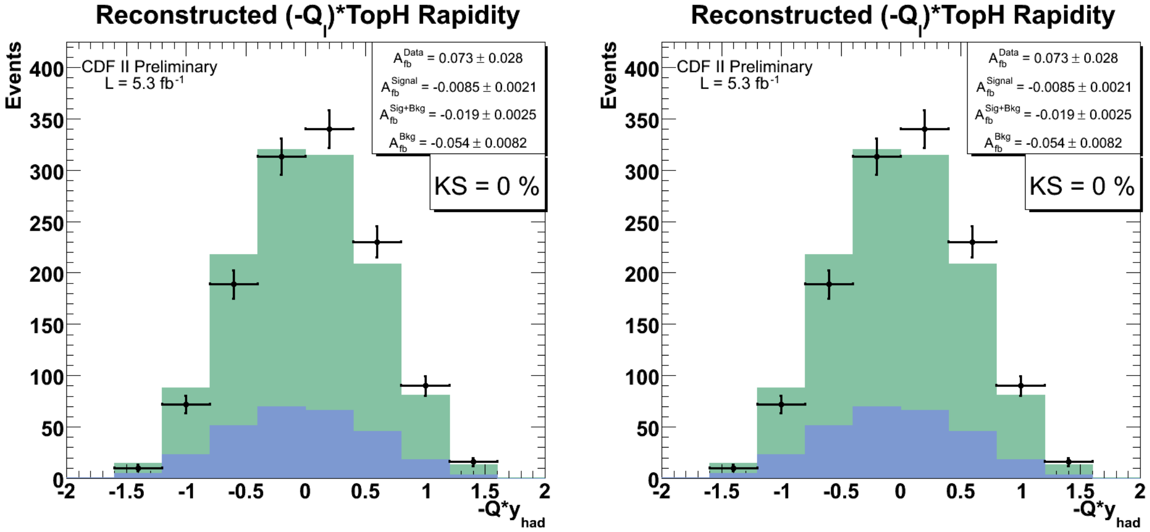

Figure 10: $-\mathrm{q}\cdot\mathrm{y}_{\mathrm{had}}$ and $\mathrm{q}\Delta\mathrm{y}$ Distributions

charge	$A_{fb}(-q\cdot y_{had})$	$A_{fb}(q\Delta y)$
positive (no q weight)	-0.0701 ± 0.0403	-0.0669 ± 0.0403
negative (no q weight)	0.0757 ± 0.0392	0.0479 ± 0.0393
total	0.0730 ± 0.0281	0.0571 ± 0.0281

Table 6: Raw A_{fb} for the $-\mathrm{q}\cdot\mathrm{y}_{\mathrm{had}}$ and $\mathrm{q}\Delta\mathrm{y}$ distributions – see Table 9 for full breakdown

8 Background Subtraction

Non-$t\bar{t}$ events that pass our event selection requirements have a small overall asymmetry (see Figure 11, as well as Table 7 for numbers), and this affects our measured $-q{\cdot}y_{had}$ and $q\Delta y$ distribution shapes. Using the M24U procedure to estimate the overall the shape and size of the background contributions, we can subtract off a total background shape and correct our data back to the signal shape. We note that some background asymmetries can be large, especially for electroweak processes.

A check of the background shapes is available in the antitagged sample, which is deficient in $t\bar{t}$ events, and therefore dominated by the background. In fact, the background to signal ratio in our anti-tagged sample is $2350/669 = 3.5$. Figure 12 shows our anti-tagged data sample compared with the anti-tagged $t\bar{t}$ Pythia signal model (ttop25) and M24U background. We see that signal+background shape has an A_{fb} value of -0.011 ± 0.0028 for $-q{\cdot}y_{had}$, which is in excellent agreement with the value seen for the anti-tagged data, -0.016 ± 0.018. Similarly for $q\Delta y$, we have a signal+background anti-tagged A_{fb} of -0.014 ± 0.0028, comparible to the data value of 0.033 ± 0.018. Additionally, the KS-test values for comparing the data distribution with the signal+background is also very good: 87.6% for $-q{\cdot}y_{had}$ and 32.5% for $q\Delta y$. Now, it is true that the asymmetry is smaller in the anti-tagged sample than the tagged sample accounted for in Table 7. This is because the anti-tags select against the W+HF which has the highest asymmetry. The anti-tags are the control sample we have, and we take the good agreement in the background dominated anti-tags as evidence that the model reproduces the data. Possible model dependence in the shapes and normalizations will be included as systematic uncertainties (see Section 13.1).

It may seem odd that subtracting background generally increases the A_{fb}, even for some positive A_{fb} valued background shapes. This can be explained by the fact that the asymmetry is the difference in forward and background events *divided by the total number of events* – so subtracting off *any* "reasonable" background will increase the magnitude of the data asymmetry. For a quick example, say we have 55 forward events and 45 backward events in the data. This results in a 10% "raw" asymmetry. Now say we have a background of 22 forward events and 20 backward, an asymmetry of ~5%. When we subtract off this background from the data, we are left with 33 forward events and 25 backward, for a final asymmetry of 14%, a significant increase from the original 10%! Subtracting off a negative asymmetry would result in an even larger increase. Thus, we see that background events tend to dilute any real A_{fb}, so any good measurement of a true parton-level A_{fb} must correct for backgrounds.

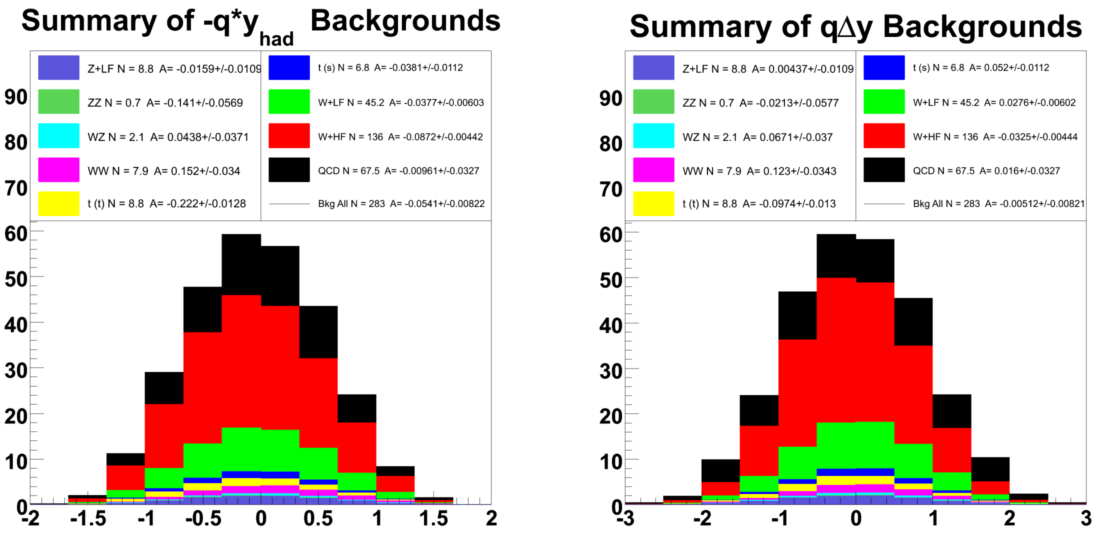

Figure 11: Background Components for $-q \cdot y_{\text{had}}$ and $q\Delta y$

Process	$A_{fb}(-q \cdot y_{\text{had}})$	$A_{fb}(q\Delta y)$
Tagged Non-W (QCD)	-0.0096 ± 0.0327	0.016 ± 0.0327
Tagged W+HF Jets	-0.0872 ± 0.004	-0.0325 ± 0.0044
Tagged W+LF	-0.0377 ± 0.006	0.0276 ± 0.006
Tagged Single Top s	-0.0381 ± 0.0112	0.052 ± 0.0112
Tagged Single Top t	-0.222 ± 0.0128	-0.0974 ± 0.013
Tagged WW	0.152 ± 0.034	0.123 ± 0.0343
Tagged WZ	0.0438 ± 0.0371	0.0671 ± 0.037
Tagged ZZ	-0.141 ± 0.0569	-0.0213 ± 0.0577
Tagged Z+Jets	-0.0159 ± 0.0109	0.0044 ± 0.0109
Total Prediction	-0.0541 ± 0.0082	-0.0051 ± 0.00821

Table 7: Summary of $A_{fb}(-q \cdot y_{\text{had}})$ and $A_{fb}(q\Delta y)$ values for M24U Backgrounds

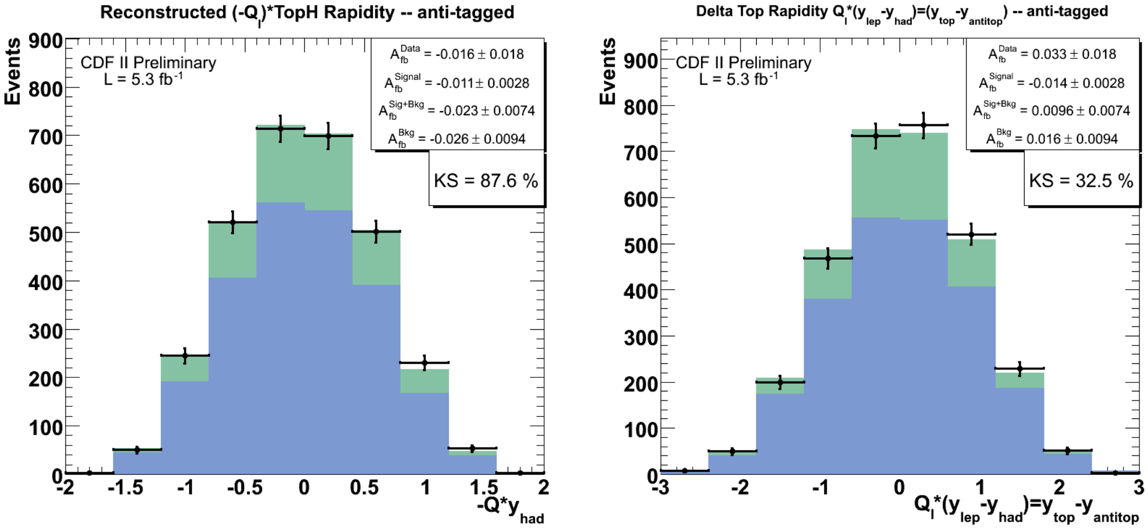

Figure 12: $-q{\cdot}y_{\text{had}}$ and $q\Delta y$ for the antitagged sample

9 Unfold to the Parton Level

In addition to background contributions, we know of two other effects that modify the true $-\mathrm{q}\cdot\mathrm{y}_{\mathrm{had}}$ and $\mathrm{q}\Delta\mathrm{y}$ distributions. First, the kinematic fitter is known to smear out the true rapidities of the reconstructed top quark. We can examine this effect by using the $\mathrm{t\bar{t}}$ Pythia MC sample ttop25 to generate a 2d histogram of $-\mathrm{q}\cdot\mathrm{y}_{\mathrm{had}}{}^{TRUE}$ vs $-\mathrm{q}\cdot\mathrm{y}_{\mathrm{had}}{}^{RECON}$, and an analogous histogram for the variable $\mathrm{q}\Delta\mathrm{y}$. The "smear histogram" N describes the movement of events from bin-to-bin in going from truth to reconstructed data when the kinematic fitter is applied. In Figures 13 and 14, we see a 3d view of the smear histograms N (for $-\mathrm{q}\cdot\mathrm{y}_{\mathrm{had}}$ and $\mathrm{q}\Delta\mathrm{y}$), along with a second view along the diagonal to see the off-diagonal contributions. Note most of the large values lie close to the diagonal, meaning there is little extreme smearing between far-apart bins. We also note that the smear histogram is roughly symmetrical about the diagonal, which shows that smearing *does not cause* an A_{fb} in reconstructed data (if none existed in the true distribution) but rather will dilute any such existing A_{fb} in the truth distribution. After constructing these histograms, we rebin N in exactly the same way as we bin our data, using 4 bins and fixed bin-edges as describe in the next section, and construct a matrix S. Actual values of the rebinned smear matrix S can be seen in Figure 15 and similar values in Equation 17. We show the actual algrebra for constructing matrix S below in Equation 17, and note that it is renormalized and defined in a slightly different way than the recon-vs-true histogram N.

In addition to reconstruction smearing effects, our true distribution is also modified by event selection itself, which cuts out some $\mathrm{t\bar{t}}$ events. If this acceptance is biased with respect to y_{t} (or $\Delta\mathrm{y}$), such bias would cause a change in measured A_{fb}. We look at truth info for events in the MC sample and calculate the ratio of "events passed" to "generated number of events" in each rapidity bin. Using these bin ratios, we can then construct a matrix A whose diagonal entries contain the ratio information, which describes the acceptance bias. Applying the inverse of this matrix A to our data will correct our post-selection-cuts shape to the true pre-cuts shape. We describe this method in detail below, but first we will explain our re-binning procedure.

9.1 Binning

In order to apply matrix-based corrections, it becomes necessary to choose a binning scheme for all histograms and matrices. While using a large bin number allows precision in our understanding of smearing, our correction method is limited by statistics in the data. Using a too-finely binned histogram results in "bin to bin oscillation effects" [2] when applying the unsmearing correction (method explained below). However, using only 2 bins could lead to over- or under-correction of smearing, since we lose information in the original smear matrix. In this case, the corrected data shape would be independent of the actual shape of the data, since it would only include the forward and backward event counts. If the unbinned distribution has more events in the outer edges or near $y = 0$, a 2x2 matrix would not take this into account. In our previous notes [1, 2], we showed that using 4 bins is optimal.

Each distribution has a different range of values. We found that the min and max values of $-\mathrm{q}{\cdot}\mathrm{y}_{\mathrm{had}}$ are roughly $\{-2, 2\}$, so this is the range we use for our data and smearing histograms, making the first and last bins contain the overflow events. For $\mathrm{q}\Delta\mathrm{y}$ we use the range $\{-3, 3\}$. After choosing these boundaries and setting the central bin edges to $y = 0$, this leaves one tunable parameter left: the bin edges at $-\mathrm{q}{\cdot}\mathrm{y}_{\mathrm{had}} = \pm X$ (and $\pm 2X$ for $\mathrm{q}\Delta\mathrm{y}$). We find that adjusting this parameter X influences correction bias effects [1], so we choose a bin edge at $|y| = 0.5$ (for $-\mathrm{q}{\cdot}\mathrm{y}_{\mathrm{had}}$) to minimize this bias effect. This is a slight change from our previous analysis that used a bin edge at $|y| = 0.4$. We chose this new bin edge to preserve the fact that $\mathrm{y}_{\mathrm{had}}$ is 1/2 of the magnitude of $\Delta\mathrm{y}$, and the best bin edge for $\mathrm{q}\Delta\mathrm{y}$ was found to be at $|\Delta\mathrm{y}| = 1.0$, rather than $|\Delta\mathrm{y}| = 0.8$.

Choosing different values for our bin edges can result in different measurements for raw and corrected A_{fb} values, partly due to fluctuations in the bins as well as due to changes in the smear and acceptance matrices used for our correction procedure. To account for these differences we will include "bin-edge" as one of our systematic uncertainties, as explained in Section 13.

9.2 Correction Using Inverse Matrices

In order to correct for smearing, we construct a 4x4 matrix S from the truth-vs-recon matrix and binning choice explained above. The entries of S are

$$S_{ij} = N^{ij}_{recon}/N^{i}_{truth} \tag{13}$$

where N^{ij} is the number of events in the smear matrix with i is the truth bin index and j the reconstructed bin index. N^{i} is the value of bin i of the truth histogram, the projection of N^{ij}, used to properly normalize the matrix (so entries are in the form of a smear ratio in terms of the original number of truth entries). We note here that Figure 15 above is a representation of array N, whereas Equation 17 is matrix S, and Figure 16 is a graphical representation of the unfold matrix, which uses S, not N.

In addition to smearing, we also know that selection cuts remove a number of $\mathrm{t}\bar{\mathrm{t}}$ events from our analysis. These removed events may have a different asymmetry than the remaining events, so to correct our raw asymmetry we apply the inverse of an acceptance matrix

$$A_{ii} = N^{i}_{selection}/N^{i}_{generated} \tag{14}$$

Where A only has diagonal terms with values equaling the ratio of number of events selected over the total number, using the same 4x4 binning scheme as the data and

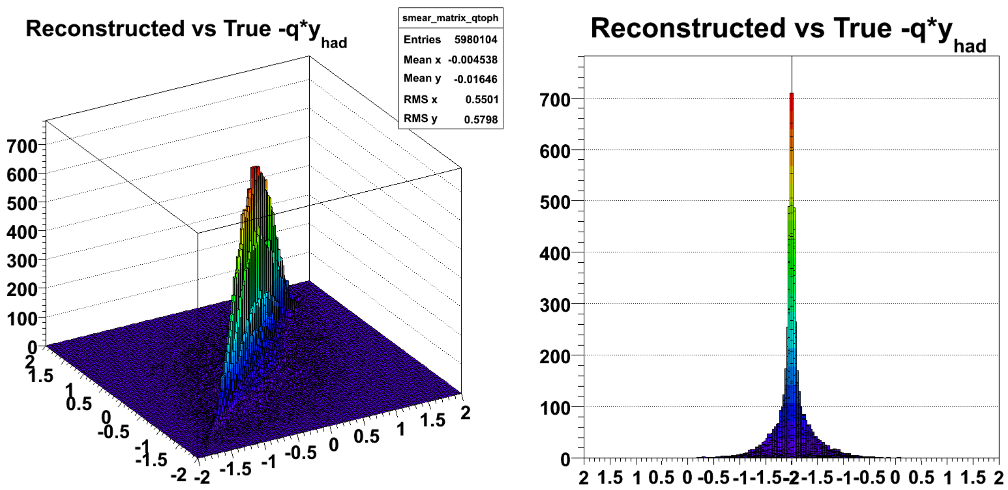

Figure 13: 3d plot of the $-\mathrm{q}\cdot\mathrm{y}_{\mathrm{had}}$ 2d smear histogram N, and a diagonal view

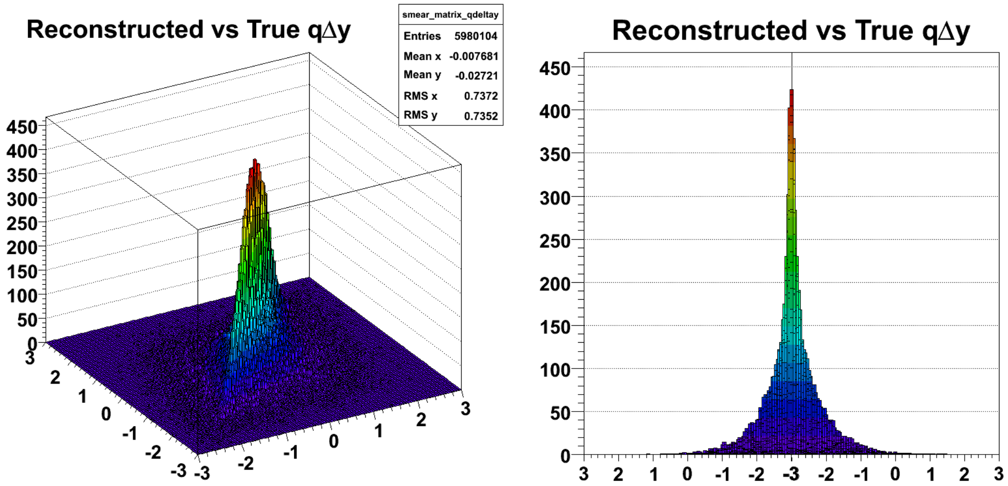

Figure 14: 3d plot of the $\mathrm{q}\Delta\mathrm{y}$ 2d smear histogram N, and a diagonal view

smear matrices.

So we see that if we start with a true distribution of $-\mathrm{q}\cdot\mathrm{y}_{\mathrm{had}}$ or $\mathrm{q}\Delta\mathrm{y}$, the distribution is first modified by selection, then smearing, then background (Equation 15). We find our final "parton-level" A_{fb} values by correcting for these effects *in reverse order*.

$$\begin{aligned} N_{raw} &= [S\cdot(A\cdot N_{true})] + N_{bkg} \qquad (15)\\ N_{corrected} &= A^{-1}\cdot S^{-1}\cdot N_{raw-bkg} \qquad (16)\end{aligned}$$

where N is a vector whose values are the number of events in each bin of our $-\mathrm{q}\cdot\mathrm{y}_{\mathrm{had}}$ distribution. That is, N_{raw} is a column vector containing the number of bin entries for the reconstructed $-\mathrm{q}\cdot\mathrm{y}_{\mathrm{had}}$ data, and $N_{corrected}$ is an analogous vector after unfolding.

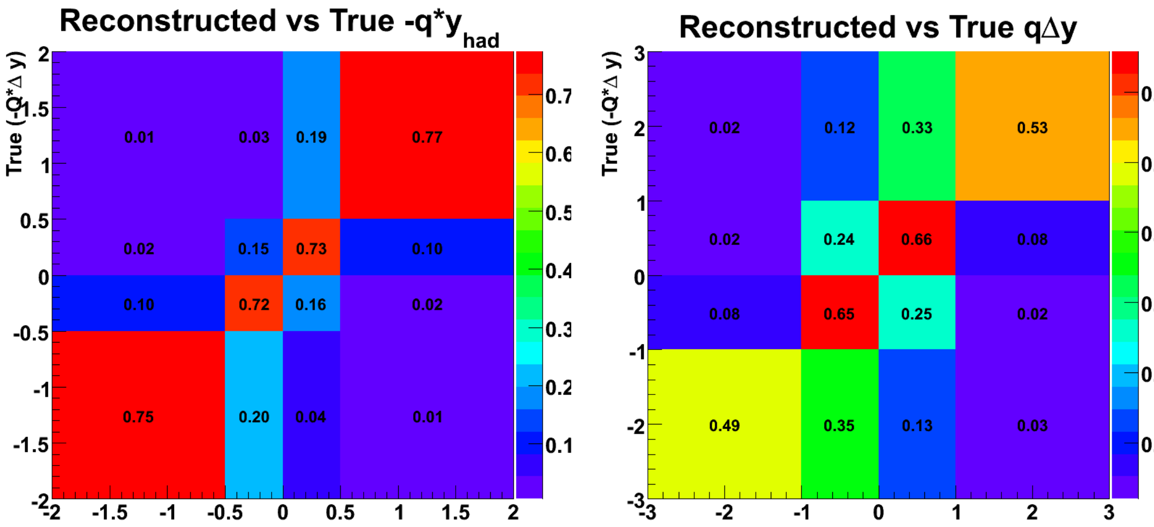

Figure 15: Smear matrices (S) for $-\mathrm{q}\cdot\mathrm{y}_{\mathrm{had}}$ and $\mathrm{q}\Delta\mathrm{y}$, after rebinning according to prescription in Section 9.1

The smear matrix we use is calculated from $\mathrm{t}\bar{\mathrm{t}}$ ttop25 Pythia MC and is

$$S_{-\mathrm{q}\cdot\mathrm{y}_{\mathrm{had}}} = \begin{bmatrix} 0.7455 \pm 0.0092 & 0.0988 \pm 0.0028 & 0.0189 \pm 0.0012 & 0.0055 \pm 0.0008 \\ 0.2028 \pm 0.0047 & 0.7192 \pm 0.0076 & 0.1519 \pm 0.0035 & 0.0338 \pm 0.0020 \\ 0.0437 \pm 0.0022 & 0.1603 \pm 0.0036 & 0.7329 \pm 0.0078 & 0.1869 \pm 0.0047 \\ 0.0080 \pm 0.0009 & 0.0217 \pm 0.0013 & 0.0963 \pm 0.0028 & 0.7738 \pm 0.0097 \end{bmatrix} \tag{17}$$

$$S_{\mathrm{q}\Delta\mathrm{y}} = \begin{bmatrix} 0.4890 \pm 0.0112 & 0.0775 \pm 0.0021 & 0.0223 \pm 0.0011 & 0.0206 \pm 0.0024 \\ 0.3516 \pm 0.0094 & 0.6519 \pm 0.0061 & 0.2443 \pm 0.0038 & 0.1199 \pm 0.0059 \\ 0.1336 \pm 0.0057 & 0.2465 \pm 0.0037 & 0.6576 \pm 0.0063 & 0.3274 \pm 0.0098 \\ 0.0258 \pm 0.0025 & 0.0241 \pm 0.0012 & 0.0757 \pm 0.0021 & 0.5321 \pm 0.0126 \end{bmatrix} \tag{18}$$

Using this same MC sample, we find from comparing the event counts before and after cuts that

$$A_{-\mathrm{q}\cdot\mathrm{y}_{\mathrm{had}}} = \begin{bmatrix} 0.9536 \pm 0.0045 & 0 \pm 0 & 0 \pm 0 & 0 \pm 0 \\ 0 \pm 0 & 1.0776 \pm 0.0043 & 0 \pm 0 & 0 \pm 0 \\ 0 \pm 0 & 0 \pm 0 & 1.0552 \pm 0.0043 & 0 \pm 0 \\ 0 \pm 0 & 0 \pm 0 & 0 \pm 0 & 0.8840 \pm 0.0044 \end{bmatrix} \tag{19}$$

$$A_{\mathrm{q}\Delta\mathrm{y}} = \begin{bmatrix} 0.8400 \pm 0.0060 & 0 \pm 0 & 0 \pm 0 & 0 \pm 0 \\ 0 \pm 0 & 1.0870 \pm 0.0037 & 0 \pm 0 & 0 \pm 0 \\ 0 \pm 0 & 0 \pm 0 & 1.0408 \pm 0.0036 & 0 \pm 0 \\ 0 \pm 0 & 0 \pm 0 & 0 \pm 0 & 0.7247 \pm 0.0056 \end{bmatrix} \tag{20}$$

Note that neither the S nor A matrices are expected to be unitary, therefore we are unconcerned with array values greater than 1. In fact, because the acceptance ratio (selected/generated) is actually small, we normalize the above matrices to values near 1 in order to easily analyze number trends.

Using these matrices, we find a final correction unfold matrices

$$A^{-1} \cdot S^{-1}(-\mathrm{q{\cdot}y_{had}}) = \begin{bmatrix} 1.4614 & -0.2016 & 0.0044 & -0.0027 \\ -0.3652 & 1.4030 & -0.2826 & 0.0097 \\ 0.0037 & -0.3023 & 1.3983 & -0.3246 \\ -0.0044 & -0.0009 & -0.1981 & 1.5098 \end{bmatrix} \tag{21}$$

$$A^{-1} \cdot S^{-1}(\mathrm{q\Delta y}) = \begin{bmatrix} 2.6638 & -0.3291 & 0.0378 & -0.0522 \\ -1.1096 & 1.7791 & -0.6265 & 0.0274 \\ 0.0249 & -0.6532 & 1.8146 & -0.9703 \\ -0.0791 & 0.0309 & -0.3303 & 2.7926 \end{bmatrix} \tag{22}$$

We drop the statistical error in the unsmearing matrix at this point, as it is negligible compared to the overall matrix entry values. In the next section, we explain how errors are propagated for the corrected distribution shape. We see that small statistical errors in the unsmearing matrix would enter only as second-order effects and therefore are negligible compared to the data-background statistical errors and first-order error effects from the correction procedure. In Figure 16 we see a graphical representation of the above unsmearing correction matrices. Note that these matrices have large values along the diagonal entries and much smaller values for far off-diagonal entries. This shows us that smearing occurs mostly for events close to the bin edges in our rebinned distribution. The near-symmetry of these numbers is indicative that the correction procedure should not bias the $\mathrm{A_{fb}}$ value.

Again, we note that the $A^{-1} \cdot S^{-1}$ matrix is not expected to be unitary.

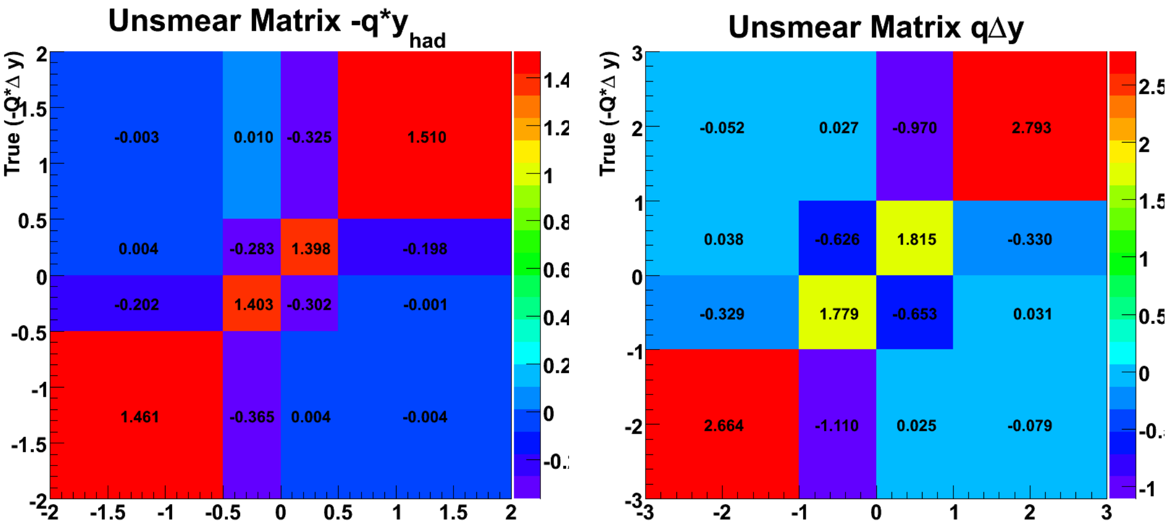

Figure 16: Correction Matrix $A^{-1} \cdot S^{-1}$ for $-\mathrm{q}{\cdot}\mathrm{y}_{\mathrm{had}}$

9.3 Error Propagation

The following section follows exactly the prescription in reference [2].

With the understanding of acceptance and reconstruction bias in hand, we can develop an overall formalism for correcting the measured A_{fb} back to the true A_{fb} of $\mathrm{t\bar{t}}$ production. Matrices A and S are multiplied together to create a relationship between the background corrected number of forward and backward events and the true number of forward and backward events generated in Monte Carlo. We will call the corrected values that are comparable to the number of events generated $N_{corrected}$.

$$N_{bkg-sub} = S \cdot A \cdot N_{truth} \tag{23}$$

The combined matrix formed by multiplication of A and S is then inverted so that we can solve for the corrected values.

$$N_{corrected} = A^{-1} \cdot S^{-1} \cdot N_{bkg-sub} \tag{24}$$

This technique is used to calculate the final corrected asymmetry that may be compared to theoretical prediction. The forward backward asymmetry is calculated as follows. Let,

$$\alpha = [1, 1, ..., 1, 1] \tag{25}$$

$$\zeta = [1, 1, ...1, -1, ..., -1, -1] \tag{26}$$

Then

$$\mathrm{A_{fb}} = \frac{\zeta \cdot N_{corrected}}{\alpha \cdot N_{corrected}} \tag{27}$$

The uncertainty on this equation is slightly more complicated. To simplify some algebra let:

$$\begin{aligned} N &= N_{corr} && (28) \\ n &= N_{bkg-sub} && (29) \\ M &= A^{-1} \cdot S^{-1} && (30) \end{aligned}$$

So,

$$N = M \cdot n \tag{31}$$

is equivalent to Equation 24. $\mathrm{A_{fb}}$ can then be represented as a sum:

$$\mathrm{A_{fb}} = \frac{\sum_i \zeta_i \sum_j^{nbins} M_{i,j} \cdot n_j}{\sum_i \alpha_i \sum_j^{nbins} M_{i,j} \cdot n_j} \tag{32}$$

Now we just perform simple error propagation:

$$\sigma^2_{\mathrm{A_{fb}}} = \sum_i \sigma^2_{n_i} \cdot \left(\frac{\delta \mathrm{A_{fb}}}{\delta n_i} \right)^2 \tag{33}$$

where, σ_{n_i} = the statistical uncertainty in bin “i” for background corrected data and,

$$\frac{\delta \mathrm{A_{fb}}}{\delta n_x} = \frac{(\sum_i \zeta_i \cdot M_{i,x}) \cdot (\alpha \cdot N) - (\sum_i \alpha_i \cdot M_{i,x}) \cdot (\zeta \cdot N)}{(\alpha \cdot N)^2} \tag{34}$$

Note that we use analogous formalism to calculate the propagated error for $\mathrm{A_{fb}}(\Delta \mathrm{y})$, described in detail in Section 10

9.4 Unfold Correction Bias Check

In our previous note [1], we examined the validity of our unfold correction method by examining pseudoexperiments, checking that correcting the distributions resulted in a pull distribution centered at 0 with a width of 1. We repeated this test for this analysis using our new MC sample ctopo3/madgraph for our initial distribution, corrected with ttop25. By running pseudoexperiments on ctopo3 and measuring the pull distribution, we are able to validate that our method does correct reconstructed distributions back to parton-level truth values, and that our error propagation is also correct. That is, a good correction method results in a Gaussian-shaped pull distribution, centered at 0, having a width of 1. From Figure 20, we see that our pull distribution is centered at 0.6967 ???? and has a width of 1.004 ?????. The fact that the width is near 1 indicates that our propagation of statistical errors has been handled correctly. The slight "bias" in the pull distributions is partially due to the fact that ctopo3 is not truly representative of standard model top physics, and we plan to repeat these pseudoexperiments with an MC@NLO sample when one becomes available. We also note that the ctopo3 sample has very large MC statistics and therefore small relative errors for bin counts, resulting in a magnification of any small bias. Using a MC sample scaled to the number of events in the data (1260) results in pull centers closer to 0.

Also in our previously note, we additionally created a series of distributions having fixed A_{fb} values in both truth and reconstructed distributions. This was accomplished by using the ttkt74 Pythia MC sample (so as to be uncorrelated with the unfold sample), finding the true $-q \cdot \cos(\theta)$ distribution in the $t\bar{t}$ frame, linearly reweighting it to a non-zero A_{fb} value, and propagating the reweighted distribution to $-q{\cdot}y_{had}$ in the lab frame (the full details are described in detail in Reference [1]). These distributions were unfolded and compared with the true A_{fb} for each test. We plotted the true-vs-recon A_{fb} values on a plot, which we have reproduced here in Figure 17. We note that the linearity of this plot shows the validity of our method for a large range of A_{fb} values and has little bias. Please see our note for a full explanation of this validation method, as we do not repeat it with the MC samples used in this note.

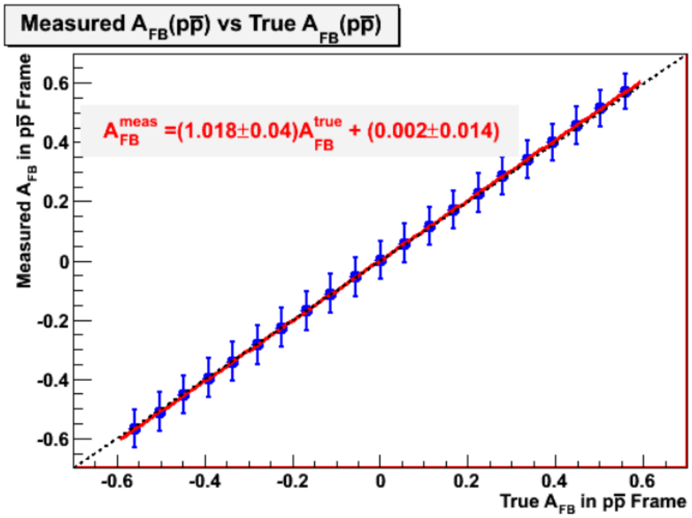

Figure 17: Measured (corrected) A_{fb} vs True A_{fb} for reweighted ttkt74, unfolded with ttop75. Reproduced from Reference [1]

9.5 Application of the Correction Method

Before accepting the above correction method, we first need to validate its effect on samples with known asymmetry. This will be explained in the following section. However, we wish to first demonstrate our correction procedure graphically by presenting the $-\mathrm{q}\cdot\mathrm{y}_{\mathrm{had}}$ and $\mathrm{q}\Delta\mathrm{y}$ distributions at various stages of correction.

Figure 18 shows the changes in the $-\mathrm{q}\cdot\mathrm{y}_{\mathrm{had}}$ distribution as we apply corrections. The black line histogram is the raw data distribution. Subtracting off the M24U background yields the green-colored histogram, and after applying the inverse matrices $A^{-1} \cdot S^{-1}$, we arrive at the final corrected red-colored histogram. The solid light-green histogram is the $\mathrm{t}\bar{\mathrm{t}}$ Pythia MC sample ttop25, normalized to have the same number of events as the background-subtracted data, so that we can compare the measured background-subtracted sample to a standard model prediction. We see that the data exhibit an asymmetry larger than that predicted by ttop25. This correction process will be repeated in our final measurement section where we will present the calculated A_{fb} values for $-\mathrm{q}\cdot\mathrm{y}_{\mathrm{had}}$ and $\mathrm{q}\Delta\mathrm{y}$.

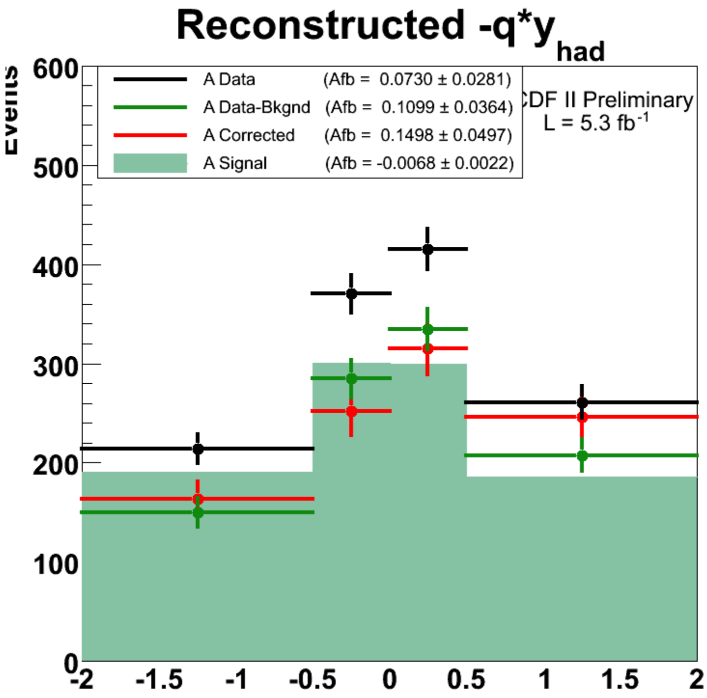

Figure 18: $-q{\cdot}y_{\rm had}$ raw data (black), data-background (green line), corrected data (red) and the signal MC prediction (solid light-green) to compare with data-background.

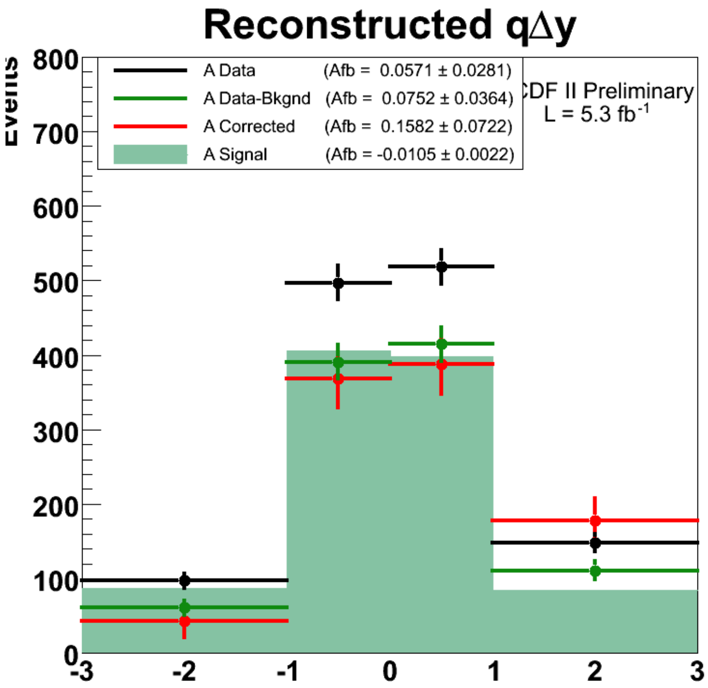

Figure 19: Unfold for qΔy

10 $\mathrm{A_{fb}}(\Delta\mathrm{y})$ Measurement

Using the raw, background-subtracted, and corrected bin values in the histograms above, we are now ready to calculate $\mathrm{A_{fb}}(\Delta\mathrm{y})$. Because this calculation is simply a bin-wise asymmetry, we look at the inner and outer bin pairs of the $\mathrm{q}\Delta\mathrm{y}$ distributions and calculate

$$\mathrm{A_{fb}}(\Delta\mathrm{y_i}) = \frac{\mathrm{N}(\Delta\mathrm{y_i}) - \mathrm{N}(-\Delta\mathrm{y_i})}{\mathrm{N}(\Delta\mathrm{y_i}) + \mathrm{N}(-\Delta\mathrm{y_i})} \tag{35}$$

where $\Delta\mathrm{y_i}$ and $-\Delta\mathrm{y_i}$ represent the forward and backward bins of either the inner or outer bin pair. We note that this is equivalent to using equation 27 (or equation 32) after substituting a different definition of α and ζ

$$\alpha^{\mathrm{inner}} = [0,1,1,0] \tag{36}$$
$$\alpha^{\mathrm{outer}} = [1,0,0,1] \tag{37}$$
$$\zeta^{\mathrm{inner}} = [0,1,-1,0] \tag{38}$$
$$\zeta^{\mathrm{outer}} = [1,0,0,-1] \tag{39}$$

$$A^k_{fb} = \frac{\sum_i \zeta^k_i \sum_j^{nbins} M_{i,j} \cdot n_j}{\sum_i \alpha^k_i \sum_j^{nbins} M_{i,j} \cdot n_j} \tag{40}$$

where k is "inner" or "outer".

Using this definition we are additionally able to calculate the propagation of statistical errors. We substitute the α and ζ above into equations 33 and 34

$$\sigma^2_{\mathrm{A_{fb}}}{}^k = \sum_i \sigma^2_{n_i} \cdot \left(\frac{\delta A^k_{fb}}{\delta n_i}\right)^2 \tag{41}$$

where, σ_{n_i} = the statistical uncertainty in bin "i" for background corrected data and,

$$\frac{\delta A^k_{fb}}{\delta n_x} = \frac{\left(\sum_i \zeta^k_i \cdot M_{i,x}\right)\cdot\left(\alpha^k \cdot N\right) - \left(\sum_i \alpha^k_i \cdot M_{i,x}\right)\cdot\left(\zeta^k \cdot N\right)}{\left(\alpha^k \cdot N\right)^2} \tag{42}$$

Note that the sum in equation 41 is still over *all* background-subtracted bins. This is because every bin contributes to the final corrected value through the correlations recorded in the smear matrix M. By using α^k and ζ^k we correctly use the components from the smear matrix and background-subtracted data vector to find the propagated error. As a test of this new formula, we ran pseudoexperiments and recorded the $\mathrm{A_{fb}}$, error, and pull distributions for the inclusive sample and each $\Delta\mathrm{y}$ bin. The results of these experiments show that our method indeed works. See Figures 20 through 22. Because the widths of the pull distributions are all near 1, this indicates that our propagation of statistical errors was handled correctly, even for unfolded $\mathrm{A_{fb}}$ values in the $\mathrm{A_{fb}}(\Delta\mathrm{y})$ measurement. The slight "bias" in the pull distributions is partially due to the fact that ctopo3 is not truly representative of standard model top physics, and we plan to repeat these pseudoexperiments with an MC@NLO sample when one becomes available. We also note that the ctopo3 sample has very large MC statistics and therefore small relative errors for bin counts, resulting in a magnification of any small bias. Using a MC sample scaled to the number of events in the data (1260) results in pull centers closer to 0.

Using the same style as the graphical unfold plots for the inclusive and rapidity-dependence $\mathrm{A_{fb}}$ measurements, in Figure 23 we see that ctopo3 is correctly unfolded (using ttop25) in the outer rapidity bin to the truth value (the cyan histogram). Looking at data, we show in Figure 24 the raw, data-background, and corrected values for $\mathrm{A_{fb}}(\Delta\mathrm{y})$. Note that the slope of the plot shows higher $\mathrm{A_{fb}}$ values for the outer rapidity bins, similar to the MCFM prediction in Figure 4. We note that the raw $\mathrm{A_{fb}}(\Delta\mathrm{y})$ is already very high in the outer bin, that subtracting off the background contribution raises the $\mathrm{A_{fb}}$ value even more, and that the corrected $\mathrm{A_{fb}}$ value is very high in the outer bin ($> 60\%$). These corrected values are to be compared with the MCFM model predictions of 0.039 ± 0.006 and 0.123 ± 0.018 for the inner and outer rapidities, respectively.

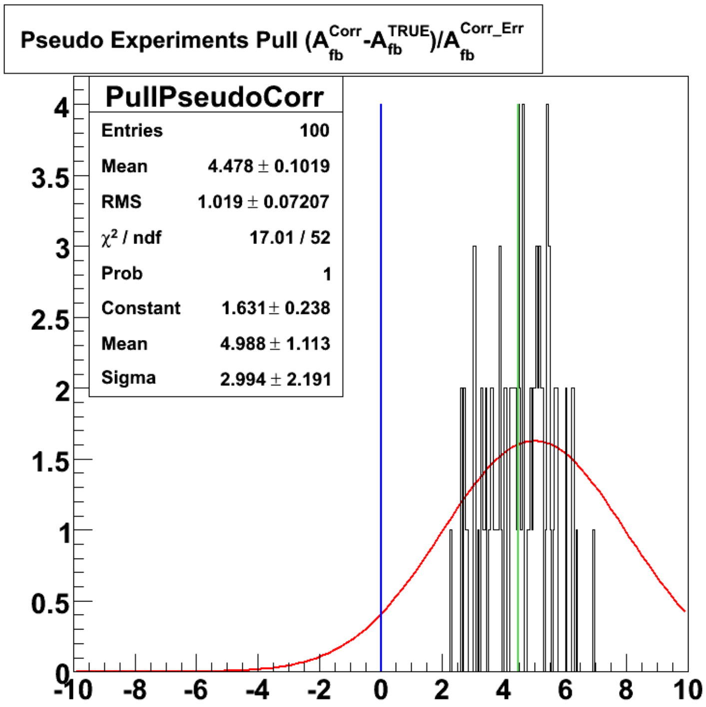

Figure 20: 20000 Pseudo-experiments for qΔy (inclusive)
Note that the pull has a width near 1,
indicating that our propagated errors are correct.

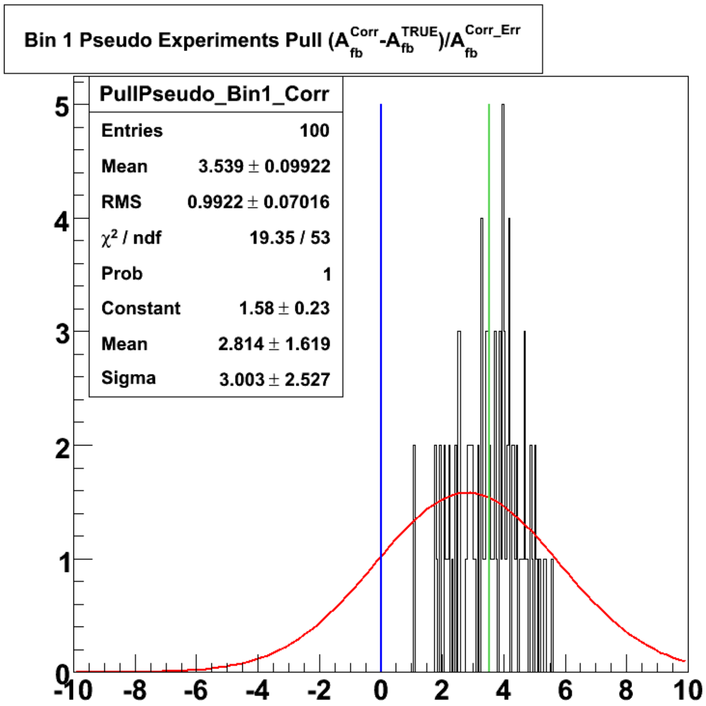

Figure 21: 20000 Pseudo-experiments for qΔy (inner bins) Note that the width of the pull is near 1, but it is not centered at 0. This indicates a possible slight bias in the inner bin $A_{fb}(\Delta y)$ measurement for corrected A_{fb}.

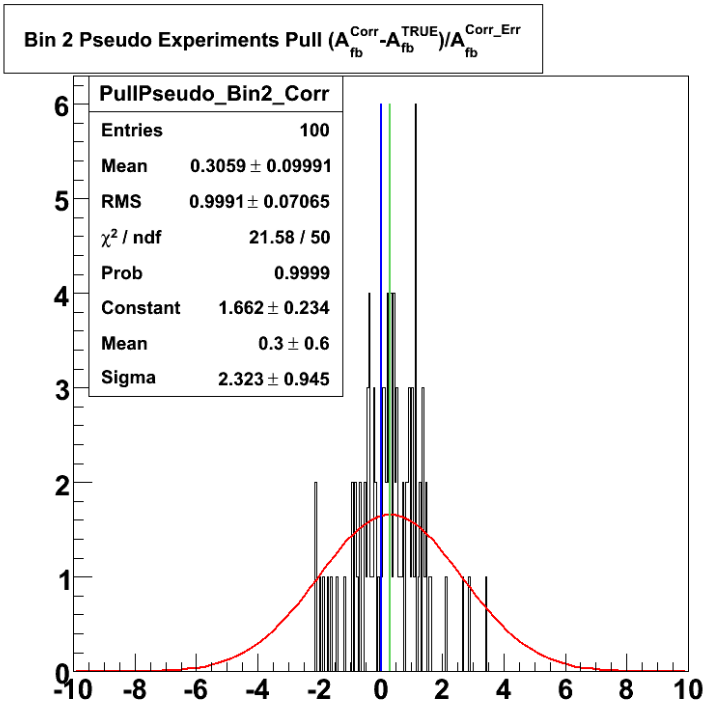

Figure 22: 20000 Pseudo-experiments for qΔy (outer bins) Note that the pull is centered near 0 and has a width near 1, indicating a good measurement.

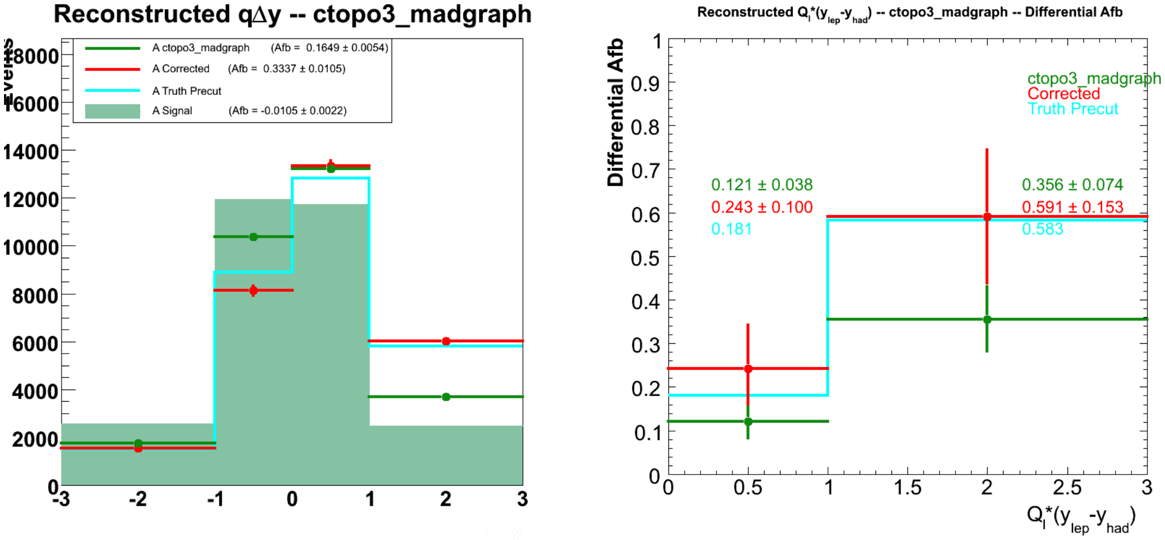

Figure 23: Inclusive $A_{fb}(q\Delta y)$ and $A_{fb}(\Delta y)$ distributions for ctopo3/madgraph

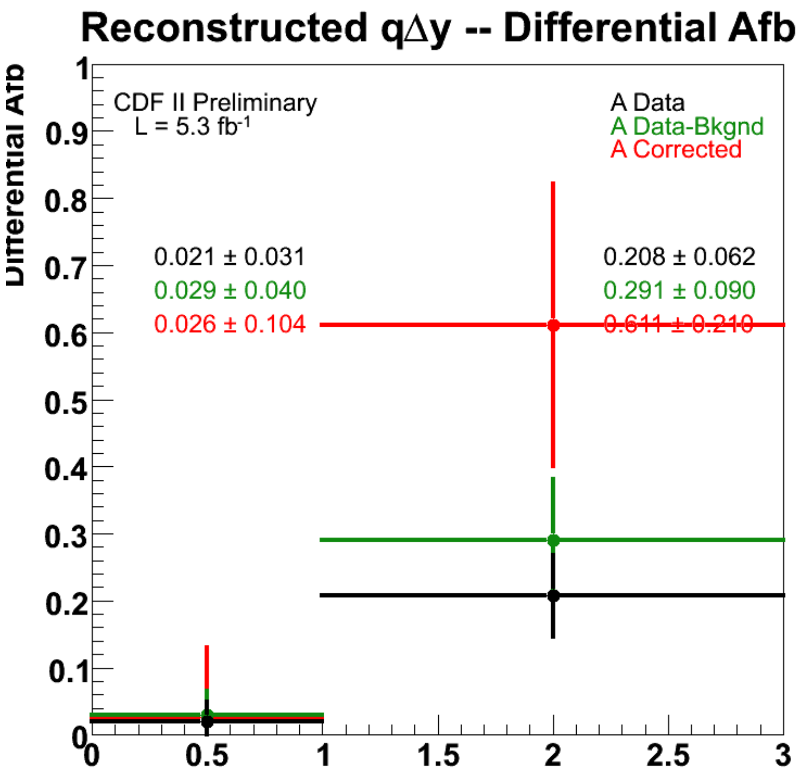

Figure 24: Raw, Data-Background, and Corrected $A_{fb}(\Delta y)$ for data

11 Initial Measurement

Having validated our data and backgrounds and checked the validity of our correction procedure, we are now ready to calculate a corrected $\mathrm{A_{fb}}$ from our data. See Figure 10 for our $-\mathrm{q}\cdot\mathrm{y_{had}}$ raw distribution, which has an initial asymmetry of

$$A_{fb}^{raw} = 0.073 \pm 0.028 \tag{43}$$

We subtract off the background events, which have an $\mathrm{A_{fb}}$ of -0.054 ± 0.018, calculating an intermediate corrected data asymmetry of

$$A_{fb}^{raw-bkg} = 0.110 \pm 0.036 \tag{44}$$

Applying our unsmearing correction procedure as explained in Section 9, using the $A^{-1} \cdot S^{-1}$ correction matrix in Equation 21, and propagating error as explained in section 9.3, we arrive at a final corrected asymmetry measurement of

$$A_{fb}^{corrected} = 0.150 \pm 0.050 \tag{45}$$

See Figure 18 in Section 9.5 for a graphical representation of the angular distribution's evolution with the application of our correction procedure.

For the $\mathrm{t\bar{t}}$ rest frame calculation, we use the variable $\mathrm{q\Delta y}$ for our data histograms and unsmearing variables. Using the method explained, we find the following values:

	$\mathrm{A_{fb}}(-\mathrm{q}\cdot\mathrm{y_{had}})$	$\mathrm{A_{fb}}(\mathrm{q\Delta y})$	Inner $\mathrm{A_{fb}}$ ($\lvert\Delta\mathrm{y}\rvert < 1.0$)	Outer $\mathrm{A_{fb}}$ ($\lvert\Delta\mathrm{y}\rvert > 1.0$)
Raw	0.073 ± 0.028	0.057 ± 0.028	0.021 ± 0.031	0.208 ± 0.062
Raw-Bkg	0.110 ± 0.036	0.075 ± 0.036	0.029 ± 0.040	0.291 ± 0.090
Corrected	0.150 ± 0.050	0.158 ± 0.072	0.026 ± 0.104	0.611 ± 0.210

Table 8: $\mathrm{A_{fb}}$ Values for $-\mathrm{q}\cdot\mathrm{y_{had}}$, $\mathrm{q\Delta y}$, and $\mathrm{A_{fb}}(\Delta\mathrm{y})$ before Systematic Uncertainties

12 Cross Checks

In order to believe our measured A_{fb} value is indicative of real physics and is not a detector effect or statistical anomaly, we wish to measure the raw A_{fb} of various subsamples. In Figure 29 we show the $-q{\cdot}y_{had}$ angular distribution for data, background, and signal for events containing a CEM, CMUP, or CMX lepton. We see that the raw A_{fb} values for each subsample are consistent within statistical error. Similarly we compare samples made distinct by lepton charge, number of tags, and number of jets (Figures 25 through 31). We summarize the numerical values below in Table 9.

		$A_{-q\cdot y_{had}}$	$A_{q\Delta y}$
1	inclusive tagged	0.0730 ± 0.0281	0.0571 ± 0.0281
2	pos lep (no q weight)	-0.0701 ± 0.0403	-0.0669 ± 0.0403
3	neg lep (no q weight)	0.0757 ± 0.0392	0.0479 ± 0.0393
4	$\chi^2 \leq 9$	0.0924 ± 0.0370	0.0428 ± 0.0371
5	$\chi^2 > 9$	0.0467 ± 0.0432	0.0766 ± 0.0431
6	p0-19 (3.4 fb^{-1})	0.1042 ± 0.0357	0.0708 ± 0.0358
7	p20-27 (2.1 fb^{-1})	0.0228 ± 0.0455	0.0352 ± 0.0455
8	CEM	0.0531 ± 0.0368	0.0259 ± 0.0369
9	CMUP	0.1325 ± 0.0544	0.1265 ± 0.0544
10	CMX	0.0466 ± 0.0719	0.0570 ± 0.0719
11	nJet = 4	0.0756 ± 0.0325	0.0650 ± 0.0326
12	nJet ≥ 5	0.0654 ± 0.0557	0.0343 ± 0.0558
13	pretagged	0.0105 ± 0.0153	0.0404 ± 0.0153
14	single tagged	0.0950 ± 0.0318	0.0582 ± 0.0319
15	double tagged	-0.0036 ± 0.0597	0.0534 ± 0.0596

Table 9: The asymmetry in $A_{fb}(-q{\cdot}y_{had})$ and $A_{fb}(q\Delta y)$ for various selections

We now examine the stability and robustness of the inclusive asymmetries against simple variations of the selection and reconstruction. A proper comparison of a real $t\bar{t}$ effect across these selections should employ a background subtraction in order to establish a pure $t\bar{t}$ signal. But because we wish to avoid any assumptions at this stage, we perform these cross-checks using the inclusive lepton+jets data.

For each selection or reconstruction variation, we look at both asymmetries, $A_{fb}^{-q\cdot y_{had}}$ and $A_{fb}^{q\Delta y}$ (A_{fb}^{lab} and $A_{fb}^{t\bar{t}}$). A summary of all the results is given in Table 9.

12.1 Frame

Row 1 shows the asymmetry in the two frames. The ratio in the data is $A_{fb}^{t\bar{t}}/A_{fb}^{lab} = 1.05 \pm 0.60$, where the uncertainty assumes the asymmetries are independent, and is therefore an over-estimate. The MCFM calculation for this ratio in the NLO QCD effect is $A_{fb}^{t\bar{t}}/A_{fb}^{lab}$ =????. In the Madgraph coloron sample ctopo3, we find $A_{fb}^{t\bar{t}}/A_{fb}^{lab} = 1.80 \pm 0.09$ from corrected reconstructed values and 1.42 ± 0.01 from truth. The data ratio is smaller than these predictions but compatible within uncertainties.

12.2 Charge

Rows 2-3 show the unsigned asymmetry variables when the data is divided by lepton charge. Leaving the top quark aside, these are charge asymmetries in the rapidity of the hadronic system in the lab, and in the rapidity difference between the leptonic and hadronic system. For both variables, the asymmetries in the separate charge species are equal and opposite, within error. This sign change under interchange of "leptonic" and "hadronic", or equivalently, the exchange of t and $\bar{t}$, is as expected from a CP-conserving asymmetry. If the asymmetry is due to the detector or reconstruction effect, that effect must link the sign of the rapidity distortion with the sign of the lepton charge in the CP conserving way. This is puzzling because the $t\bar{t}$ reconstruction uses only mass constraints, the sign of the lepton does not enter the algorithm in any way.

A number of small charge asymmetries are known to exist in the W+jets samples, but they are all counting asymmetries [12]. A counting asymmetry in the charge would affect the relative size of the populations and the total inclusive efficiency of the combined sample, but would not affect the separately measured efficiency for each charge species.

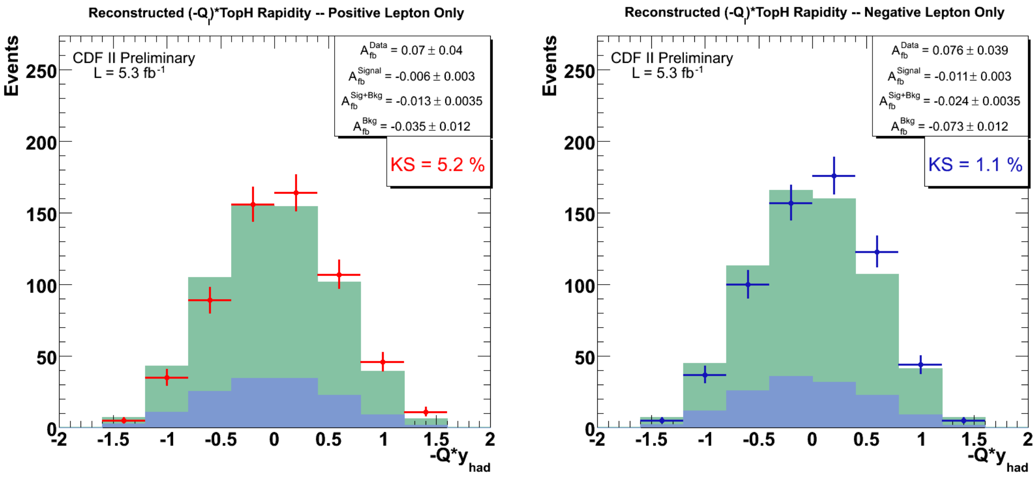

Figure 25: $-q \cdot y_{had}$ split for positive and negative lepton events

12.3 χ^2

Rows 4-5 show the asymmetries when the data is partitioned by a cut on the reconstruction quality at $\chi^2 = 9.0$, the value established and used in the top mass analysis. As seen in Figure 36, this cut restricts the sample to the peak in the distribution. There

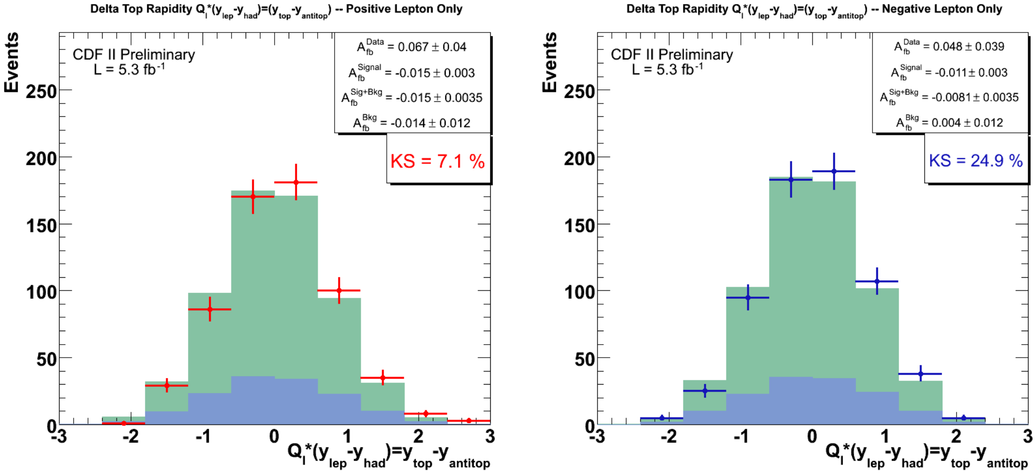

Figure 26: qΔy split for positive and negative lepton events

are 725 events out of 1260 with $\chi^2 \leq 9$. In this high quality reconstruction sample, $\mathrm{A}_{\mathrm{fb}}^{\mathrm{t\bar{t}}}$ is diminished to 1σ significance, but $\mathrm{A}_{\mathrm{fb}}^{\mathrm{lab}}$ grows in significance. Both values are statistically compatible with the result in the full sample. We will keep an eye on the χ^2 in $\mathrm{A}_{\mathrm{fb}}^{\mathrm{t\bar{t}}}$ but the data seem to suggest that the asymmetry is not associated with bad reconstructions that show up as large χ^2.

12.4 Run Range

Rows 6-7 show the asymmetries when the data is divided into an early and a later part. We see that $\mathrm{A}_{\mathrm{fb}}^{\mathrm{t\bar{t}}}$ is stable but that in the newer data $\mathrm{A}_{\mathrm{fb}}^{\mathrm{t\bar{t}}}$ drops to zero. The stability of the former might suggest that the latter is a fluctuation, and, indeed, the $\mathrm{A}_{\mathrm{fb}}^{\mathrm{t\bar{t}}}$ in the two data periods are consistent within 1σ. However, we also know that in p18 there was a version change in the reconstruction that affected primary vertexing and silicon hit finding [18]. It is conceivable that incorrect primary vertices could create a direction bias in the reconstruction and/or that changes in b-tagging associated with silicon hit finding could create distortions in the reconstruction. Dividing the dataset into two parts at p19 is made with this concern in mind.

asymmetry	all data	p0-19 (3.4 fb^{-1})	p20-27 (2.1 fb^{-1})
$\mathrm{A}_{\mathrm{fb}}^{\mathrm{tt}}$	$+0.057 \pm 0.028$	$+0.071 \pm 0.036$	$+0.035 \pm 0.046$
$A_{\mathrm{t\bar{t}}}^{+}$	-0.067 ± 0.040	$+0.095 \pm 0.053$	-0.030 ± 0.061
$A_{\mathrm{t\bar{t}}}^{-}$	$+0.048 \pm 0.039$	-0.051 ± 0.048	$+0.041 \pm 0.068$
$\mathrm{A}_{\mathrm{fb}}^{\mathrm{lab}}$	$+0.073 \pm 0.028$	$+0.104 \pm 0.036$	$+0.023 \pm 0.046$
A_{lab}^{+}	-0.070 ± 0.040	-0.130 ± 0.053	$+0.008 \pm 0.061$
A_{lab}^{-}	$+0.076 \pm 0.043$	$+0.084 \pm 0.048$	$+0.060 \pm 0.068$

Table 10: The inclusive and charged asymmetries in all, early, and later data

12.4.1 Charge components

The signed asymmetries are shown for the two data periods in Table 10. Within the largish statistical uncertainty of the latter data, the $\mathrm{A}_{\mathrm{fb}}^{\mathrm{t\bar{t}}}$ charge components are self-consistent and stable across the datasets. In $\mathrm{A}_{\mathrm{fb}}^{\mathrm{lab}}$ we see that the A_{lab}^{-} for negative leptons is stable across the datasets, but that the latter data has a wrong sign in A_{lab}^{+}. This leads to the null in the total $\mathrm{A}_{\mathrm{fb}}^{\mathrm{lab}}$ for the latter data. Interestingly, opposing contributions in the early and later data combine to give an inclusive A_{lab}^{+} that is in very good agreement with the inclusive A_{lab}^{-} (it is possible to over-think these things).

12.4.2 Time series

In order to monitor the integrity of dataset for this analysis, we have calculated the asymmetries separately in each of the standard CDF data periods and studied the trends. The top row of Figure 27 shows the two asymmetries as measured separately in each of the data periods, p0-p25. For the time variable here we use the total number of b-tagged events in the sample. This plot shows trends in all tagging categories: pretags are in black, tags are in blue, double tags are in green, and anti-tags are in red. The double tags show large fluctuations consistent with the smaller sample. A very correlated downward fluctuation in all categories, driven by the pretag value, is seen in Period 23, and is probably a main ingredient in the differences between the two periods.

The cumulative asymmetries are shown in the bottom row of Figure 27. The $\mathrm{A}_{\mathrm{fb}}^{\mathrm{t\bar{t}}}$ asymmetry seems to be converging to values near +5% for all tag categories. The $\mathrm{A}_{\mathrm{fb}}^{\mathrm{lab}}$ trends show the negative asymmetry in the background dominated anti-tags (dominated by electroweak processes like $Wb\bar{b}$), the positive asymmetry in the tags (dominated by $\mathrm{t\bar{t}}$), and their net of almost zero asymmetry in the pre-tag sample. The trend in the double tags is probably the result of small statistics early in the Run, but could also be part of the general “double-tag problem” which will be discussed in Sec. 12.7, along with other observations about asymmetries across the b-tagging selections.

The cumulative significance of the asymmetries is shown in Figure 28. If the effect is real, we expect the significance to grow as $\sqrt{N}$. In fact,

$$\text{Significance} = \frac{A}{\sigma(A)} = \frac{A}{\sqrt{1-A^2}}\sqrt{N} \tag{46}$$

so that the scaling curve is normalized by the size of the asymmetry. Here we are most interested in the significance in the tagged sample. On each plot we show the best fit curve of the form $\sqrt{N}$ to the tagged data. The $\sqrt{N}$ curve is a good representation of the significance and we can use the normalization in fits Figure 28 as an alternate derivation of the ensemble asymmetry. The results are shown in Table 11. The fit means are in good agreement with the means in the data (the unphysical fit uncertainties are due to neglect of the uniform statistical errors on the significance).

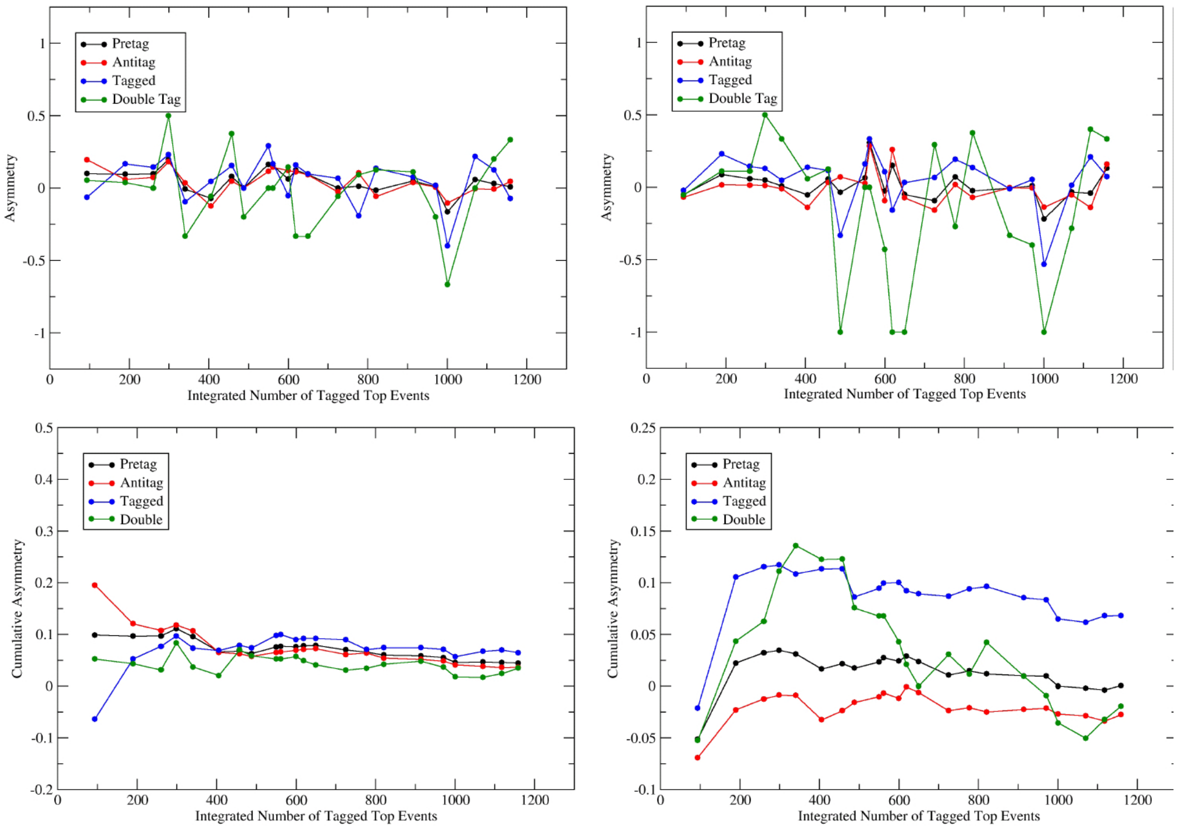

Figure 27: Top: Each point is the $A_{fb}^{t\bar{t}}$ (left) and A_{fb}^{lab} (right) for a CDF data period. Bottom: cumulative values for same variables as a function of data period.

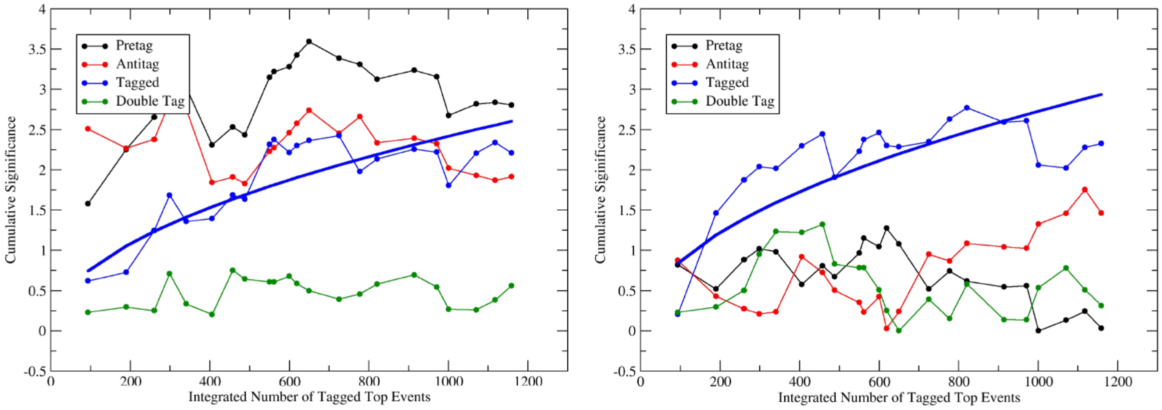

Figure 28: Significance of $A_{fb}^{t\bar{t}}$ (left) and A_{fb}^{lab} (right) for each data period.

	$A_{\mathrm{fb}}^{\mathrm{lab}}$	$A_{\mathrm{fb}}^{t\bar{t}}$
data	0.075 ± 0.030	0.070 ± 0.030
fit	0.085 ± 0.004	0.076 ± 0.004

Table 11: Inclusive asymmetries from the ensemble average and from the fit to the $\sqrt{N}$ hypothesis for the significance.

12.5 Triggers

The rows "CEM,CMUP,CMX" show the asymmetry measured separately for each one of our trigger lepton types. The fluctuations across the trigger types are large, but the values are all consistent within error.

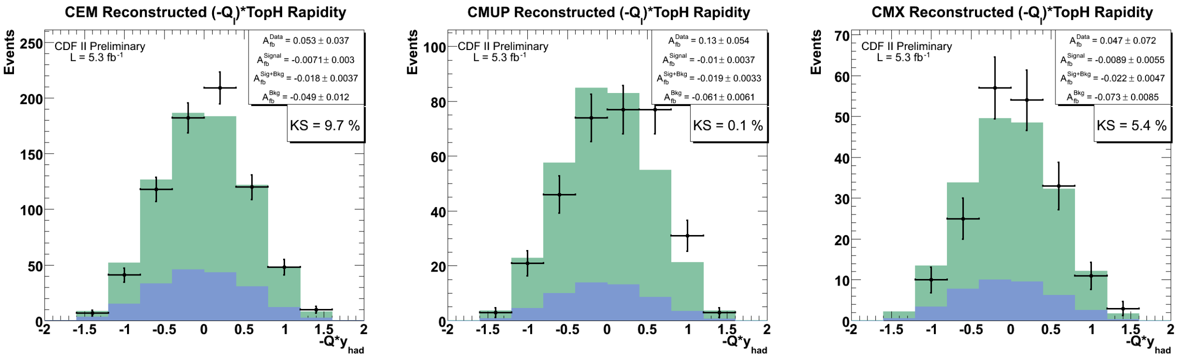

Figure 29: $-q{\cdot}y_{\mathrm{had}}$ split for CEM, CMUP, and CMX lepton events

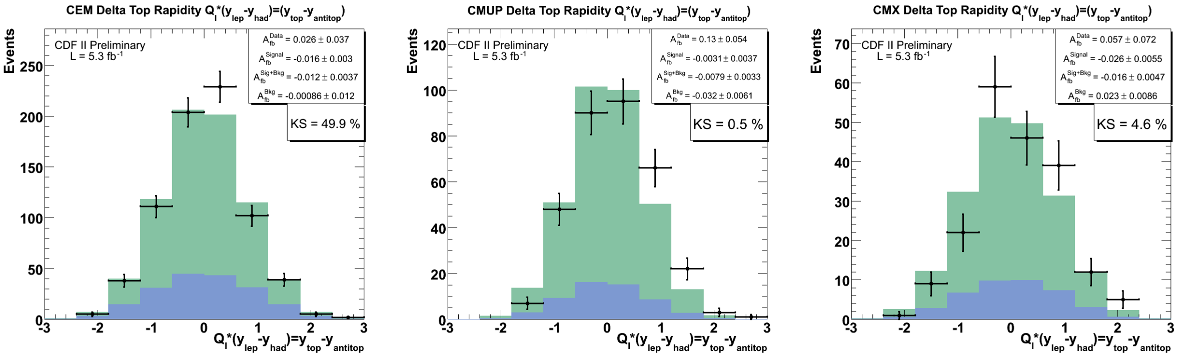

Figure 30: $q\Delta y$ split for CEM, CMUP, and CMX lepton events

12.6 Jet Multiplicity

Recall that the NLO QCD asymmetry is the sum of a positive asymmetry in exclusive 4-jet events and a negative asymmetry in events with ISR/FSR. In MCFM, restricting the sample to 4-jets almost doubles the asymmetry. Rows 11-12 show the two asymmetries in data samples partitioned according to the presence of an extra jet. The "4-jet" sample requires exactly 4 tight jets, has 939 events, and asymmetries of 0.0756 ± 0.0325 and 0.0650 ± 0.0326 for $-\mathrm{q}\cdot\mathrm{y}_{\mathrm{had}}$ and $\mathrm{q}\Delta\mathrm{y}$, respectively. The "5-jet" sample is actually 5-or-more tight jets, and has 321 events, and asymmetries of 0.0654 ± 0.0557 and 0.0343 ± 0.0558 for $-\mathrm{q}\cdot\mathrm{y}_{\mathrm{had}}$ and $\mathrm{q}\Delta\mathrm{y}$, respectively. The 4-jet vs. 5-jet asymmetries are marginally consistent within the large uncertainties. The jet multiplicity dependence is in the direction of the NLO effect, but weaker: in 4-jets the asymmetry increases but is not doubled, while 5-jets the asymmetry is reduced but negative. See Figures 31 and 32 for plots.

12.7 B-tagging

Rows 13-15 of Table 9 show the behavior of the asymmetries under different b-tagging selections. In row 15, we find that the asymmetries in the double-tags are very small. The asymmetry in the single-tags is then correspondingly larger than the full inclusive result. They single tags and double tags are barely statistically compatible, but the double tags still seem suggestively small. The double tags have very small backgrounds and, owing to the identification of both b-jets, very good accuracy in parton-jet assignment. The obvious hypothesis is that there is no real asymmetry, and some issue with backgrounds or b-jets in the reconstruction is creating a false asymmetry in the single tags. This is one of the biggest mysteries in these studies.

The M24U backgrounds are checked in the anti-tag sample as seen in Figure 33. The M24U model shapes and normalization, combined with the small $\mathrm{t}\bar{\mathrm{t}}$ admixture, provide a very good representation of the anti-tagged data. Given the good agreement in the antitags, it is impossible for the backgrounds to explain the asymmetries in the data [17].

Perhaps the single-tag result is somehow due to the treatment of single b-jets in the reconstruction. This is already somewhat disfavored by the charge symmetry argument in Section 12.2: why would the sign of a pull from a mis-identified b-jet depend on the lepton sign which is not used anywhere in the calculation? As an additional check we can look at the results when we use the lowest χ^2 reconstruction solution *without* the requirement that b-tags are associated with b-partons. The results in all tag selection categories, shown in Table 12, are very close to asymmetries found when b-tag consistency is required, suggesting that the asymmetry is not arising from any kind of bias associated with b-tag jets.

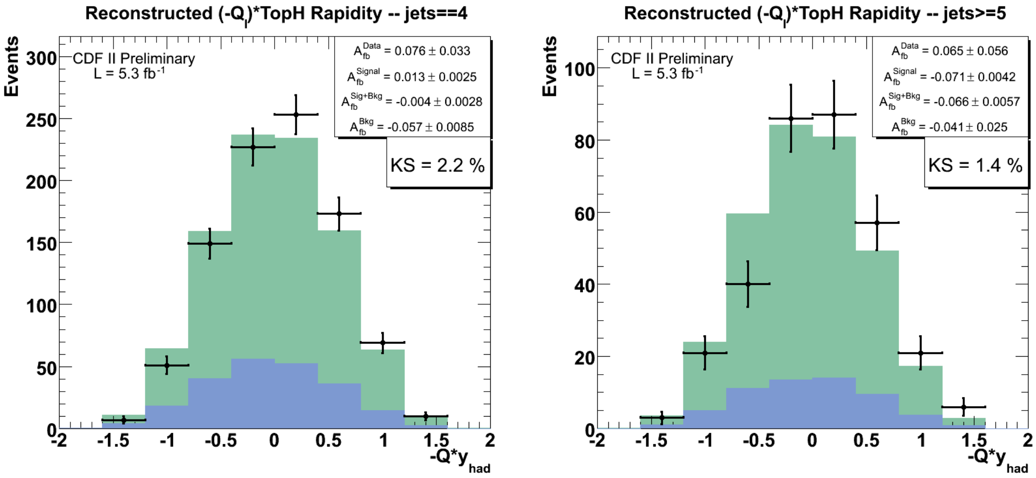

Figure 31: $-q{\cdot}y_{\rm had}$ split by nJets

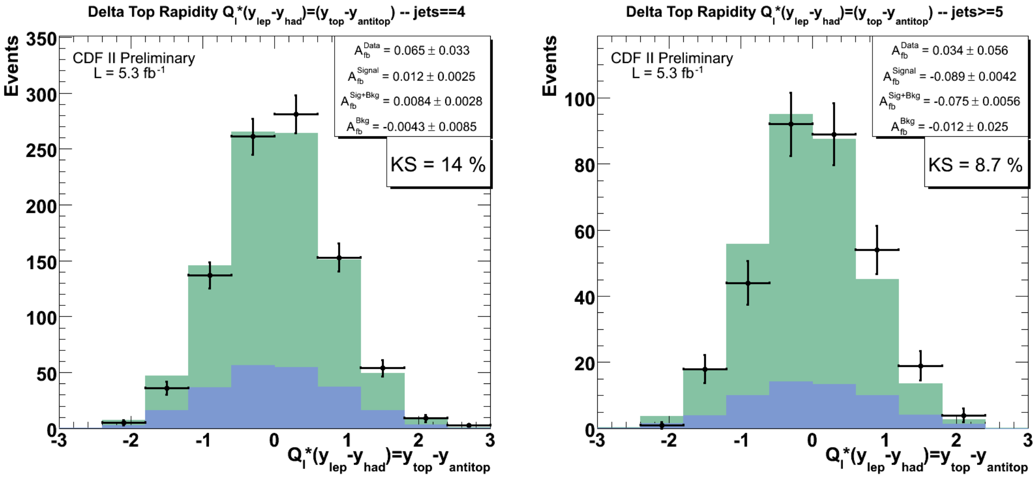

Figure 32: $q\Delta y$ split by nJets

The other special feature of double tagged events is an acceptance restriction: both b-jets must have $|eta| < 1.0$. It is conceivable that some aspect of the asymmetry disfavors 2 central b-jets, and it therefore cannot be seen in that selection. Our one cherry-picked physics model does not show this however: in the Madgraph coloron sample ctopo3, the double-tags there have very similar asymmetries to the single tags. The lack of asymmetry in the double tags remains mysterious.

Finally, we note the asymmetries in the pretag sample as shown in line 13 of Table 9. The pretag sample behaves as expected from the admixture of the backgrounds and b-tagged-$\mathrm{t\bar{t}}$ asymmetries. For *ad* the negative backgrounds combine with the positive $\mathrm{t\bar{t}}$ to give zero pre-tag asymmetry. For $\mathrm{A_{fb}^{t\bar{t}}}$, the pretags are the sum of the positive background asymmetry and the positive background asymmetry.

selection	$\mathrm{A_{fb}^{lab}}$	$\mathrm{A_{fb}^{tt}}$
pre-tag	????	????
inclusive tag	????	????
single tag	????	????
double tag	????	????

Table 12: The asymmetry in $\mathrm{A_{fb}^{lab}}$ and $\mathrm{A_{fb}^{t\bar{t}}}$ for various selections when the b-tag consistency is NOT used in the kinematic reconstruction

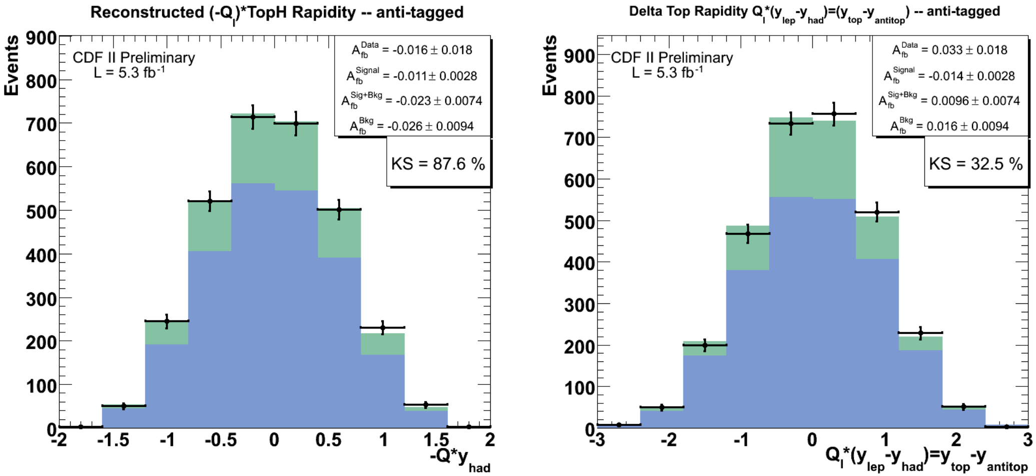

Figure 33: $-\mathrm{q}\cdot\mathrm{y_{had}}$ and $\mathrm{q\Delta y}$ distributions in the anti-tag sample.

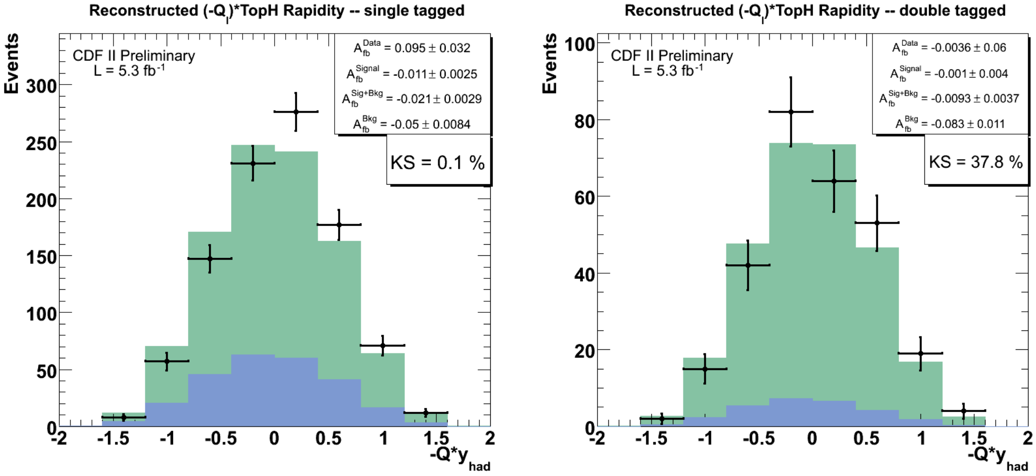

Figure 34: $-q{\cdot}y_{\mathrm{had}}$ split by number of tags (single / double)

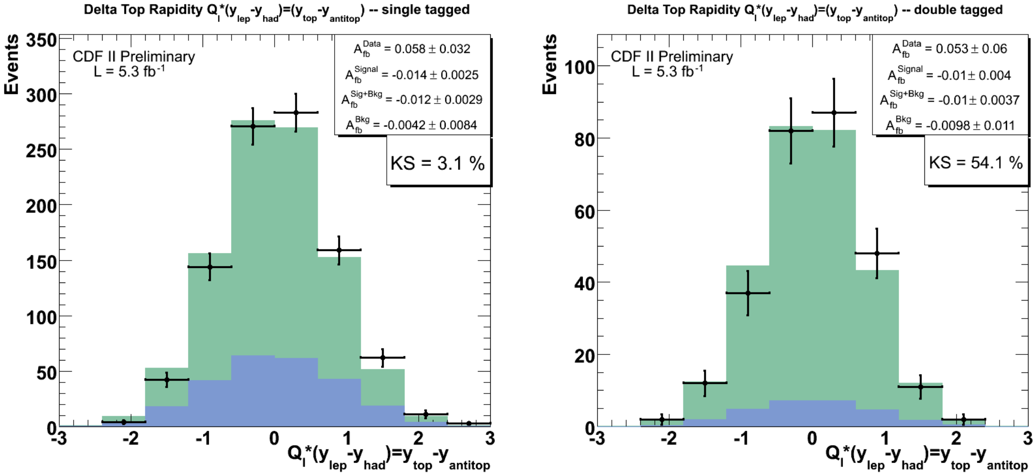

Figure 35: $q\Delta y$ split by number of tags (single / double)

13 Systematic Uncertainties

Because our correction method involves subtracting background shapes and unfolding the resulting distribution with smearing information from signal MC, our systematic uncertainties are easily organized into two categories: background uncertainties and top signal model uncertainties. (A third category is now added to account for the bin edge choice as discussed in Section 9.1).

The background systematic uncertainties are handled by subtracting different shapes and cross-sections (as described in Section 9) from the raw data and compare the final corrected (unfolded using ttop25) A_{fb} values. The signal model uncertainties are handled slightly differently – we use the background-subtracted data corrected using ttop25 and compare this "nominal" corrected A_{fb} value to a second unfolded value made using different MC signal sample to generate the unfold matrix. We use the top group conventions [19] for averaging values of the differences to obtain a final calculation for each systematic uncertainty. The calculated uncertainties for each component and each A_{fb} variable are summarized in Table 17. These components are added in quadrature to obtain a final systematic uncertainty for our measurement.

13.1 Background Uncertainties

The background subtraction influences the final corrected A_{fb} measurement through uncertainties in size and shape.

To account for the background size normalization, we use our reweighted signal MC (see Section 9) and add on the M24U background scaled by +25% and −25%. We then use our correction procedure to subtract off the normal expected background and unfold. By comparing our A_{fb} measurement of these modified samples with the corrected A_{fb} for the nominal shape (with unscaled M24U background) we find a percent change.

The overall shape of the background is determined by adding various MC samples (Table 4) weighted by the M24U numbers (Table 5). However, this background shape may be incorrect, so we wish to compare results with modified background shapes. It is difficult to define a $+\sigma$ and $-\sigma$ convention, so to account for uncertainty in background shape we choose single components of the method II background samples and reweight these shapes to have the same area as the M24U numbers predict for total background. We choose the largest 2 components of our backgrounds – QCD and Wbb – for this test. The A_{fb} for each of these samples can be found in Table 7. We choose the largest difference between corrected MC sample A_{fb} and the nominal corrected A_{fb} as our background shape uncertainty.

Tables 13 and 14 show the results for the background size and shape uncertainties:

	nominal A_{fb}	less	difference	more	difference	uncertainty
background size	0.1498	0.1357	0.0141	0.1662	-0.0164	0.0153
		QCD		Wbb		
background shape	0.1498	0.1336	0.0162	0.1620	-0.0122	0.0142

Table 13: $-q{\cdot}y_{had}$ background systematic uncertainties

	nominal A_{fb}	less	difference	more	difference	uncertainty
background size	0.1582	0.1482	0.0100	0.1698	-0.0116	0.0108
		QCD		Wbb		
background shape	0.1582	0.1337	0.0245	0.1728	-0.0146	0.0196

Table 14: $q\Delta y$ background systematic uncertainties

13.2 Signal Uncertainties

Top signal MC is generated with a set of assumptions which we describe below. Since the top model is used only in the unfold matrix when calculating the corrected A_{fb}, it is the unfold matrix that we modify by $+\sigma$ and $-\sigma$ for each systematic uncertainty category. Essentially we unfold the background-subtracted data with matrices generated from different MC samples that have the top parameters varied by $+\sigma$ and $-\sigma$, then we compare the resulting corrected A_{fb} value with the nominal A_{fb} value calculated from the ttop25 unfold. The average or largest of these differences (as per the top group conventions) is our systematic uncertainty for the varied parameter. Tables 15 and 16 show the numbers calculated for these signal uncertainties.

13.2.1 Initial and Final State Radiation (ISR/FSR)

Partons in a $t\bar{t}$ event may radiate gluons as seen in Figures 1a and 1b. These gluons may be energetic enough to produce jets, perhaps capable of being misidentified in event reconstruction as a decay quark. The branching ratios of such radiative effects is not well understood and is treated as a tunable parameter in top signal MC generation. We follow the top group's use of samples dtops1 and dtops1 to model $+1.0\sigma$ and -1.0σ shifts in the amount of radiation for both ISR and FSR.

13.2.2 Jet Energy Scale (JES)

Jet energies are determined by integrating over sections of the calorimeter hit by a jet using a jet clustering algorithm, however, this process is far from trivial and requires corrections. First, different calorimetry systems in the CDF detector have different response efficiencies for various particles. Calorimetry values often exhibit non-linear response to true particle energy. There are non-covered geometries in the detector, including spaces, or “cracks”, between calorimetry towers. Additionally there are inefficiencies and uncertainties associated with the integration clustering algorithms assigning calorimetry towers to jets. These effects all contribute overall adjustments to final jet energies, for which corrections are calculated. Here is a list of individual uncertainties in JES that we take into account

- Relative Correction
  Corrections due to η dependent calorimeter response.
- Underlying Event Correction
  Correcting for energy associated with the spectator partons in the event.
- Absolute Correction
  Corrects the jet energy measured in the calorimeter for any non-linearity and energy loss in the non-instrumented regions of the detector.
- Out-of-Cone Correction
  Corrects back to the particle-level energy by accounting for leakage of radiation outside of the jet clustering cone.
- Splash-Out Correction
  Uncertainty in the energy leakage beyond the out-of-cone scope.

Accounting for these effects incorrectly would cause different parts of the detector to have more or less response to jets, leading to an incorrect asymmetry measurement. We measure the uncertainty associated with these corrections by using the top signal MC sample ttop25 and vary these JES components by $+\sigma$ or $-\sigma$. We take the differences of the corrected $\mathrm{A_{fb}}$ values to calculate our JES systematic uncertainty.

13.2.3 Parton Distribution Function (PDF)

The momentum distribution of partons and gluons in Monte Carlo simulations is derived from empirically calculated functions, called “PDFs”. The momentum distribution of particles in hard scattering process determines the “energy” spectrum of the $\mathrm{t\bar{t}}$ system. To study the effect on our measurement to the uncertainty in the PDF, we compare 46 different sets of PDF: CTEQ6M, CTEQ5L, MRST72, MRST75, CTEQ6L, CTEQ6L1, CTEQ6M ± 20 (orthogonal pdf sets). The differences between the ± eigenvectors are compared and added in quadrature. We separately add the difference between MRST72 and CTEQ5L. The larger of these 2 sums, added in quadrature with the differences in the MRST72 and MRST75 sets, is taken as our PDF systematic uncertainty. This procedure can be found in detail on the top group’s systematic uncertainties web page [19].

13.2.4 Color Flow

We compare different "tunes" of color-flow parameters to each other and our nominal unfold. Sample ctopsd corresponds to the "Apro" tuning, while ctopse corresponds to "ACRpro".

13.2.5 Top MC Sample

Monte Carlo is expected to model the $t\bar{t}$ process from production to final state particles. This requires a number of effects to be simulated properly, such as top quark production, decay, and hadronization. Uncertainty in any number of these effects translates into measurement uncertainty. Fortunately, these simulations have been tested and refined over many measurements of various processes. Nonetheless, we assign an uncertainty to our measurement to account for differences between our model and the actual $t\bar{t}$ process. We calculate the systematic error by comparing our measurement for two entirely different MC simulations: Pythia and Herwig. The sample we use for Alpgen+Pythia is dtopa2, and for Alpgen+Herwig we use dtopa3. The absolute difference between these two corrected A_{fb} values is taken as our top shape systematic uncertainty.

	nominal A_{fb}	less	difference	more	difference	uncertainty
ISR/FSR	0.1498	0.1396	0.0102	0.1588	-0.0090	0.0096
JES	0.1498	0.1488	0.0010	0.1538	-0.0040	0.0025

Table 15: Selected $-q{\cdot}y_{had}$ signal systematic uncertainties

	nominal A_{fb}	less	difference	more	difference	uncertainty
ISR/FSR	0.1582	0.1562	0.0020	0.1554	0.0028	0.0014
JES	0.1582	0.1540	0.0042	0.1670	-0.0088	0.0065

Table 16: Selected $q\Delta y$ signal systematic uncertainties

13.3 Bin Edge Effects on Systematic Uncertainties

As discussed in Section 9.1, our choice of bin edges can effect the raw, background-subtracted, and fully-corrected values – first, through changing the bin event counts and second, through changing the unfold matrix. To account for these effects, we first find all of these A_{fb} numbers for our nominal bin edge choices (0.5 for $-q{\cdot}y_{had}$ and 1.0 for $q\Delta y$) and record them. We then vary the bin edges by ±0.1 and rerun our measurement. Using the same methods as above for the other systematics, we are able to find the effect of bin edge on each A_{fb} measurement.

13.4 Final Measurement with Systematic Uncertainty Calculation

By adding the various systematic uncertainties listed above (background size/shape, signal parameters, shape uncertainty) in quadrature, we arrive at these final values:

Systematic Uncertainty	$A_{fb}(-q \cdot y_{had})$	$A_{fb}(q\Delta y)$	$A_{fb}(\lvert\Delta y\rvert < 1.0)$	$A_{fb}(\lvert\Delta y\rvert > 1.0)$
background size	0.0153	0.0108	0.0019	0.0856
background shape	0.0142	0.0196	0.0078	0.2286
ISR/FSR	0.0096	0.0014	0.0037	0.0044
JES	0.0025	0.0065	0.0024	0.0034
PDF	??????	??????	??????	??????
Color Flow	0.0015	0.0042	0.0066	0.0071
MC Generator	0.0055	0.0052	0.0043	0.0326
Bin Edge	????	????	????	????
Total Uncertainty	0.0238	0.0242	0.0121	0.2464

Table 17: Summary of Systematic Uncertainties

14 Results and Conclusion

We have updated our previous measurement to include data through p27, corresponding to 5.3 fb^{-1}. The distribution $q\Delta y$ is now used to measure $A_{fb}^{t\bar{t}}$, in addition to the variable $-q{\cdot}y_{had}$ used to measure A_{fb}^{lab}. Finally, we have added a measurement of raw, background-subtracted, and corrected $A_{fb}(\Delta y)$.

Our final front-back asymmetry results are measured to be

	$A_{fb}(-q{\cdot}y_{had})$	$A_{fb}(q\Delta y)$	$A_{fb}(\|\Delta y\| < 1.0)$	$A_{fb}(\|\Delta y\| > 1.0)$
Raw	0.073 ± 0.028	0.057 ± 0.028	0.021 ± 0.031	0.208 ± 0.062
Raw-Bkg	0.110 ± 0.036	0.075 ± 0.036	0.029 ± 0.040	0.291 ± 0.090
Corrected	$0.150 \pm 0.050 \pm 0.024$	$0.158 \pm 0.072 \pm 0.024$	$0.026 \pm 0.104 \pm 0.012$	$0.611 \pm 0.210 \pm 0.246$

Table 18: Final A_{fb} Values for $-q{\cdot}y_{had}$, $q\Delta y$, and $A_{fb}(\Delta y)$

These values should be compared to the the small $p\bar{p}$ frame charge asymmetry expected in QCD at NLO, $A_{fb} = 0.050 \pm 0.015$ [6–9], and the corrected values for $A_{fb}(\Delta y)$ are to be compared with the MCFM model predictions of 0.039 ± 0.006 and 0.123 ± 0.018 for the inner and outer rapidities, respectively.

References

[1] G. L. Strycker *et al.*, "Measurement of the Forward-Backward Asymmetry in $\mathrm{t\bar{t}}$ Production in 3.2 fb^{-1} of Tevatron Data", CDF-9705, Mar. 2009

[2] Thomas A Schwarz, Robin Erbacher, Dante Amidei, "Measurement Of The Front Back Asymmetry In Top-Antitop Quark Pairs In 1.9 fb^{-1}", CDF-9078, Oct. 2007

[3] T. Aaltonen *et al.*, CDF Collaboration, "Forward-Backward Asymmetry in Top-Quark Production in $\mathrm{p\bar{p}}$ Collisions at $\sqrt{s}$=1.96 TeV", Phys. Rev. Lett. 101 (2008), 202001 (also as CDF-9295, June 2008)

[4] D. Hirschbühl *et al.*, "Measurement of the Charge Asymmetry in Top Pair Production using 1.9 fb^{-1}", CDF-9122, Dec. 2007

[5] V. M. Abazov *et al.*, D0 Collaboration, "Measurement of the Forward-Backward Charge Asymmetry in Top-Quark Pair Production", Phys. Rev. Lett. 100 (2008), 142002

[6] O. Antunano, J. H. Kuhn, and G. Rodrigo, Phys. Rev. D 77, 014003 (2008)

[7] M. T. Bowen, S. Ellis, and D. Rainwater, Phys. Rev. D 73, 014008 (2006)

[8] S. Dittmaier, P. Uwer, and S. Weinzierl, Phys. Rev. Lett. 98, 262002 (2007)

[9] L. G. Almeida, G. Sterman, and W. Vogelsang, Phys. Rev. D 78, 014008 (2008)

[10] Paola Ferrario and Germn Rodrigo, Phys. Rev. D 80, 051701(R) (2009), hep-ph/0906.5541

[11] J. M. Campbell, R. K. Ellis, Phys. Rev. D 62, 114012 (2000), hep-ph/0006304
`http://mcfm.fnal.gov/`

[12] A. Bridgeman, L. Cerrito *et al.*, "Study of Charge Asymmetry in W+jets", CDF-9323, May 2008

[13] Top Group Good Run List (GRL) web pages,
`http://www-cdf.fnal.gov/internal/physics/top/luminosity.shtml`
`http://www-cdf.fnal.gov/internal/physics/top/RunIITopProp/gen6Sum06/lumi_v25.html`

[14] J. Adelman *et al.*, "Method II For You", CDF-9185, May 2008
`http://www-cdf.fnal.gov/internal/physics/top/RunIITopProp/m2-4u/methodII.html`

[15] G. Strycker *et al.* "Data Validation for $\mathrm{A_{fb}}$ Analysis", talk at Top Meeting, April 22, 2010.
`www-cdf.fnal.gov/internal/WebTalks/Archive/1004/100422_top/02_Glenn_Strycker_1_afb_p0tp19_vs_p20tp25_presentation_2010-04-22_final.pdf`

[16] M. Tecchio, T. Schwarz *et al.*, "Dependence of the Forward-Backward Asymmetry in $\mathrm{t\bar{t}}$ Production on the $\mathrm{M_{t\bar{t}}}$ Invariant Mass", CDF-9813, June 2009

[17] A. Eppig *et al.*, “Measurement of $dA_{FB}/d\mathrm{M}_{\mathrm{t\bar{t}}}$ in $\mathrm{t\bar{t}}$ Production”, talk at Top Meeting, April 1, 2010,
`http://www-cdf.fnal.gov/internal/WebTalks/Archive/1004/100401_top/05_100401_top_Andrew_Eppig_1_eppig_2010-04-01UpdatedAFBResults.pdf`

[18] Y.C. Chen *et al.* “Final Report of the B-Tag Task Force”, CDF-10069, Feb. 2010

[19] Top Group Systematic Uncertainties web page,
`http://www-cdf.fnal.gov/internal/physics/top/run2mass/systematics_links.html`,
`http://www-cdf.fnal.gov/internal/physics/top/run2mass/systematics_08_add.html`

[20] `http://www-cdf.fnal.gov/internal/physics/top/RunIITopProp/tools/fitter.html`

[21] Erik Brubaker *et al.*, “Updated Measurement of the Top Quark Mass in the Lepton+Jets Channel”, CDF-6845, May 2004

[22] T. Affolder *et al.*, Phys Rev D 64, 032002 (2001)

15 Appendix: Event Selection Details

The $p\bar{p}$ collisions at the Tevatron produce a broad range of final states. This analysis is performed with $t\bar{t}$ events in the lepton plus jets channel. The lepton plus jets channel is characterized by a high P_t lepton, a large amount of missing energy, and at least four jets from two b-quarks and two quarks from the hadronic decay of a W-boson. These are relatively rare events, and their isolation from the general collision data requires a detailed selection.

The event selection is performed through several stages. The first stage is performed in real time, as the online trigger selects collision events for readout. Since leptons have such distinct signals, our primary trigger selections are based upon the detection of a high momentum electron in the CEM, or a muon in the CMUP or CMX. The trigger requirements are described in the electron and muon identification sections below. Events passing the online trigger requirements are written to disk in separate "streams" for each trigger. The streams are processed offline to apply calibration constants and fully reconstruct higher level signals such as tracks and showers from low level detector information. Tracks and showers are then combined into "physics objects" such as muon, electron, and jet candidates, which are examined for quality and form the essential part of the $t\bar{t}$ selection.

We first describe the separate selections for electron, muons, jets, and missing energy and then how these are combined to select $t\bar{t}$.

16 Appendix: Electron Identification

A high momentum electron detected at the trigger level is used as a source for a possible $t\bar{t}$ lepton plus jets event. Electrons are identified as a single isolated track pointing to an isolated deposit of energy in a single electromagnetic calorimeter tower in the CEM ($|\eta| < 1.0$).

The trigger level requirements are listed first, followed by offline requirements for electron identification.

16.1 Triggers

16.1.1 Level 1

- A cluster of energy in the central EM calorimeters with $E_t \geq 8.0$ GeV.
- The ratio of energy deposited in the HAD compartment to EM compartment in the calorimeter tower is small [$(\mathrm{HAD}/\mathrm{EM}) \leq 0.125$] as expected for an electromagnetic shower.

- One or more tracks in the COT with $P_t \geq 8$ GeV.

16.1.2 Level 2

- A cluster of energy in the central EM calorimeters with $E_t \geq 16.0$ GeV, and (HAD/EM) ≤ 0.125.
- A track in the COT at level 1 must point to the cluster.
- Matching track $P_t \geq 8$ GeV.

16.1.3 Level 3

- A cluster of energy in the central EM calorimeters with $E_t \geq 18.0$ GeV, and (HAD/EM) ≤ 0.125.
- Matching track $P_t \geq 8$ GeV.
- $L_{shr} < 0.4$
  The lateral shower profile compares the small sharing of the shower energy across neighboring towers with expectations based on test beam data. The L_{shr} cut is on the χ^2 of the comparison.

16.2 Offline Selection

Offline selection is applied to events that have passed through the trigger levels. The cuts can be more stringent because the offline information is more detailed. Electrons that pass the offline selection criteria are referred to as “tight” electrons. The offline selection criteria for electrons is detailed below.

- $E_t \geq 20$ GeV
  Electrons in $t\bar{t}$ events are expected to have high energy.
- $P_t \geq 10$ GeV
  For an ideal electron $P_t = E_t$.
- $P_t \geq 50$ GeV (if $E_t > 100$ GeV)
  This cut filters out high momentum hadrons that fake electrons.
- $E_{HAD}/E_{EM} < 0.055 + 0.00045 \cdot E$
  Since the electromagnetic shower of an electron is mostly contained in the electromagnetic compartment, we can reduce the number of jets misidentified as an electron by requiring that the ratio of hadronic energy to electromagnetic energy is small.

  The requirement is linearly scaled with energy because very high energy electrons will deposit a larger fraction of energy into the hadronic compartment.

- $E/p < 2.0$ (if $E_t < 100$ GeV)
  The energy an electron deposits in the calorimeter should be approximately be the same as the momentum of the matching track.

- # COT Axial Segments ≥ 3 and # COT Stereo Segments ≥ 2
  This is a quality cut on the electron track found in the COT.

- $Track|z_0| < 60$ cm
  z_0 is the z intercept of the electron track. This is done to guarantee the track originates from optimal regions in the COT.

- $-3.0cm < Q \cdot \Delta x < 1.5$ cm
  Δx is the distance in the x-coordinate between the COT track position extrapolated to the CES and the actual hits in the CES chamber. Matching tracks between CES and the COT is charge dependent and, therefore, this cut is different depending on the charge of the electron track.

- $|\Delta z| < 3.0$ cm
  Δz is the distance in the z-coordinate between the COT track position extrapolated to the CES and the actual hits in the CES chamber. A minimum window is applied to this distance to match the COT track to the CES hits.

- $\chi^2_{strip} < 10$
  A χ^2 test is performed between the profile of hits in the CES and the expected profile of electrons.

- $L_{shr} < 0.2$
  A tighter requirement on the lateral shower profile.

- $Isolation < 0.1$
  The energy deposited in a calorimeter by an electron is very collimated. An "isolation" requirement examines the energy nearby the electron. Jets that fake electrons are filtered out by requiring that energy deposited in a cone around the electron is small. This is quantified by the variable I_l.

  $$I_l = \frac{\sum E_t^{\Delta R<0.4} - E_t^{electron}}{E_t^{electron}} \tag{47}$$

  The ratio of energy in a cone $\Delta R = \sqrt{(\Delta\phi)^2 + (\Delta\eta)^2}$ around the electron to the energy of the electron must be smaller then 0.1.

- No Conversions
  High energy photons interacting with material in the detector can convert into electron-positron pairs. Electrons from conversions are backgrounds to our electron selection. High energy conversions appear as oppositely charged tracks traveling in the same direction and having a pair mass of zero. An electron identified with a conversion partner is rejected.

17 Appendix: Muon Identification

A high momentum muon detected at the trigger level is used as a source for a possible $t\bar{t}$ lepton plus jets event. Muons are identified as tracks in the COT matched to stubs in the muon chambers.

17.1 CMUP Triggers

17.1.1 Level 1

- A muon stub in the CMU detector with $P_t \geq 6.0$ GeV.
- Track with $P_t \geq 4$ GeV in the COT extrapolates to the muon stub.
- An additional stub required in the CMP detector.

17.1.2 Level 2

- COT track with $P_t \geq 8$ GeV

17.1.3 Level 3

- Tracks in the COT are extrapolated to stubs in both the inner CMU and outer CMP
- COT track with $P_t \geq 18$ GeV

17.2 CMX Triggers

17.2.1 Level 1

- A muon stub in the CMX detector with $P_t \geq 6.0$ GeV
- $P_t \geq 8$ GeV COT track with hits in at least four superlayers

17.2.2 Level 2

- No Level 2 Trigger Selections

17.2.3 Level 3

- COT track extrapolates to CMX stub
- COT Track with $P_t \geq 18$ GeV

17.3 Offline Selection

- $P_t \geq 20$ GeV
  Muons originating from W-bosons are expected to have large momentum.

- E_{EM} <Maximum of 2.0 GeV or $2.0 + 0.0115 \cdot (p - 100.0)$ GeV
  Muons are minimum ionizing particles and therefore should leave little energy in the electromagnetic calorimeters. A linear correction term is added because the deposited energy increases slightly with the momentum of the muon.

- E_{HAD} <Maximum of 6.0 GeV or $6.0 + 0.0115 \cdot (p - 100.0)$ GeV
  Muons should leave little energy in the hadronic calorimeters as well, though slightly more energy then the EM calorimeters because of the increased amount of material.

- $\Delta x_{CMU} < 3.0$ cm
  For an event with CMU hits, the extrapolated COT track must be within a small window of the hits in the CMU chamber.

- $\Delta x_{CMP} < 5.0$ cm
  For an event with CMP hits, the extrapolated COT track must be within a small window of the hits in the CMP chamber.

- $\Delta x_{CMX} < 6.0$ cm
  For an event with CMX hits, the extrapolated COT track must be within a small window of the hits in the CMX chamber.

- $|d_0| < 0.02$ cm with hits in silicon
  The impact parameter, d_0, is the distance of closest approach from the track to the z-axis. This rejects cosmic rays and mis-reconstructed tracks that do not apparently originate from the primary vertex.

- $|d_0| < 0.2$ cm without any hits in silicon
  This requirement is made less stringent if the track cannot be matched to a corresponding one in silicon or if the silicon detector is not in operation.

- $Track|z_0| < 60$ cm
  z_0 is the z intercept of the muon track. This is done to guarantee the track originates from optimal regions in the COT.

- # COT Axial Segments ≥ 3 and # COT Stereo Segments ≥ 2
  This is a quality cut on the muon track found in the COT.

- COT exit radius < 140 cm (CMX Only)
  This is done for muons detected in the CMX chambers only. It imposes a requirement that the track from the muon left in the COT had passed through a minimum number of COT layers before matching to the CMX chamber.

- Isolation < 0.1
  As in the case of the electron, the "isolation" requirement examines the energy nearby the muon. Jets with muon "punchthrough" or decays in flight are rejected by requiring that energy deposited in the calorimeters in a cone around the muon is small. The isolation of the muon is the ratio of the energy in a cone around the muon to the momentum of the muon.

$$I_l = \frac{\sum E_t^{\Delta R<0.4}}{P_t^{muon}} \tag{48}$$

- Cosmic Veto
  Cosmic rays detected by CDF are characterized by two back-to-back tracks separated with a $\Delta\phi$ very close to 180 degrees and timing of the hits such that the track appears to be going "backward in time" across half of the COT diameter. These characteristics can be flagged and such muons are rejected.

18 Appendix: Jet Identification And Corrections

Partons produced in the p$\bar{\text{p}}$ collision will hadronize into a shower of neutral and charged particles. This shower of particles is referred to as a jet. The signature of a jet is multiple tracks from the charged particles and a large amount of energy deposited in both hadronic and electromagnetic calorimeters. Jets are identified as isolated deposits of energy in the calorimeters. The energy and direction of the jets are found by associating energies deposited in neighboring calorimeter towers into a single calorimeter "cluster".

The clustering is performed around any tower with $E_t > 3.0$ GeV. For any such tower, the algorithm begins by adding the energy of all towers within a cone of $\Delta R < 0.4$ of the highest energy tower in the group. The center of the cluster is calculated as the energy weighted centroid of the tower coordinates. A reclustering is then performed around this new center and then the process repeated until it converges. The energy of the jet is the sum of the energy in a cone $\Delta R < 0.4$ around the center. Once a tower is included inside a clustered jet, it is no longer allowed to be included in the clustering of any other jet.

Several corrections to calculated jet energies account for known issues with the calorimeter response and other sources of deposited energy. Corrections are applied to jets in "levels", each of which is described below.

- Level 1 (η Dependence): Applied to the raw energy deposited in the calorimeter to correct for differences in calorimeter response as a function of η.

- Level 2 and 3 are no longer in use.

- Level 4 (Multiple Interactions): Energy from an overlapping p$\bar{\text{p}}$ interaction during the same bunch crossing will be detected inside jet clusters, increasing the energy of the measured jet. This correction subtracts that contribution on average.
- Level 5 (Absolute): Corrects the jet energy measured in the calorimeter for any non-linearity and energy loss in the un-instrumented regions of each calorimeter.
- Level 6 (Underlying Event): The underlying event is defined as the energy associated with the spectator partons in a hard collision event. These are the partons that do not contribute to the hard scattering, but whose peripheral interaction produces low energy particles in the event. Depending on the details of the particular analysis, this energy needs to be subtracted from the particle-level jet energy.
- Level 7 (Out Of Cone): The choice of $\Delta R < 0.4$ for clustering is arbitrary. Some of the jet energy will be outside of this cone. This correction uses Monte Carlo models of jets to correct for the out-of-cone energy, taking the jet energy back to the parent parton energy.

For this analysis, all jets are corrected to level 4 for selection purposes and to level 5 for all other purposes.

For the purpose of t$\bar{\text{t}}$ identification, jets are grouped into two kinds: "tight" and "loose". Any jet with level 4 corrected $E_t \geq 15.0$ GeV and $|\eta| < 2.0$ is a tight jet, and any jet with level 4 corrected $E_t \geq 8.0$ GeV and $|\eta| < 2.0$ is considered a loose jet. Note that tight jets are a subset of loose jets.

19 Appendix: Missing Energy

At the Tevatron, the protons and antiprotons in the beam have zero transverse momentum and therefore, the 4-vector sum of the transverse energy in the detector should be zero. In a lepton plus jets event, a large amount of momentum is carried away by the undetected neutrino. This produces a transverse momentum imbalance in the detector, which is called missing energy ($\not{E}_T$), and it is closely related to the neutrino transverse momentum.

The calculation of $\not{E}_T$ begins as the negative of the vector sum of the raw (uncorrected) transverse energy in the calorimeter towers broken into x,y components.

$$\not{E}_{T,x}^{raw} = -\sum_{towers} E^{tower} \cdot Cos(\phi_{tower}) \tag{49}$$

$$\not{E}_{T,y}^{raw} = -\sum_{towers} E^{tower} \cdot Sin(\phi_{tower}) \tag{50}$$

Since the neutrino causes the imbalance, it will be opposite the apparent total momentum, thus the minus sign in the above equations.

In the case that the event contains a muon, which leaves minimal energy in the calorimeter, the sum is corrected by subtracting the associated calorimeter energy and adding the muon track momentum (for events without a muon, this step is skipped).

$$\not{E}_{T,x}^{muon-corr} = \not{E}_{T,x}^{raw} - P_t^{muon} \cdot Cos(\phi_{muon}) \tag{51}$$

$$\not{E}_{T,y}^{muon-corr} = \not{E}_{T,y}^{raw} - P_t^{muon} \cdot Sin(\phi_{muon}) \tag{52}$$

Finally the effect of the jet corrections is incorporated by removing the raw jets and adding the corrected jets to the sum.

$$\not{E}_{T,x}^{L4-corr} = \not{E}_{T,x}^{muon-corr} + \sum_{loose\,jets} E_{raw}^{jet} \cdot Cos(\phi_{jet}) - \sum_{loose\,jets} E_{L4Corrected}^{jet} \cdot Cos(\phi_{jet}) \tag{53}$$

$$\not{E}_{T,y}^{L4-corr} = \not{E}_{T,y}^{muon-corr} + \sum_{loose\,jets} E_{raw}^{jet} \cdot Sin(\phi_{jet}) - \sum_{loose\,jets} E_{L4Corrected}^{jet} \cdot Sin(\phi_{jet}) \tag{54}$$

The final corrected $\not{E}_T$ vector has magnitude equal to the quadrature sum of the x-y components and angular direction calculated from the x-y components.

$$\not{E}_T = \sqrt{(\not{E}_{T,x}^{L4-corr})^2 + (\not{E}_{T,y}^{L4-corr})^2} \tag{55}$$

$$\phi_{\not{E}_T} = Tan^{-1}(\not{E}_{T,y}^{L4-corr} / \not{E}_{T,x}^{L4-corr}) \tag{56}$$

20 Appendix: Secondary Vertex b-Tagging

Top quarks decay to Wb, but most background processes to $t\bar{t}$ do not contain heavy flavor quarks in the final state. The bottom quark is long lived, and the typical b from top decay, with $p = 65$ GeV, travels a distance $\gamma\beta c\tau = 500$ μm. This can be observed in the silicon detector as tracks within a jet forming a secondary vertex that is displaced from the primary vertex. An algorithm, called SecVtx, identifies events displaced secondary vertices in jets, and these vertices are used in selection to reduce background processes [22]. A jet identified with a secondary vertex by SecVtx is said to be “tagged”.

Tagging is performed for each jet in an event by selecting quality tracks inside the jet and searching for vertices formed by those tracks. The quality of a track is determined by the number of hits in silicon tracking, the χ^2 of the track, and the momentum of the track. Good tracks with a large impact parameter are tested to see if they form a common vertex. For each vertex found, the length of the vector pointing from the primary vertex to the secondary vertex in the $r - \phi$ plane (L_{xy}), is calculated along with its error ($\sigma_{L_{xy}}$). If $L_{xy}/\sigma_{L_{xy}} > 3.0$ the jet is “tagged”.

21 Appendix: Dilepton Veto

To separate the $t\bar{t}$ lepton plus jets channel from the dilepton channel, any event with a second tight lepton is removed.

22 Appendix: Z veto

Events are removed if a tight lepton and a second object form an invariant mass consistent with a Z-boson ($76 < M_{ll} < 106$ GeV). If the tight lepton is an electron, the second object must be an isolated electromagnetic object, a re-clustered jet with 95% of energy deposited in the electromagnetic calorimeter, or an opposite-signed isolated track. If the tight lepton is a muon, the second object must be an isolated muon or an opposite-signed isolated track.

23 Appendix: Primary Vertex Reconstruction

The origin of the event is the primary vertex. The z-position of the primary vertex is used to cluster jets and to ensure that leptons and jets belong to the same interaction. The z-position of the primary vertex is estimated by the error weighted sum of the z-intercept of all tracks within a common point of origin.

$$z_{PrimVertex} = \frac{\sum_{tracks} z_0^{track}/\Delta^2_{track}}{\sum 1/\Delta^2_{track}} \tag{57}$$

To ensure the lepton originates from the primary vertex events are rejected if the lepton z-intercept is not within 5 cm of the primary vertex z-position. This reduces the number of events in the sample where jets and the lepton are part of different interactions.

24 Appendix: Full Validation Plots for Observables

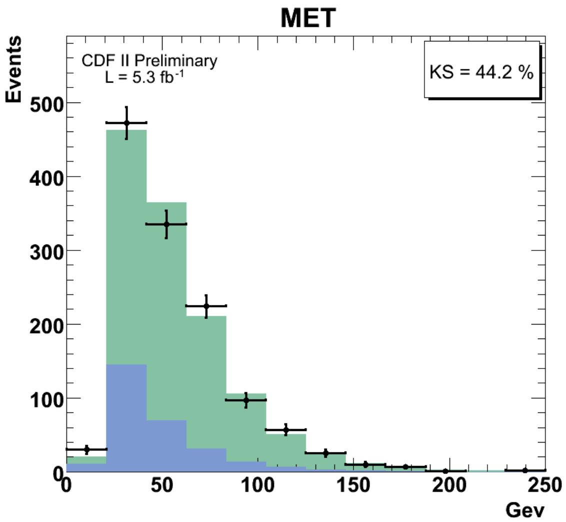

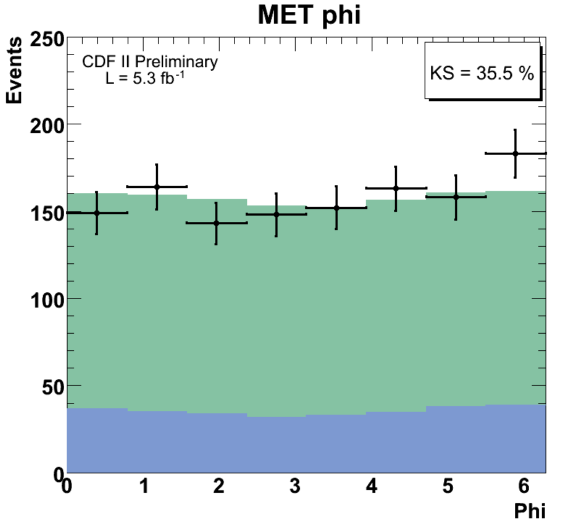

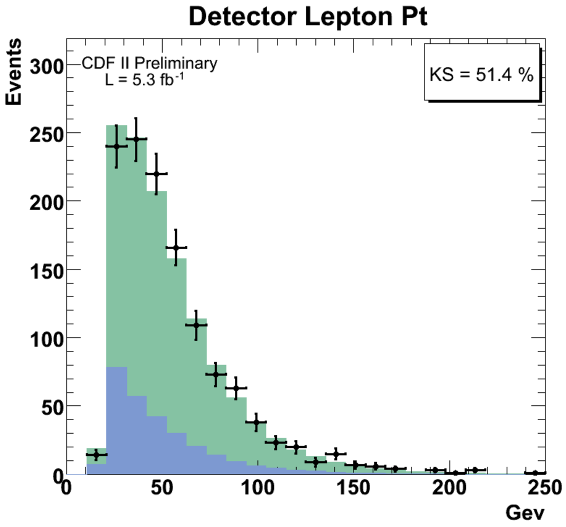

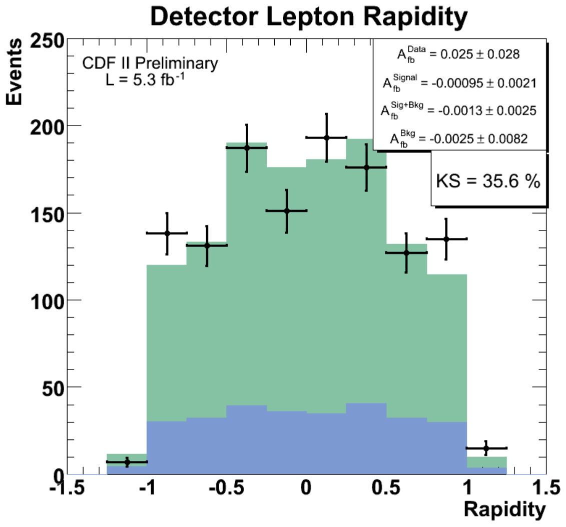

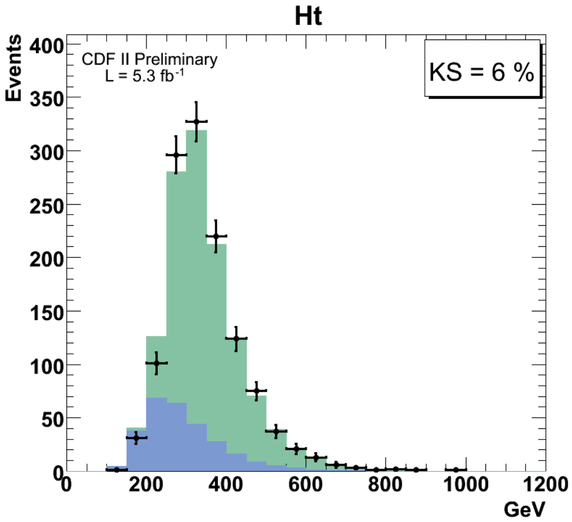
Ht
Events
CDF II Preliminary
L = 5.3 fb-1
KS = 6 %
0
50
100
150
200
250
300
350
400
0
200
400
600
800
1000
1200
GeV

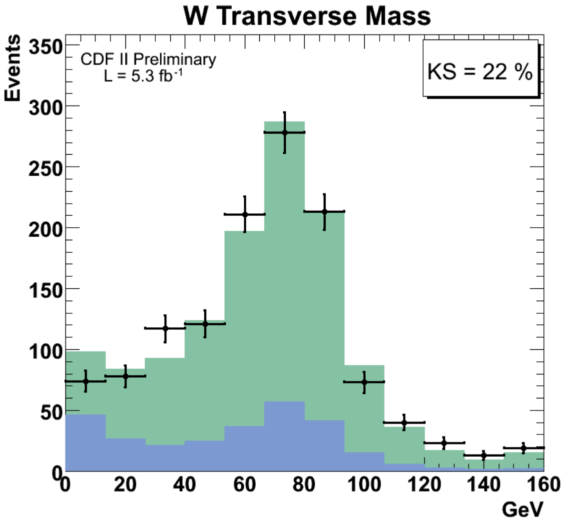
W Transverse Mass
Events
CDF II Preliminary
L = 5.3 fb-1
KS = 22 %
0
50
100
150
200
250
300
350
0
20
40
60
80
100
120
140
160
GeV

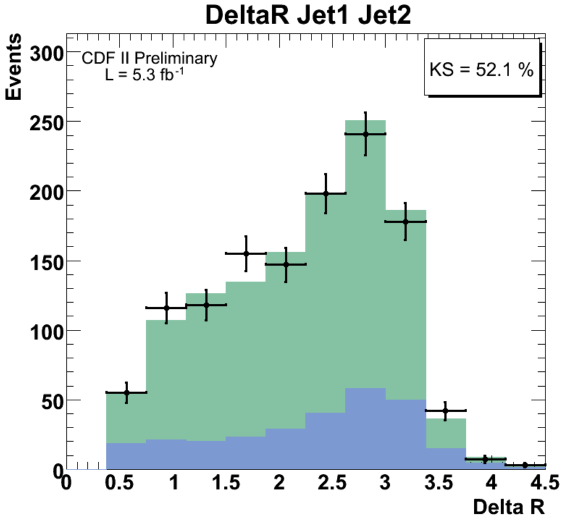
DeltaR Jet1 Jet2
Events
CDF II Preliminary
L = 5.3 fb-1
KS = 52.1 %
0
50
100
150
200
250
300
0
0.5
1
1.5
2
2.5
3
3.5
4
4.5
Delta R

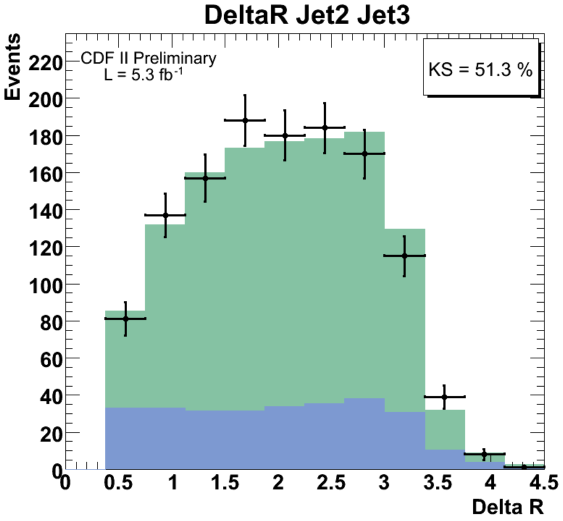
DeltaR Jet2 Jet3
Events
CDF II Preliminary
L = 5.3 fb-1
KS = 51.3 %
0
20
40
60
80
100
120
140
160
180
200
220
0
0.5
1
1.5
2
2.5
3
3.5
4
4.5
Delta R

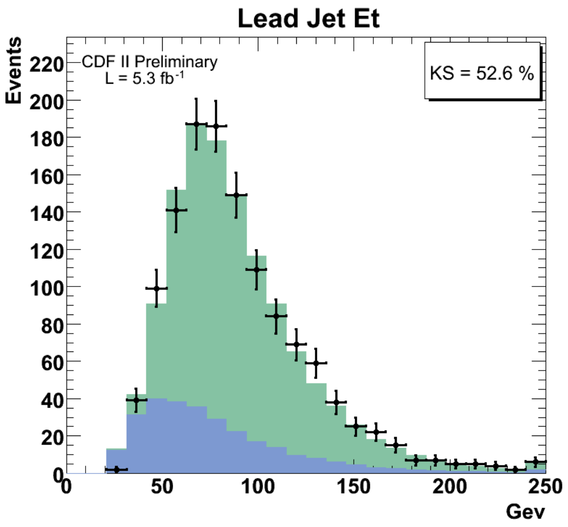
Lead Jet Et
CDF II Preliminary
L = 5.3 fb^{-1}
KS = 52.6 %
Events
0
20
40
60
80
100
120
140
160
180
200
220
0
50
100
150
200
250
Gev

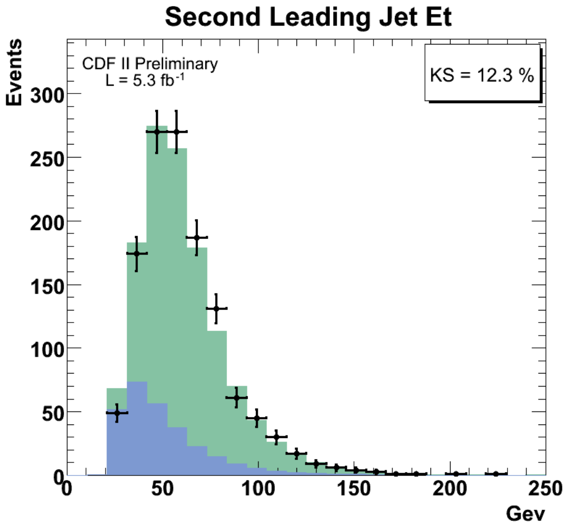
Second Leading Jet Et
CDF II Preliminary
L = 5.3 fb^{-1}
KS = 12.3 %
Events
0
50
100
150
200
250
300
0
50
100
150
200
250
Gev

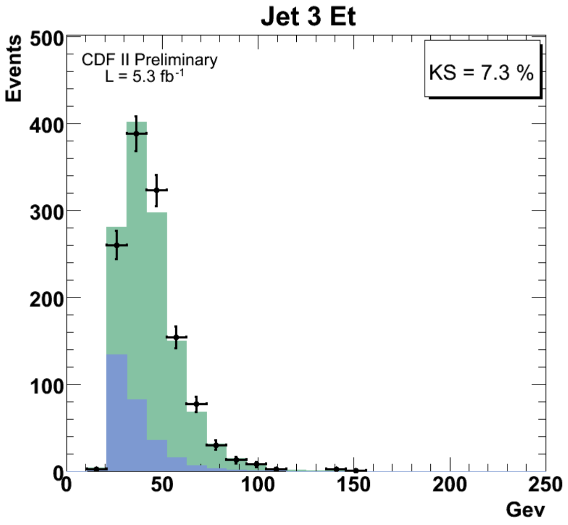
Jet 3 Et
CDF II Preliminary
L = 5.3 fb^{-1}
KS = 7.3 %
Events
0
100
200
300
400
500
0
50
100
150
200
250
Gev

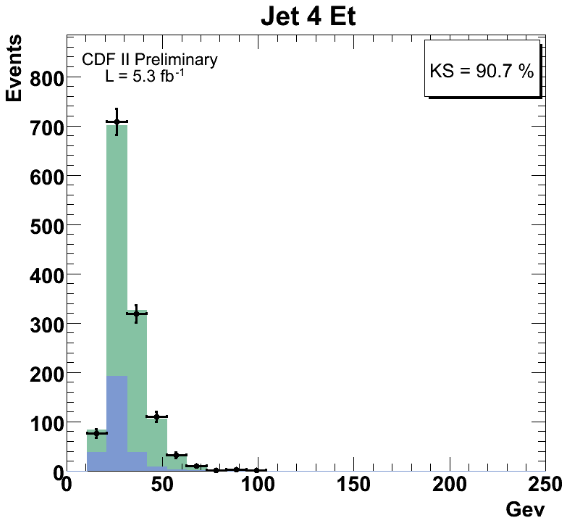
Jet 4 Et
CDF II Preliminary
L = 5.3 fb^{-1}
KS = 90.7 %
Events
0
100
200
300
400
500
600
700
800
0
50
100
150
200
250
Gev

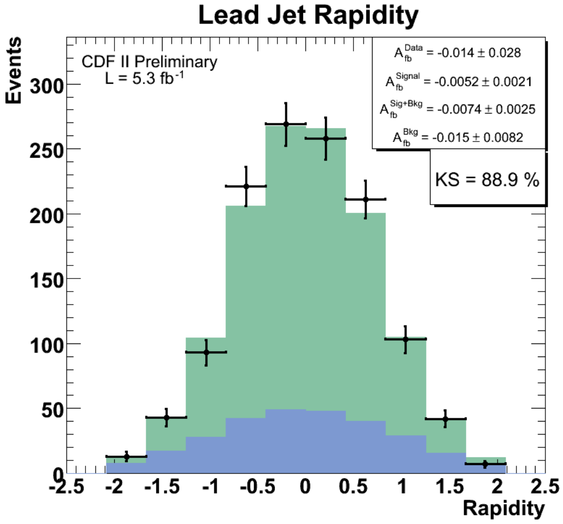
Lead Jet Rapidity
CDF II Preliminary
L = 5.3 fb^{-1}
A_{fb}^{Data} = -0.014 ± 0.028
A_{fb}^{Signal} = -0.0052 ± 0.0021
$A_{fb}^{Sig+Bkg}$ = -0.0074 ± 0.0025
A_{fb}^{Bkg} = -0.015 ± 0.0082
KS = 88.9 %
Events
0
50
100
150
200
250
300
-2.5
-2
-1.5
-1
-0.5
0
0.5
1
1.5
2
2.5
Rapidity

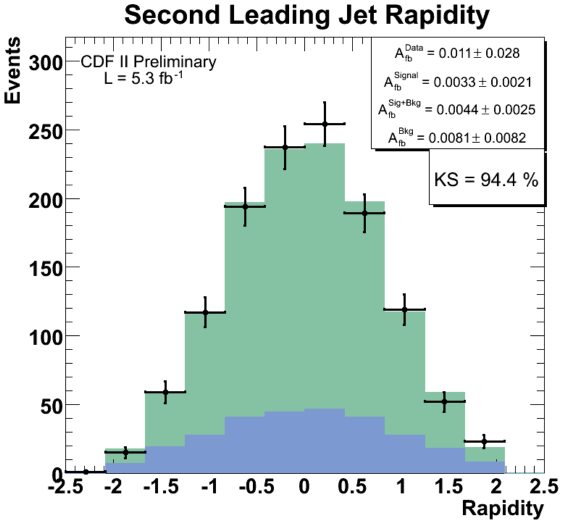
Second Leading Jet Rapidity
CDF II Preliminary
L = 5.3 fb^{-1}
A_{fb}^{Data} = 0.011 ± 0.028
A_{fb}^{Signal} = 0.0033 ± 0.0021
$A_{fb}^{Sig+Bkg}$ = 0.0044 ± 0.0025
A_{fb}^{Bkg} = 0.0081 ± 0.0082
KS = 94.4 %
Events
0
50
100
150
200
250
300
-2.5
-2
-1.5
-1
-0.5
0
0.5
1
1.5
2
2.5
Rapidity

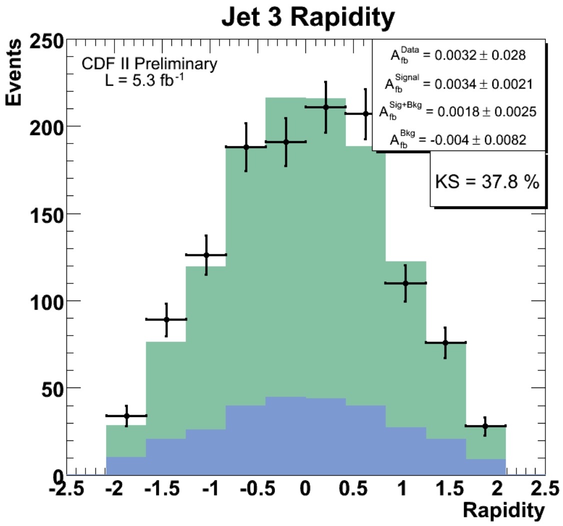
Jet 3 Rapidity
CDF II Preliminary
L = 5.3 fb^{-1}
A_{fb}^{Data} = 0.0032 ± 0.028
A_{fb}^{Signal} = 0.0034 ± 0.0021
$A_{fb}^{Sig+Bkg}$ = 0.0018 ± 0.0025
A_{fb}^{Bkg} = -0.004 ± 0.0082
KS = 37.8 %
Events
0
50
100
150
200
250
-2.5
-2
-1.5
-1
-0.5
0
0.5
1
1.5
2
2.5
Rapidity

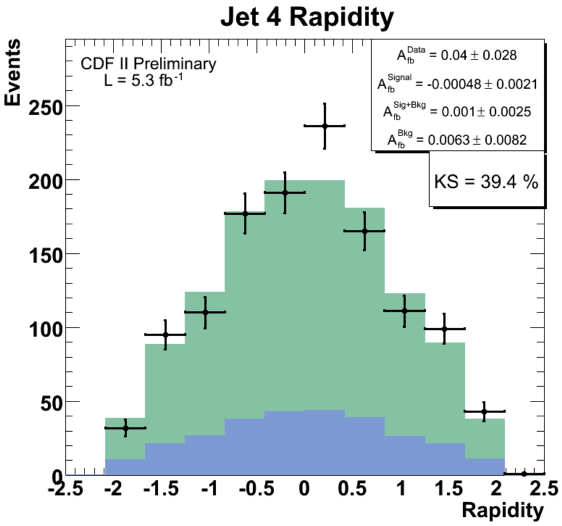
Jet 4 Rapidity
CDF II Preliminary
L = 5.3 fb^{-1}
A_{fb}^{Data} = 0.04 ± 0.028
A_{fb}^{Signal} = -0.00048 ± 0.0021
$A_{fb}^{Sig+Bkg}$ = 0.001 ± 0.0025
A_{fb}^{Bkg} = 0.0063 ± 0.0082
KS = 39.4 %
Events
0
50
100
150
200
250
-2.5
-2
-1.5
-1
-0.5
0
0.5
1
1.5
2
2.5
Rapidity

25 Appendix: Full Validation Plots for Reconstructed Event Variables

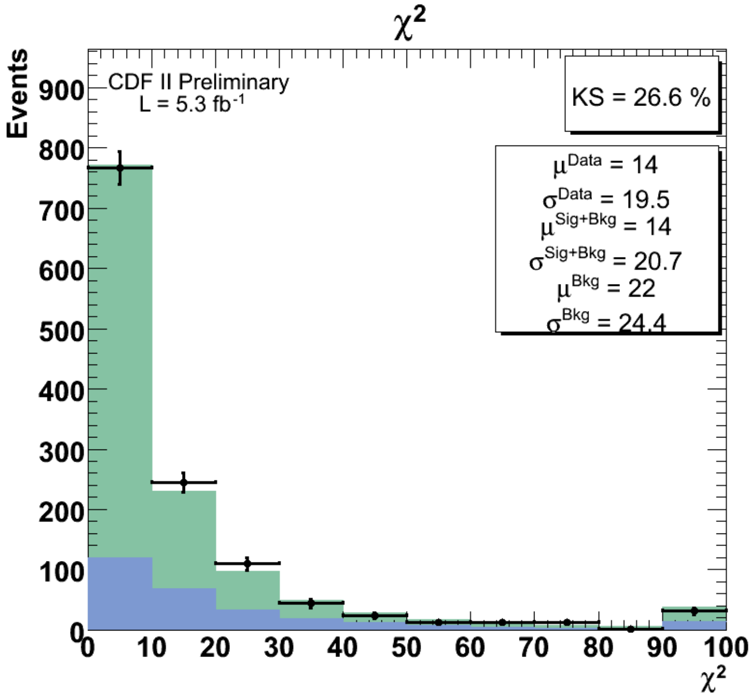

Figure 36: Kinematic Fitter χ^2

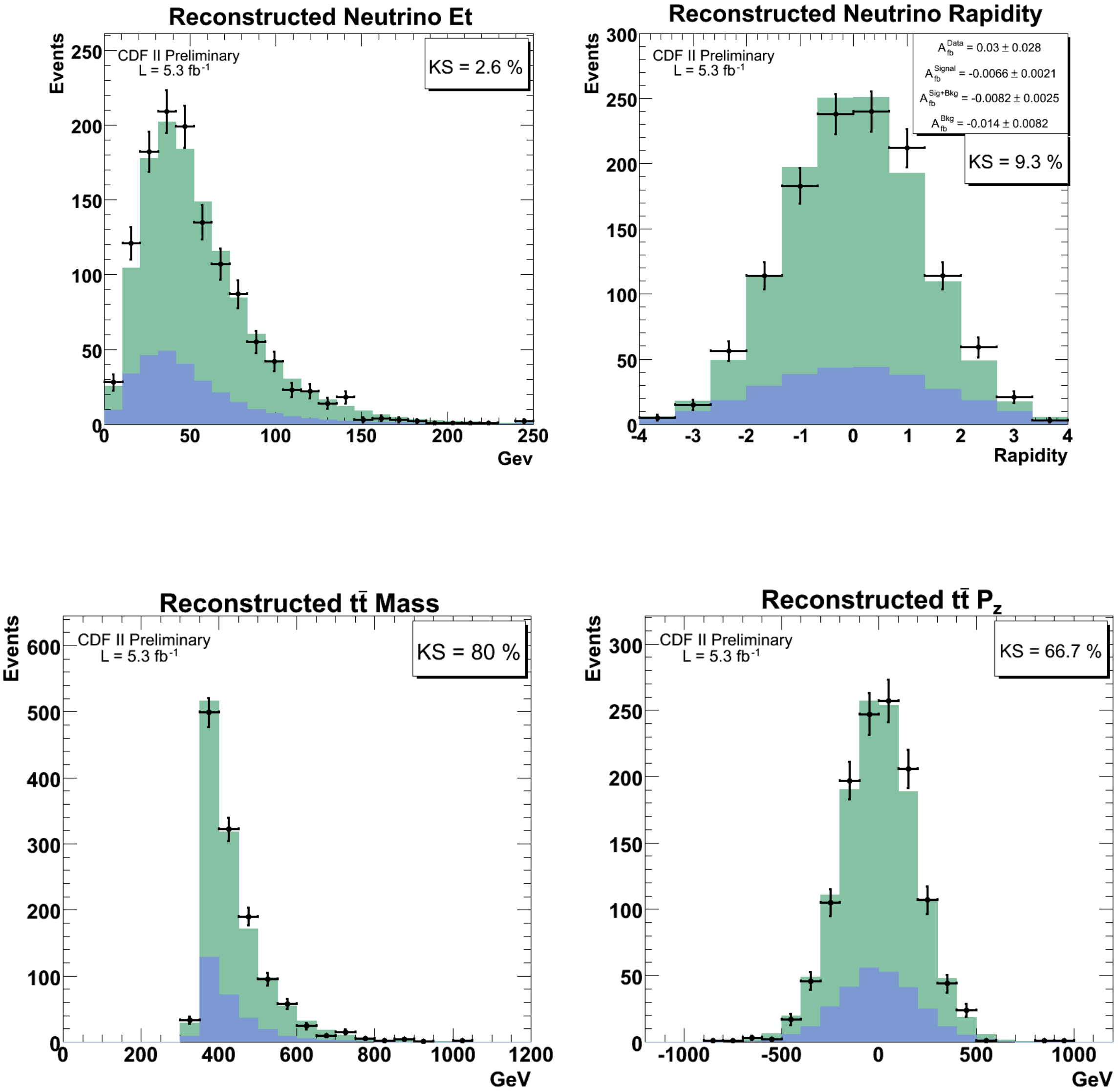

Figure 37: Reconstructed tt̄ Mass and Pz

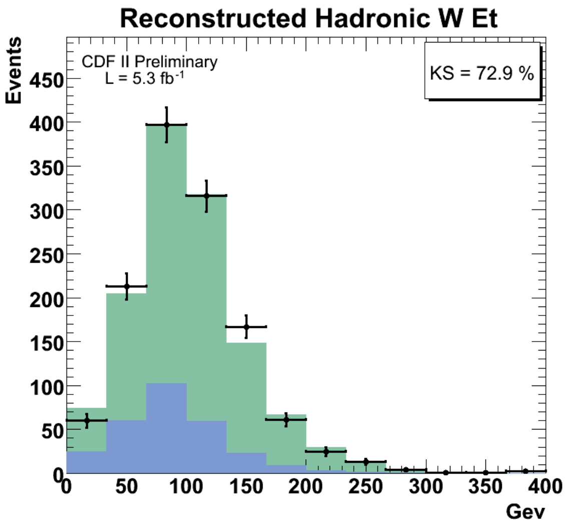
Reconstructed Hadronic W Et

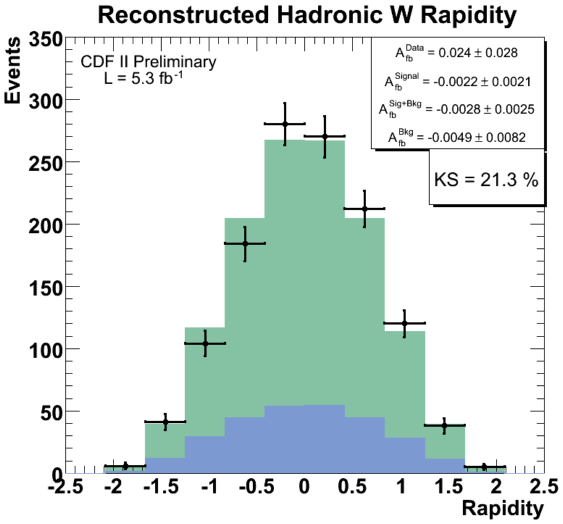
Reconstructed Hadronic W Rapidity

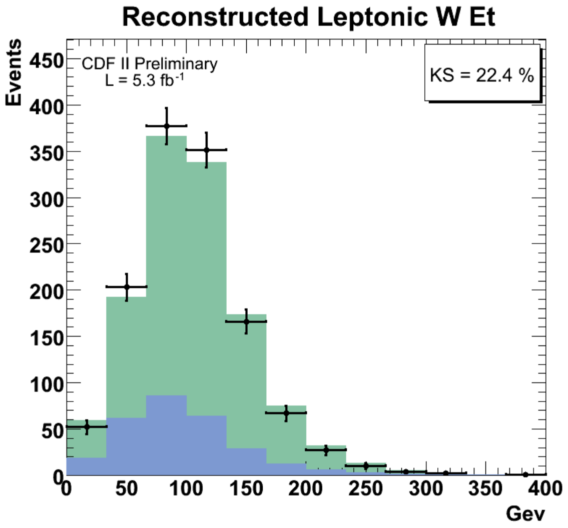
Reconstructed Leptonic W Et

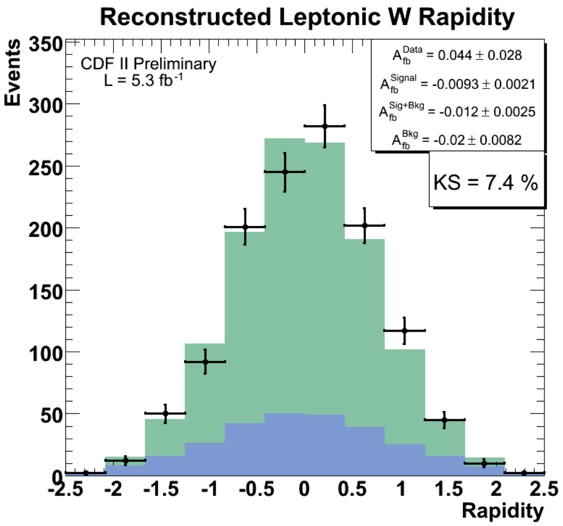
Reconstructed Leptonic W Rapidity

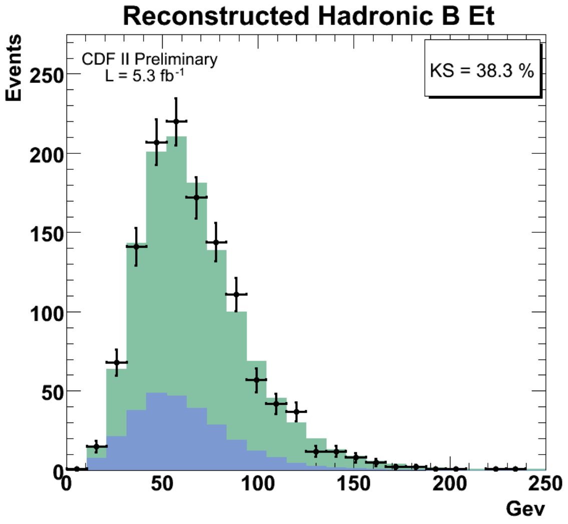
Reconstructed Hadronic B Et
CDF II Preliminary
L = 5.3 fb^{-1}
KS = 38.3 %
Events
0
50
100
150
200
250
Gev

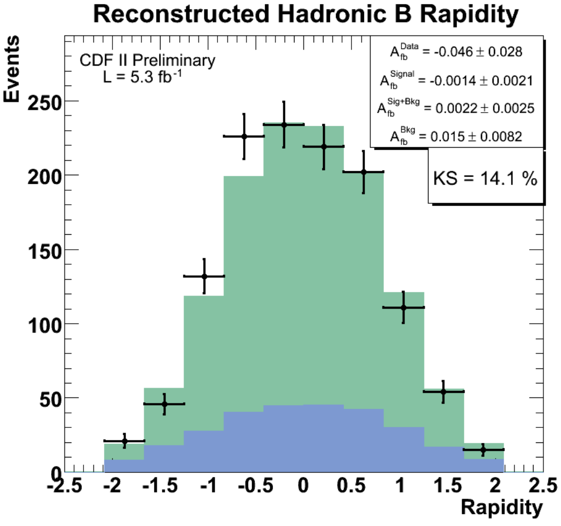
Reconstructed Hadronic B Rapidity
CDF II Preliminary
L = 5.3 fb^{-1}
A_{fb}^{Data} = -0.046 ± 0.028
A_{fb}^{Signal} = -0.0014 ± 0.0021
$A_{fb}^{Sig+Bkg}$ = 0.0022 ± 0.0025
A_{fb}^{Bkg} = 0.015 ± 0.0082
KS = 14.1 %
Events
0
50
100
150
200
250
-2.5
-2
-1.5
-1
-0.5
0
0.5
1
1.5
2
2.5
Rapidity

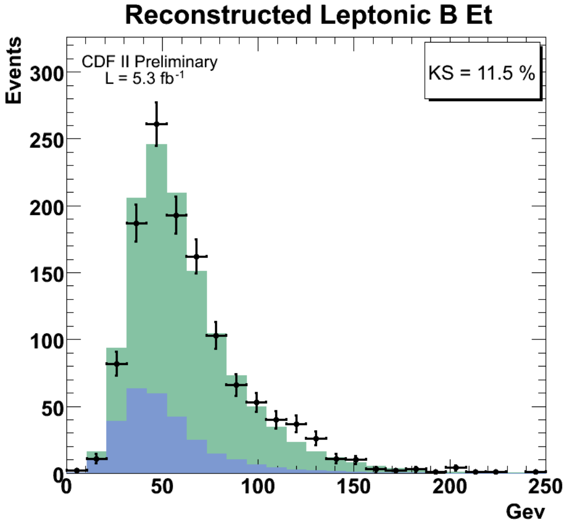
Reconstructed Leptonic B Et
CDF II Preliminary
L = 5.3 fb^{-1}
KS = 11.5 %
Events
0
50
100
150
200
250
300
Gev

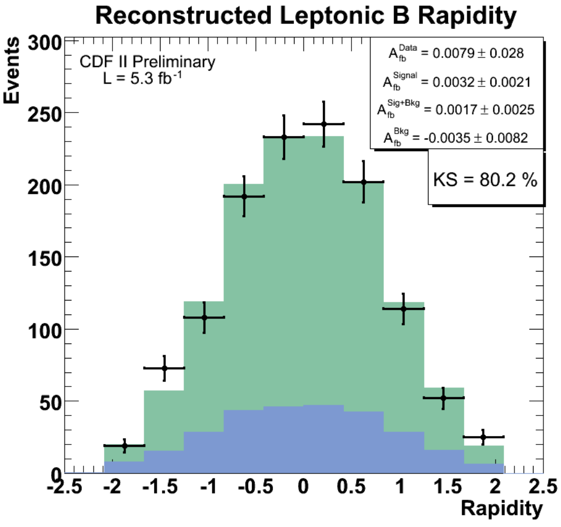
Reconstructed Leptonic B Rapidity
CDF II Preliminary
L = 5.3 fb^{-1}
A_{fb}^{Data} = 0.0079 ± 0.028
A_{fb}^{Signal} = 0.0032 ± 0.0021
$A_{fb}^{Sig+Bkg}$ = 0.0017 ± 0.0025
A_{fb}^{Bkg} = -0.0035 ± 0.0082
KS = 80.2 %
Events
0
50
100
150
200
250
300
-2.5
-2
-1.5
-1
-0.5
0
0.5
1
1.5
2
2.5
Rapidity

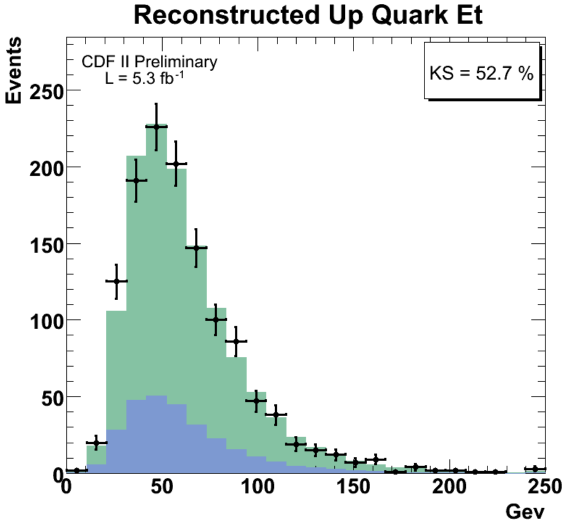
Reconstructed Up Quark Et
CDF II Preliminary
L = 5.3 fb^{-1}
KS = 52.7 %
Events
0
50
100
150
200
250
Gev

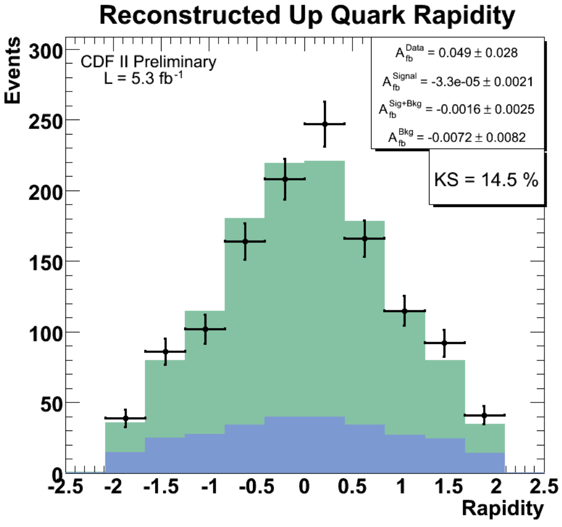
Reconstructed Up Quark Rapidity
CDF II Preliminary
L = 5.3 fb^{-1}
A_{fb}^{Data} = 0.049 ± 0.028
A_{fb}^{Signal} = -3.3e-05 ± 0.0021
$A_{fb}^{Sig+Bkg}$ = -0.0016 ± 0.0025
A_{fb}^{Bkg} = -0.0072 ± 0.0082
KS = 14.5 %
Events
0
50
100
150
200
250
300
-2.5
-2
-1.5
-1
-0.5
0
0.5
1
1.5
2
2.5
Rapidity

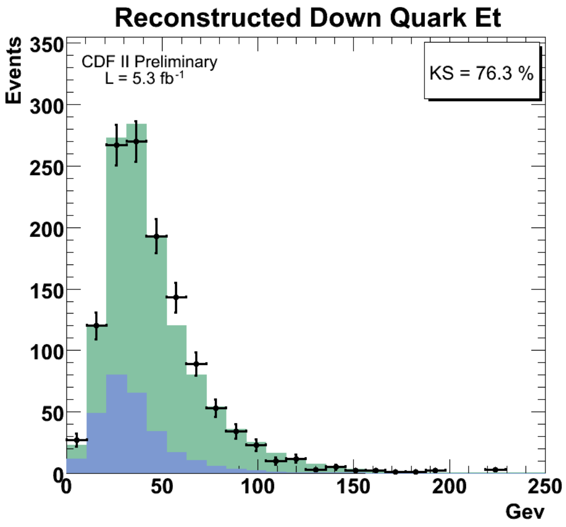
Reconstructed Down Quark Et
CDF II Preliminary
L = 5.3 fb^{-1}
KS = 76.3 %
Events
0
50
100
150
200
250
300
350
Gev

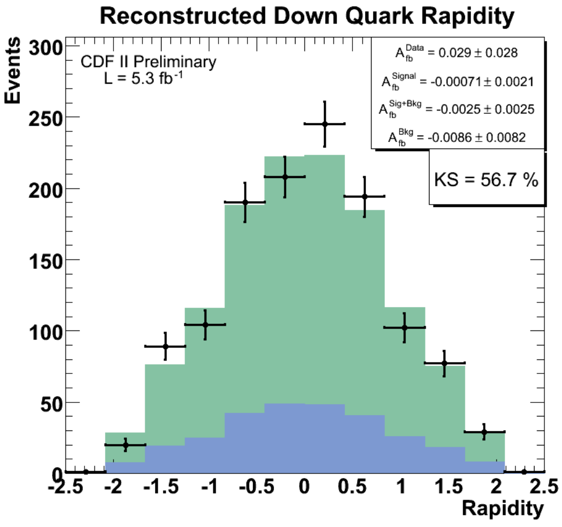
Reconstructed Down Quark Rapidity
CDF II Preliminary
L = 5.3 fb^{-1}
A_{fb}^{Data} = 0.029 ± 0.028
A_{fb}^{Signal} = -0.00071 ± 0.0021
$A_{fb}^{Sig+Bkg}$ = -0.0025 ± 0.0025
A_{fb}^{Bkg} = -0.0086 ± 0.0082
KS = 56.7 %
Events
0
50
100
150
200
250
300
-2.5
-2
-1.5
-1
-0.5
0
0.5
1
1.5
2
2.5
Rapidity

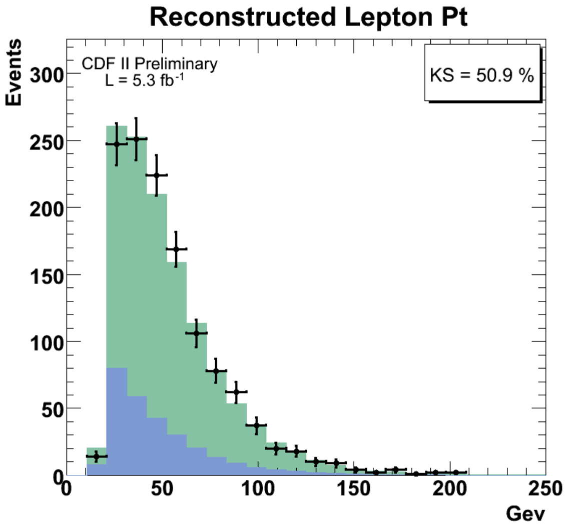
Reconstructed Lepton Pt
CDF II Preliminary
L = 5.3 fb^{-1}
KS = 50.9 %
Events
0
50
100
150
200
250
300
0
50
100
150
200
250
Gev

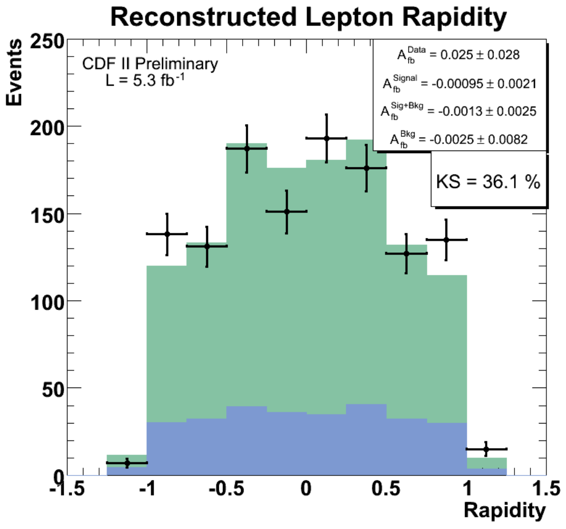
Reconstructed Lepton Rapidity
CDF II Preliminary
L = 5.3 fb^{-1}
A_{fb}^{Data} = 0.025 ± 0.028
A_{fb}^{Signal} = -0.00095 ± 0.0021
$A_{fb}^{Sig+Bkg}$ = -0.0013 ± 0.0025
A_{fb}^{Bkg} = -0.0025 ± 0.0082
KS = 36.1 %
Events
0
50
100
150
200
250
-1.5
-1
-0.5
0
0.5
1
1.5
Rapidity

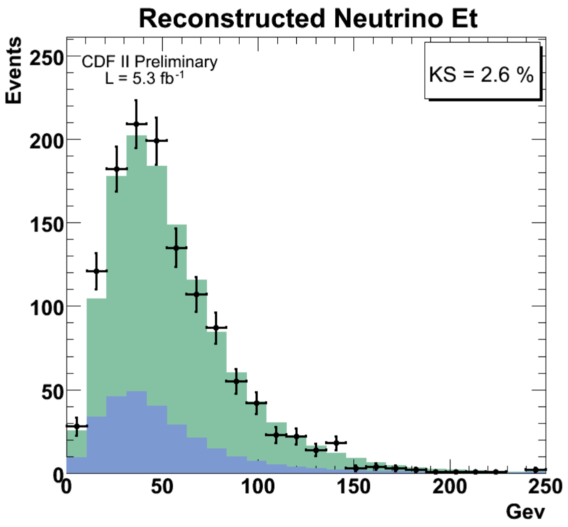
Reconstructed Neutrino Et
CDF II Preliminary
L = 5.3 fb^{-1}
KS = 2.6 %
Events
0
50
100
150
200
250
0
50
100
150
200
250
Gev

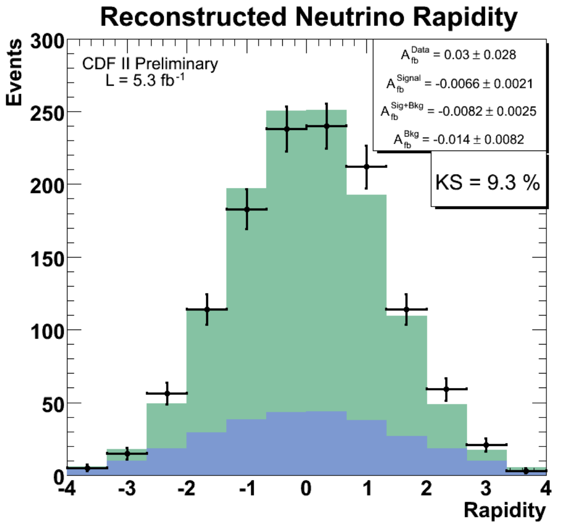
Reconstructed Neutrino Rapidity
CDF II Preliminary
L = 5.3 fb^{-1}
A_{fb}^{Data} = 0.03 ± 0.028
A_{fb}^{Signal} = -0.0066 ± 0.0021
$A_{fb}^{Sig+Bkg}$ = -0.0082 ± 0.0025
A_{fb}^{Bkg} = -0.014 ± 0.0082
KS = 9.3 %
Events
0
50
100
150
200
250
300
-4
-3
-2
-1
0
1
2
3
4
Rapidity